



Dissertations

Theses and Dissertations

Fall 2022

Structural and Transient Kinetic Analysis on Mechanism-Based Inactivators of Human Ornithine Aminotransferase

Arseniy Butrin

Follow this and additional works at: https://ecommons.luc.edu/luc_diss

 Part of the [Biochemistry Commons](#)

Recommended Citation

Butrin, Arseniy, "Structural and Transient Kinetic Analysis on Mechanism-Based Inactivators of Human Ornithine Aminotransferase" (2022). *Dissertations*. 3979.

https://ecommons.luc.edu/luc_diss/3979

This Dissertation is brought to you for free and open access by the Theses and Dissertations at Loyola eCommons. It has been accepted for inclusion in Dissertations by an authorized administrator of Loyola eCommons. For more information, please contact ecommons@luc.edu.



This work is licensed under a [Creative Commons Attribution-Noncommercial-No Derivative Works 3.0 License](#).
Copyright © 2022 Arseniy Butrin

LOYOLA UNIVERSITY CHICAGO

STRUCTURAL AND TRANSIENT KINETIC ANALYSIS ON MECHANISM-BASED
INACTIVATORS OF HUMAN ORNITHINE AMINOTRANSFERASE

A DISSERTATION SUBMITTED TO
THE FACULTY OF THE GRADUATE SCHOOL
IN CANDIDACY FOR THE DEGREE OF
DOCTOR OF PHILOSOPHY

PROGRAM IN CHEMISTRY AND BIOCHEMISTRY

BY

ARSENIY BUTRIN

CHICAGO, IL

AUGUST 2022

Copyright by Arseniy Butrin, 2022
All rights reserved.

ACKNOWLEDGMENTS

I am tremendously grateful to my advisor, Dr. Dali Liu, for providing me an opportunity to do the research in his lab. I strongly appreciate the freedom in the research that he granted to me throughout these years. During my research work in lab, we always had comprehensive discussions and all the decisions were always made based on our mutual understanding of the project and jointly devised course of actions. It was always very valuable to me that my opinion mattered when I could provide my rationale. I am thankful to Dr. Liu for his constant encouragement and guidance during my PhD studies.

I would like to thank Dr. Graham Moran and Dr. Richard Silverman for their collaborations on a large part of this dissertation. With their help, I had an opportunity to learn new techniques and apply them into a multidisciplinary approach during our research. At some point, I've got very enthusiastic about the methods used in Dr. Moran's lab, that I asked if I could unofficially attend his class just to get the grasp of the research he was doing. That class was a real joy for me, I am very glad that I could attend it. I sincerely appreciate an opportunity to work on *hOAT* project provided by Dr. Silverman. I believe that the work on this project in many ways formed me as a researcher, and I am always going to be grateful for that. I also would like to thank Sida Shen, Wei Zhu, and Brett Beaupre for collaborating with me on this project. Investigation of *hOAT* inactivators is not a trivial task and I am happy that I had the best team for this purpose. I am also very grateful to Dr. Miguel Ballicora whose expertise was very critical for me in several key moments during the work on this and other projects.

The research in the lab was much more productive and entertaining thanks to Graeme Lindsey, Noel Kadamandla, Dulce Garcia, Jaina Bhayani, Gaby Matinez-Ramirez, Yuanpu Niu, Dariush Forouzesh, and all the undergraduate members. My gratitude also goes to Yuanzhang Zheng and Daniel Catlin for their mentorship during my first semesters in the lab. I also would like to thank the faculty and staff of the Chemistry department for making graduate school at Loyola a pleasant experience.

I would like to express my gratitude to Arthur J. Schmitt Foundation for awarding me with Schmitt Dissertation Fellowship for the 2021-2022 school year. This fellowship allowed me to finalize my research projects and focus on the writing of my dissertation.

On a personal note, I would like to thank my mother and my sister, Tatyana Butrina and Alexandra Wofsey, who worked very hard to provide me with an opportunity to obtain a PhD. Thanks to their unconditional love and support, I happened to be where I am now. They worked very hard to ensure that I had access to a good education, and I could fulfill my potential. They are incredible people, and I am extremely lucky to have them in my life.

I would like to thank my dear wife, Anastasiya Butrin. No one knows better than her how overwhelming a life of a PhD student can be, and I appreciate her constant support throughout all these years. I heartily appreciate her willingness to rationalize and discuss complicated scientific topics with me at any time of the day. Our discussions always served me as inspiration to continue my research studies even in ambiguous and stressful moments. I am blessed to have such a caring and thoughtful person in my life.

I am very grateful to my brother-in-law Stephen and his parents Avrom and Debbie Wofsey. Ten years ago, for the first time in my life, Stephen and Avrom took me to the National

Air and Space Museum in Washington DC. For a fourteen-year-old boy who I was, this experience was life-changing. That museum trip sparked my interest in science and predetermined my future career. To this day, I remember my excitement and fascination when I first saw Discovery space shuttle. To me, it was a demonstration of how science helps humanity to excel and achieve goals that are outside of our nature. There, for the first time, I realized that the purpose of science is to advance ourselves toward a greater cause. On that day, I spent over eight hours in the museum, and I still didn't want to leave. Throughout all these years Stephen has helped me infinite number of times and to this day he keeps supporting and guiding me on my life path.

I also would like to thank Vladimir Ivanovich Klyuchko, my friend and high school math teacher who recognized me as a curious student. He spent countless hours educating me and always teaching something extra, outside school curriculum. Technically speaking, my first publication was in a Russian math journal, called "Math in School" where we submitted a solution to the series problem using plain arithmetic and logic. I always remember Vladimir Ivanovich as a very skeptical (but not cynical) person who places facts and logic above everything else. To me, he continues to serve as a role model of a very rational, yet very amusing, supportive, and inspirational scientist.

To my father, grandparents, and those who are no longer with us, but always remain in our hearts.

The first principle is that you must not fool yourself and you are the easiest person to fool.
- Richard P. Feynman

TABLE OF CONTENTS

ACKNOWLEDGMENTS	iii
LIST OF FIGURES	x
LIST OF TABLES	xiii
LIST OF SCHEMES	xiv
LIST OF ABBREVIATIONS	xv
ABSTRACT	xvii
CHAPTER ONE: INVESTIGATION OF pH DEPENDENCE, SUBSTRATE SPECIFICITY, AND TURNOVERS OF ALTERNATIVE SUBSTRATES FOR HUMAN ORNITHINE AMINOTRANSFERASE	1
Summary	1
Introduction	2
Results	5
Discussion	22
Experimental Procedures	30
CHAPTER TWO: STRUCTURAL AND TRANSIENT KINETIC ANALYSES REVEAL THE DUAL INHIBITION MODES OF HUMAN ORNITHINE AMINOTRANSFERASE BY (1 <i>S</i> ,3 <i>S</i>)-3-AMINO-4-(HEXAFLUOROPROPAN-2-YLIDENYL)-CYCLOPENTANE-1- CARBOXYLIC ACID (BCF ₃)	38
Summary	38
Introduction	39
Results	43
Discussion	55
Experimental Procedures	62
CHAPTER THREE: TURNOVER AND INACTIVATION MECHANISM FOR (S)-3-AMINO- 4,4-DIFLUOROCYCLOPENT-1-ENE-CARBOXYLIC ACID, A SELECTIVE MECHANISM-BASED INACTIVATOR OF <i>h</i> OAT	67
Summary	67
Introduction	68
Results	69

Discussion	77
Experimental Procedures	79
CHAPTER FOUR: RATIONAL DESIGN, SYNTHESIS, AND MECHANISM OF (3 <i>S</i> ,4 <i>R</i>)-3-AMINO-4-(DIFLUOROMETHYL) CYCLOPENT-1-ENE-1-CARBOXYLIC ACID EMPLOYING A SECOND DEPROTONATION STRATEGY FOR SELECTIVITY OF <i>h</i> OAT OVER GABA-AT	
	83
Summary	83
Introduction	84
Results	87
Discussion	102
Experimental Procedures	103
CONCLUSION	108
REFERENCE LIST	113
VITA	123

LIST OF FIGURES

Figure 1. Chemical structures of L-ornithine and three substrate analogs: L-2,4-Diaminobutyric acid (DABA), 5-aminovaleric acid (AVA), and γ -aminobutyric acid (GABA).	4
Figure 2. <i>hOAT</i> pH dependence plots for the first half-reaction with L-Orn and the second half-reaction with α -KG.	6
Figure 3. Comparison of the active site structure of <i>hOAT</i> at pH 6.0 and 7.8.	8
Figure 4. Polder map (at 2.0 σ level) of <i>hOAT</i> crystallized at pH 6.0.	9
Figure 5. Overlay of crystal structures of <i>hOAT</i> at pH 6.0 and pH 7.8.	10
Figure 6. Transient-state absorption changes observed at 335 nm for <i>hOAT</i> reacting with L-Orn, AVA, and DABA.	12
Figure 7. Transient-state absorption changes observed at 420 nm for 9 μ M <i>hOAT</i> reacting with 250, 500, 1000, and 2000 μ M GABA.	13
Figure 8. Comparison of the <i>hOAT</i> holoenzyme spectrum with the initial spectrum after addition of the 2 mM GABA, 1 mM AVA, or 8 mM DABA.	15
Figure 9. The absorption spectra of 9 μ M holoenzyme <i>hOAT</i> at pH 6.0 and pH 8.5.	16
Figure 10. Polder map (F_0 - F_c , at 3.0 σ) of the <i>hOAT</i> structure soaked with GABA and AVA.	19
Figure 11. Comparison of the phosphate binding site in crystal structure of <i>hOAT</i> soaked with AVA and biological dimer of holoenzyme.	21
Figure 12. Simplified mechanism of reaction of <i>hOAT</i> with its native substrate L-ornithine.	23
Figure 13. Initial and final spectra of the reaction between 8 mM AVA and 9 μ M <i>hOAT</i> .	26

Figure 14. Initial (black) and final (red) spectra of the reaction between 8 mM DABA and 10.4 μ M <i>h</i> OAT.	26
Figure 15. Initial (black) and final (red) spectra of the reaction between 8 mM L-ornithine and 9 μ M <i>h</i> OAT.	27
Figure 16. Transient state absorption changes observed at 567 nm for <i>h</i> OAT reacting with BCF ₃ .	44
Figure 17. Transient state CCD data for <i>h</i> OAT reacting with BCF ₃ .	46
Figure 18. Transient state nuclear magnetic resonance changes observed for <i>h</i> OAT reacting with BCF ₃ .	47
Figure 19. ¹⁹ F-NMR spectrum of <i>h</i> OAT-BCF ₃ inactivation reaction after 8 hours.	48
Figure 20. ¹⁹ F-NMR spectrum of the <i>h</i> OAT reaction with BCF ₃ after 5 minutes.	49
Figure 21. The structure of <i>h</i> OAT homodimer in the external aldimine II state.	50
Figure 22. Comparison of the <i>h</i> OAT structures of the external aldimine II state and the covalently inhibited complex, external aldimine V.	51
Figure 23. Polder map ($F_o - F_c$ at 3.8 σ) generated by omitting the external aldimine II from the structure.	52
Figure 24. Comparison of the <i>h</i> OAT BCF ₃ derived external aldimine II to that formed from 5-fluoromethylornithine (5FMeOrn).	53
Figure 25. External aldimine II in the active site cavity.	54
Figure 26. BCF ₃ and previously developed mono-trifluoromethyl inhibitors.	57
Figure 27. Crystal structures of <i>h</i> OAT resulting from soaking experiment and cocrystallization with compound 148.	71
Figure 28. Transient state absorption changes observed at 275, 420, and 560 nm for <i>h</i> OAT reacting with 148.	73

Figure 29. Partial deconvolution by singular value decomposition (SVD) of transient state absorption changes observed for <i>hOAT</i> reacting with 148.	77
Figure 30. The metabolic role of <i>hOAT</i> .	85
Figure 31. Structures of GABA analogs 1, 6-11.	86
Figure 32. Cocrystal structures of <i>hOAT</i> inactivated by 7 and 1.	88
Figure 33. Omit map (at 2.5 σ) of <i>hOAT</i> -8 cocrystal structure.	91
Figure 34. Comparison of <i>hOAT</i> -10b and <i>hOAT</i> -11 models.	93
Figure 35. Cocrystal structure of <i>hOAT</i> inactivated by 10b and 11.	94
Figure 36. Spectral deconvolution of the <i>hOAT</i> , 10b reaction.	97
Figure 37. Spectra observed during inactivation by 10b.	98
Figure 38. Kinetic analysis of the <i>hOAT</i> -10b reaction at 410 nm.	100
Figure 39. Kinetic analysis of the <i>hOAT</i> -10b reaction at 320 nm.	101
Figure 40. Four different inhibition modes discovered for <i>hOAT</i> .	111

LIST OF TABLES

Table 1. Summary of kinetic parameters for <i>hOAT</i> using various substrates.	17
Table 2. Statistics of the crystal structures of holoenzyme <i>hOAT</i> crystallized at pH 6.0, soaked with AVA, and soaked with GABA.	37
Table 3. Statistics table for <i>hOAT</i> -external aldimine II crystal structure.	66
Table 4. Statistics of the crystal structures of <i>hOAT</i> inactivated by 148.	82
Table 5. Statistics of the crystal structure of <i>hOAT</i> inactivated by compound 1, 7, 10b, and 11.	105

LIST OF SCHEMES

Scheme 1. Summarized half-reactions of <i>h</i> OAT.	3
Scheme 2. Two potential pathways for cyclization in the last step of the forward half-reaction of <i>h</i> OAT.	28
Scheme 3. Proposed Inactivation Mechanism of <i>h</i> OAT by BCF ₃ .	41
Scheme 4. Four-step model for the intermediates observed via CCD 340-700 nm and ¹⁹ F-NMR spectrometry.	63
Scheme 5. Plausible Inactivation Mechanisms of 148 with <i>h</i> OAT.	75
Scheme 6. Plausible Inactivation Mechanisms of <i>h</i> OAT by 7.	89
Scheme 7. Plausible Inactivation Mechanisms of <i>h</i> OAT by 1.	90
Scheme 8. Plausible mechanism for 10b with <i>h</i> OAT and GABA-AT.	95
Scheme 9. Transient kinetics of the reaction of 10b with <i>h</i> OAT.	99

LIST OF ABBREVIATIONS

<i>h</i> OAT	human Ornithine Aminotransferase
HCC	Hepatocellular carcinoma
L-Orn	L-ornithine
α -KG	α -ketoglutarate
PLP	Pyridoxal Phosphate
PMP	Pyridoxamine Phosphate
MBI	Mechanism-based inactivator
GSA	Glutamate-5-semialdehyde
P5C	1-pyrroline-5-carboxylic acid
GABA	γ -aminobutyric acid
GABA-AT	GABA-Aminotransferase
DABA	L-2,4-diaminobutyric acid
AVA	5-aminovaleric acid
BCF ₃	(1 <i>s</i> ,3 <i>s</i>)-3-amino-4-(hexafluoropropan-2-ylidenyl)-cyclopentane-1-carboxylic acid
CCD	Charged-coupled device
L	Liter
mL	Milliliters

IPTG	Isopropyl β -D-1-thiogalactopyranoside
PEG	Polyethylene glycol
<i>E. Coli</i>	<i>Escherichia coli</i>
Compound 148	(S)-3-amino-4,4-difluorocyclopent-1-enecarboxylic acid
Compound 1	(1S,3S)-3-amino-4-difluoromethylenyl-1-cyclopentanoic acid
Compound 10b	(3S,4R)-3-amino-4-(difluoromethyl)cyclopent-1-ene-1-carboxylate
Compound 11	(S,E)-3-amino-4-(fluoromethylene)cyclopent-1-ene-1-carboxylate
MBP	Maltose binding protein
TEV	Tobacco etch virus
GS	Glutamine synthetase

ABSTRACT

Hepatocellular carcinoma (HCC) is a primary cancer of liver that occurs predominantly in patients with underlying chronic liver diseases. Currently, HCC is the third leading cause of cancer-related death worldwide and, according to the World Health Organization, the incidence of the disease is expected to rise until 2030 in several countries including the United States. Current methods of HCC treatment are effective in the early stages but are found to be ineffective in the later disease stages. Thus, a novel approach is required to successfully suppress HCC. In the last twenty years, it was found that the enzyme ornithine aminotransferase (OAT) is overexpressed in HCC cells. Several independent studies have shown that OAT plays an important role in the development and division of malignant cells. This makes OAT a promising target for anticancer therapy, especially for the mechanism-based inactivators. In the last years, several OAT inactivators have been synthesized and have shown the capacity to slow the progression of HCC in animal models. To improve the efficacy of the designed inactivators, knowledge on the inactivation mechanisms is required. In this dissertation project, three novel OAT inactivators were investigated structurally and kinetically using a combination of X-ray crystallography, stopped-flow spectrophotometry, and nuclear magnetic resonance spectroscopy. The data gained from these experiments potentially could be used for the rational design of a new generation of drugs against HCC.

CHAPTER ONE

INVESTIGATION OF pH DEPENDENCE, SUBSTRATE SPECIFICITY, AND TURNOVERS OF ALTERNATIVE SUBSTRATES FOR HUMAN ORNITHINE AMINOTRANSFERASE

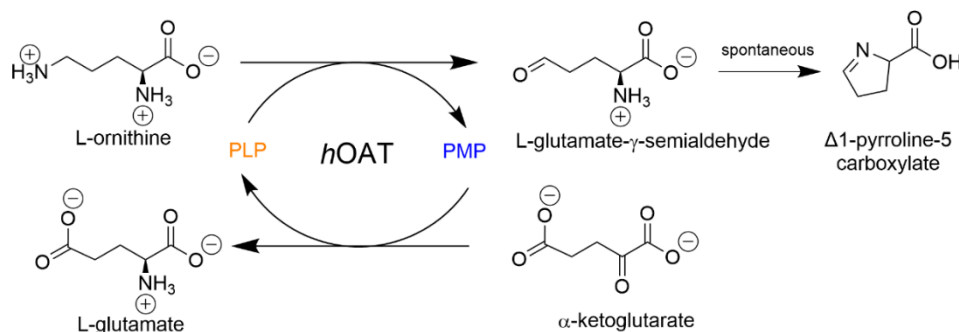
Summary

Hepatocellular carcinoma (HCC) is the most common primary cancer of liver and occurs predominantly in patients with underlying chronic liver diseases. In the last decades, human ornithine aminotransferase (*hOAT*), a PLP-dependent enzyme found overexpressed in HCC cells, has emerged as a promising target for novel anticancer therapy, especially for the ongoing rational design effort to discover mechanism-based inactivators (MBIs). Despite *hOAT*'s significance in human metabolism and its clinical potential as a drug target against HCC, there are significant knowledge deficits with regard to its mechanism and structural characteristics. Ongoing MBI design efforts require in-depth knowledge of the enzyme active site, in particular, pKa values of the potential nucleophiles and the molecular recognition of ligands. This work presents a study on the fundamental active site properties of *hOAT* using stopped-flow spectrophotometry and X-ray crystallography. The results quantitatively revealed the pH dependence for the multi-step reaction and elucidated the roles of α and δ -amino groups in substrate recognition and catalysis. The results reveal mechanistic aspects that could benefit the rational design of MBIs of *hOAT*. The manuscript with results of this work was submitted for publication and is currently under review (Butrin A.; et al. Investigation of pH dependence,

substrate specificity, and turnovers of alternative substrates for human ornithine aminotransferase. 2022).

Introduction

Human ornithine aminotransferase (*hOAT*)¹ is an enzyme that catalyzes the transfer of δ -amino group from L-ornithine (L-Orn) to α -ketoglutarate (α -KG). As a pyridoxal-5'-phosphate (PLP)-dependent transaminase, *hOAT* has a “Bi-Bi, Ping-Pong” kinetic mechanism. In the first half-reaction, PLP and L-Orn are converted to pyridoxamine phosphate (PMP) and L-glutamate- γ -semialdehyde (L-GSA). L-GSA is then prone to cyclize to Δ 1-pyrroline-5-carboxylate (P5C). In the second half-reaction, *hOAT* catalyzes the transfer of the amino group of PMP to an α -keto acid, preferentially α -KG, forming glutamate and regenerating PLP (Scheme 1).



Scheme 1. Summarized half-reactions of *hOAT*.

In mammals, OAT is vital to multiple metabolic pathways including glutamine metabolism, proline and arginine biosynthesis, and the urea cycle. In addition, it was found that OAT plays a crucial role in the early development of neonates² for the reason that mammalian milk is a poor source of arginine and thus it must be synthesized from citrulline, whose concentration is regulated by OAT in the small intestine³. The conversion of significant

amounts of proline from maternal milk into arginine has been confirmed for human, pig, and mouse neonates^{2-3,4-5}. Deficiency and inhibition of OAT in humans was found to cause gyrate atrophy⁶ and hyperornithinemia⁷. While some slow-developing diseases are associated with insufficient amounts of *hOAT*, studies have also shown that overexpression of *hOAT* supports the proliferation and development of the cancer cells⁸⁻⁹. Hepatocellular carcinoma (HCC) is the most common form of primary liver cancer, accounting for 90% of all cases of liver cancer in the United States¹⁰⁻¹³. If diagnosed early, HCC can be treated at the early stages via surgery. In the latter stages, additional treatment is required including radio- and chemotherapy¹⁴⁻¹⁷. In reality, HCC is typically diagnosed in advanced disease stages when tumors are resistant to both radio- and chemotherapy. Recently published works have shown that *hOAT* and other glutaminogenic enzymes were found to be overexpressed in HCC cells due to abnormal oncogenic Wnt/ β -catenin signaling⁸⁻⁹. Thus, *hOAT* has been identified as a potential drug target for novel anticancer therapy against HCC. Some work on *in vivo* inhibition of *hOAT* in the HCC mouse models already demonstrated encouraging results for a potential antitumor effect by mechanism-based OAT inactivators¹⁸.

Despite the significance of *hOAT* in normal human physiology and its proven participation in HCC development, many fundamental properties of this enzyme remain unknown. pH studies on *hOAT* have not been carried out in a quantitative manner and a macroscopic pKa that determines the rate-limiting step in the forward and reverse half-reactions has not been identified. It is also unclear if and how the conformation of the protein responds to changes in pH. Like several other aminotransferases, OAT is a promiscuous enzyme and a number of its alternative substrates have been identified experimentally¹⁹. But detailed

mechanistic and structural analysis of the enzyme's interaction with alternative substrates is currently lacking. In the current work, some of the fundamental questions on *hOAT* are addressed. A pH profile for the rate-limiting step(s) was generated and key kinetic pKa values were determined. Transient-state kinetic experiments on L-Orn and three other smaller alternative substrates have been performed (Figure 1). Crystal soaking experiments were employed to trap intermediate states for these ligands. The results elucidate the importance of substrate α and δ -amino groups in substrate recognition and catalysis. In addition, current work produced some experimental results that are consistent with the cyclization of the final product before its release from the active site. The obtained data could serve as a structural and mechanistic basis for the development of a new generation of *hOAT* inhibitors and/or mechanism-based inactivators that mimic the fragment-sized alternative substrates, such as γ -aminobutyric acid or 5-aminovaleric acid.

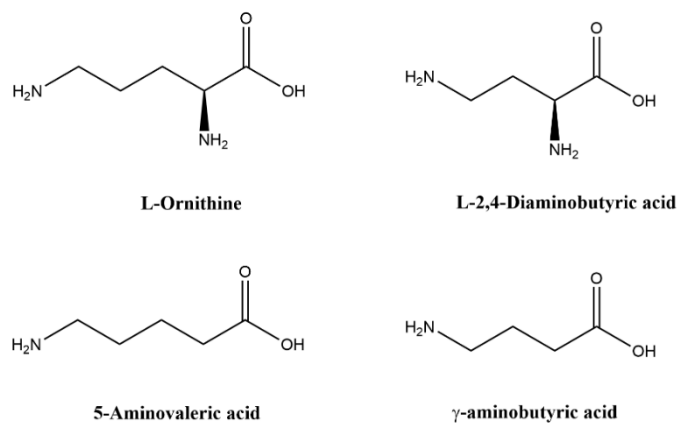


Figure 1. Chemical structures of L-ornithine and three substrate analogs: L-2,4-Diaminobutyric acid (DABA), 5-aminovaleric acid (AVA), and γ -aminobutyric acid (GABA).

Results

Among the unanswered questions pertaining to *hOAT*'s structural and mechanistic properties, one of them addressed in this work is the determination of the macroscopic pKa values for the enzyme's native forward and reverse half-reactions. It has been previously shown that the kinetics of each half-reaction of rat liver OAT is influenced by pH, however, those experiments were largely qualitative²⁰ because the working pH ranges of the enzyme were identified without measurement of the macroscopic pKa for either of the two half-reactions. In the current work, the pH profile of *hOAT* was observed for the forward half-reaction using L-Orn and for the reverse half-reaction using α -KG with stopped-flow spectroscopy. To augment the kinetic experiments, holo-*hOAT* was crystallized at a pH of 6.0. The protein crystal diffracted to a resolution of 2.1 Å and revealed notable changes in the orientation of specific active site residues. To investigate substrate specificity of *hOAT*, transient-state kinetic experiments were conducted with three analogs of L-Orn: AVA, GABA, and DABA (Figure 1). All analogs exhibited relatively slow catalytic rates; therefore, a series of *hOAT* crystal soaking experiments were conducted in an attempt to capture structures of their reaction intermediates. The soaking experiments resulted in a structure of GABA covalently attached to the PLP as well as the structure of AVA linked both to PLP and the catalytic Lys292.

pH dependences of the half-reactions of hOAT

PLP-dependent enzymes exhibit prominent signature spectrophotometric absorption characteristics that facilitate observation of their reactions. By monitoring the spectrum of the cofactor during turnover explicit details of the reaction mechanism can be elucidated²¹⁻²². For the

pH study of *hOAT*, transient-state pH-jump experiments were conducted using the stopped-flow instrument. These data are shown in Figure 2.

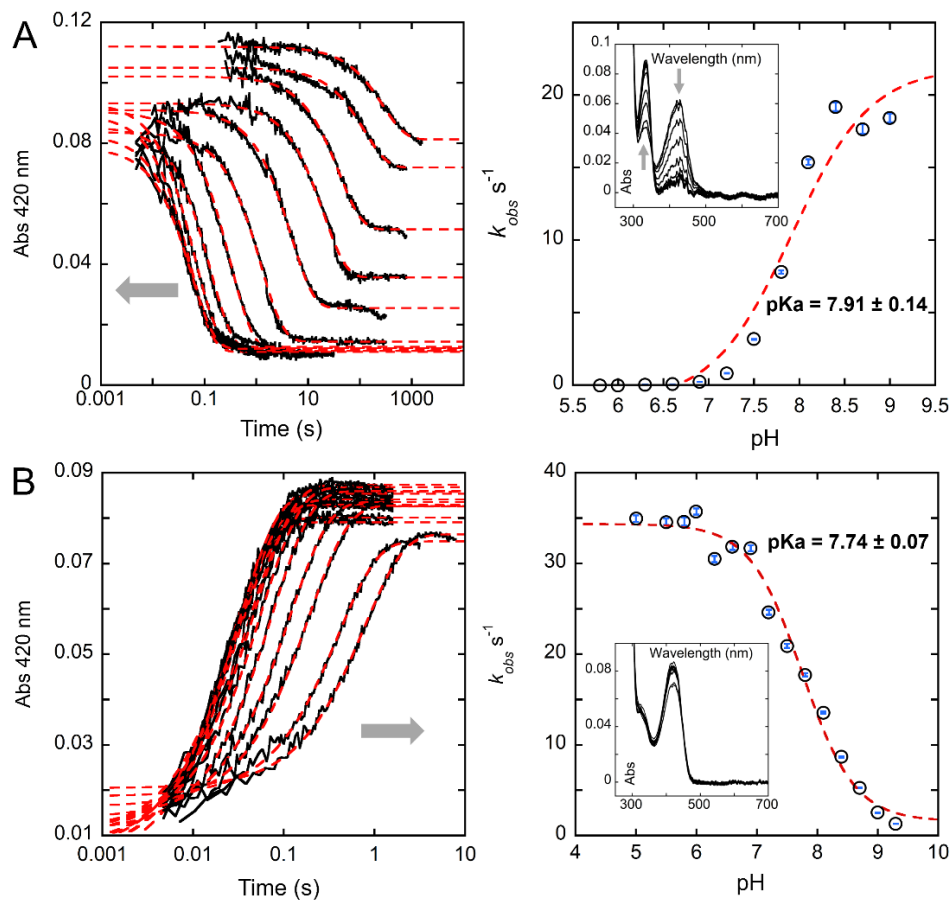


Figure 2. *hOAT* pH dependence plots for the first half-reaction with L-Orn (A) and the second half-reaction with α -KG (B). Each kinetic trace was fit to equation 1 to determine observed rate constants (k_{obs}). The pH dependence of the k_{obs} values was fit to equation 2. In each plot to the left, the gray arrow indicates the trend toward higher pH values. The observed rate was measured at pH values of 5.8, 6.0, 6.0, 6.3, 6.6, 6.9, 7.2, 7.5, 7.8, 8.1, 8.4, 8.7, and 9.0. The markers are shown as hollow black circles overlaying blue error bars, the magnitudes of which are derived from the fit to equation 2. Spectra extracted at equilibrium are shown as the insets and represent the balance of aldimine and PMP forms of the enzyme.

Both reactions were observed under pseudo-first-order conditions using CCD detection from 250 to 800 nm. In both cases, the data are described by the fit to a single exponential and

thus report only interconversion between the external aldimine and PMP. From the pH profiles, it was determined that the first half-reaction with L-Orn approaches the maximum rate at \sim pH 9.5. The kinetic pKa was calculated to be 7.91 ± 0.14 . For the second half-reaction with α -KG, the maximum reaction rate was observed at pH ≤ 6.0 and it decreased with higher pH. The kinetic pKa was determined as 7.74 ± 0.07 . The observed small difference in the pKa values may indicate titration of the same group acting in the rate-limiting catalytic step of both the first and the second half-reaction, such as tethering Lys292. Although the solution pKa value for the ϵ amino group of lysine is 10.53²³, the pKa of Lys292 may be shifted to a lower value in the active site of *hOAT* as has been observed for aspartate aminotransferase²⁴.

Spectra extracted at equilibrium represent the balance of aldimine and PMP forms of the enzyme (Figure 2 insets). These spectra indicate that the first half-reaction is biased forward to the PMP state only at high pH values and that the product of the first half-reaction, L-GSA, is a substrate for the second half-reaction, dictating that ring closure to P5C does not occur on the surface of the enzyme. Conversely, the second half-reaction with α -KG as a substrate is strongly biased toward aldimine and L-glutamate formation at all pHs.

Crystal structure of holo-hOAT at pH 6.0

The observed rate decrease in the first half-reaction rate of *hOAT* with L-Orn at low pH in stopped-flow experiments indicates that deprotonation of one or more active site groups enhances the rate of the reaction. To structurally assess the influence of low pH values, an X-ray crystal structure of *hOAT* at pH 6.0 was obtained at 2.1 Å resolution. This structure was solved using molecular replacement (search model PDB ID: 1OAT²⁵). After model-building and

refinements, the final model presents three monomers in an asymmetric unit of the C 1 2 1 space group (Table S1). The active site of the structure of *hOAT* internal aldimine state at pH 6.0 and pH 7.8 is depicted in Figure 3.

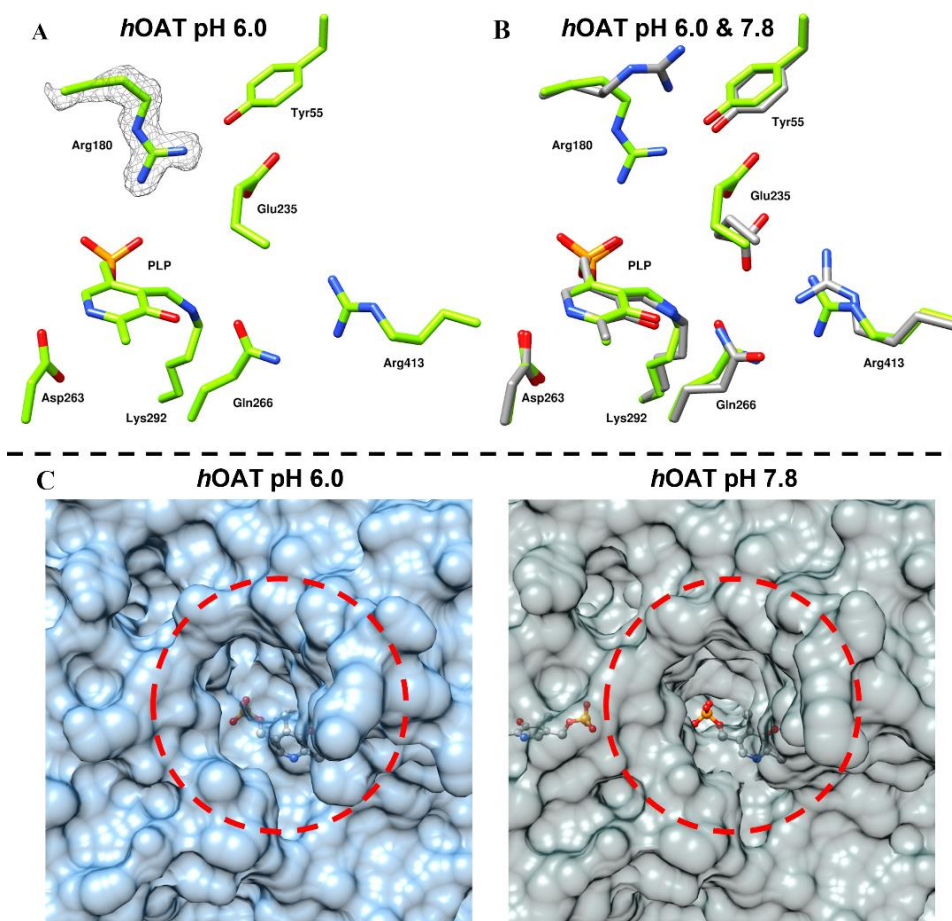


Figure 3. Comparison of the active site structure of *hOAT* at pH 6.0 and 7.8. A. The active site of *hOAT* crystallized at pH 6.0 (PDB ID: 7T9Z). The electron density (simulated annealing composite $2F_o - F_c$ map at 1.1σ) is shown as a gray contour around Arg180. B. Overlaid structures of *hOAT* at pH 6.0 (green) and pH 7.8 (gray). C. Comparison of *hOAT* homodimer surface within the active site cavity at pH 7.8 (right) and pH 6.0 (left). The active site pocket for both structures is indicated by a dashed red circle.

Although no major structural changes were detected in the overall quaternary and tertiary structure of *hOAT* at pH 6.0, some notable deviations were observed in local conformations of

the active site residues. The acidic pH altered the position of the Arg180 side chain, a residue responsible for initial substrate recognition and binding²⁵⁻²⁶. In addition, the side chain of Glu235 exhibited relatively weak electron density reflecting increased mobility of this residue at lower pHs. In the refined low pH model, the side chain of Glu235 faces away from Arg413 (Figure 4).

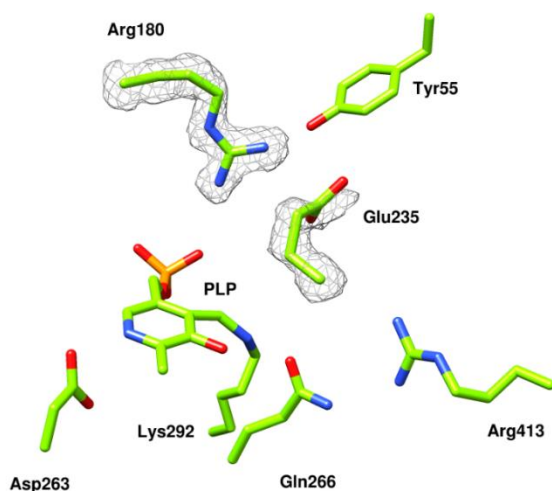


Figure 4. Polder map (at 2.0σ level) of *hOAT* crystallized at pH 6.0. The electron density is shown as a gray mesh around Arg180 and Glu235.

The Arg413-Glu235 salt bridge is known to act as a molecular switch that prevents a possible nonproductive interaction between L-Orn and Arg413 in the forward reaction²⁷. In the pH 6.0 structure, Arg180 moved towards the active-site center occupying the space where the substrate would be localized. As shown in Figure 5, sidechains of Arg180 and Glu235 regulate the width of the active site pocket and act as a gate through which the ligand passes to the active

site. At pH 7.8, the distance between the two sidechains is 7.8 Å, but it reduces to 5.7 Å at pH 6.0.

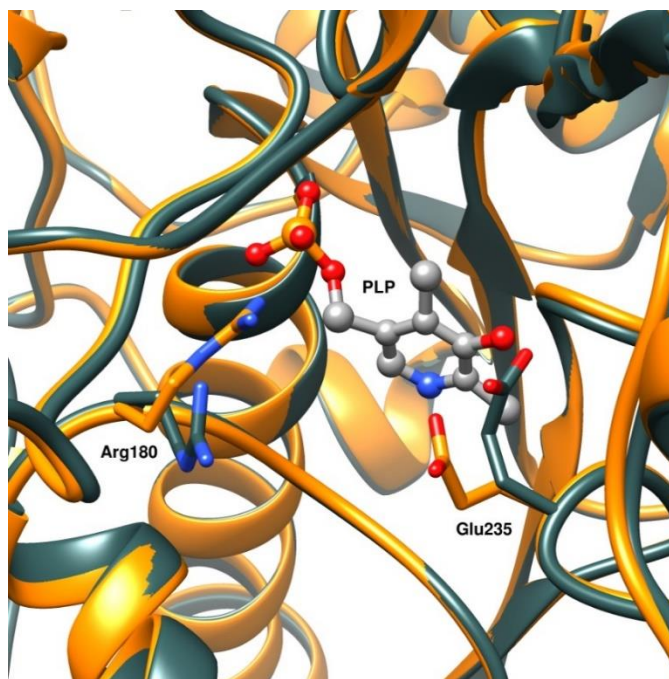


Figure 5. Overlay of crystal structures of *hOAT* at pH 6.0 (orange) and pH 7.8 (dark blue). The Arg180 and Glu235 side chains are shown as sticks for both structures. The positions of these two residues control the width of the active site pocket.

This results in the constriction of the active site pocket as shown in protein surface comparison in Figure 3C. Such conformational alterations for Arg180 and Glu235 could directly impair binding affinity to the substrates and/or contribute to the observed decrease in the catalytic rate (Figure 2). Moreover, with the loss of interaction between Arg413 and Glu235, there is the potential for the carboxyl group of L-Orn to form a charge-pairing interaction with Arg413 resulting in non-productive binding. The observed conformational changes for Arg180 and Glu235-Arg413 could account for the decreased reaction rate at low pH in the first half-reaction or could be additive with changes in the protonation state of other active site residues

and/or PLP that do not induce conformational alterations and so are not observed crystallographically.

Transient-state measurements of hOAT reaction with alternative substrates

Despite the fact that *hOAT* is mainly characterized as a δ -aminotransferase, several recent publications have shown that the enzyme is capable of reacting with cyclized ligands where the amino group was located in the γ position²⁸⁻³¹. Moreover, it was demonstrated that L-glutamate with a single α -amino group could also serve as a substrate in the first half-reaction³². Other works on *hOAT* included mutations of Tyr55 and Arg180 and confirmed their role in anchoring L-Orn through noncovalent interactions with the carboxylate and α -amino group³³⁻³⁴, respectively. However, how the active-site recognition of the δ - and α -amino groups of L-Orn as well as how the substrate size contributes to both binding and catalysis haven't been investigated in detail. The mechanistic and structural determinants of the substrate preference displayed by *hOAT* for L-Orn are not clear, as aminotransferases are commonly known for their catalytic promiscuity³⁵⁻³⁶. To explore the determinants of substrate selectivity, three substrate analogs of L-Orn were selected and allowed to react with *hOAT*. The results of transient-state kinetics experiments were compared to that of L-Orn. Each compound was titrated against *hOAT*, and the absorption changes associated with the reaction were observed. The results of transient-state absorption changes at 335 nm, which report the formation of PMP produced in the first half-reaction for all tested substrates, are shown in Figures 6, 7.

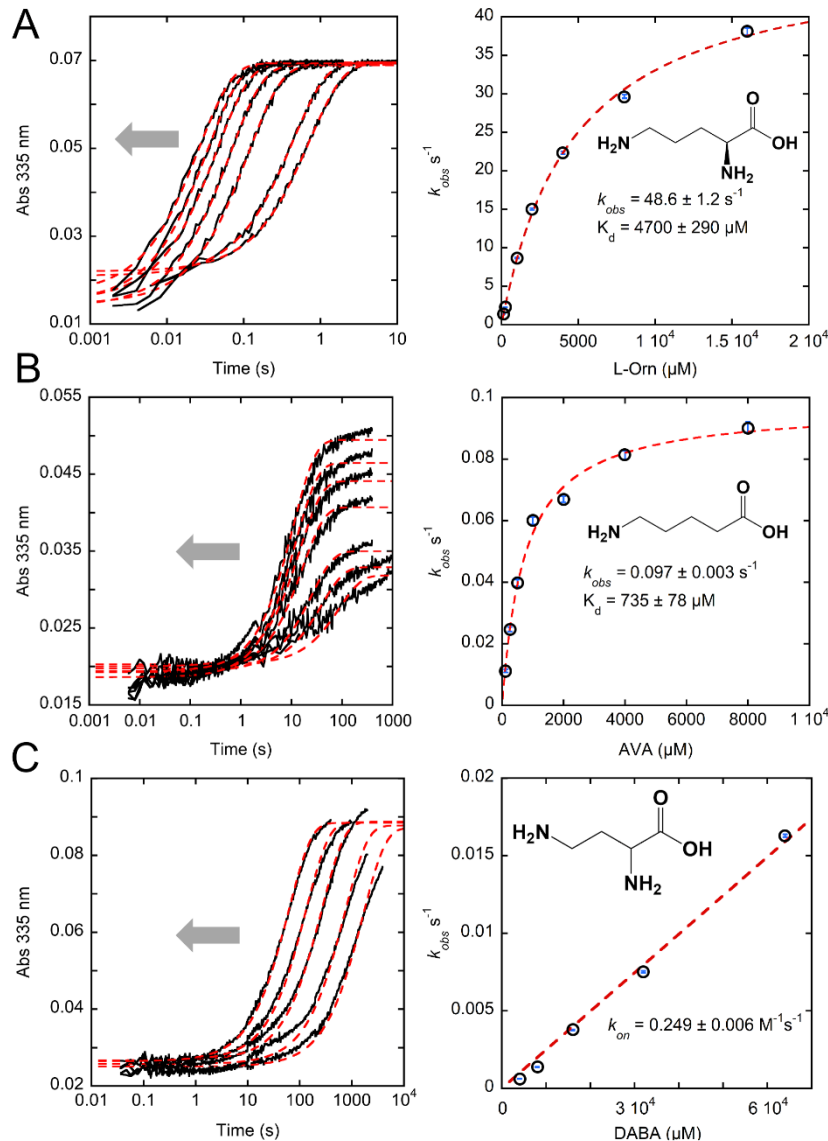


Figure 6. Transient-state absorption changes observed at 335 nm for *hOAT* reacting with L-Orn (A), AVA (B), and DABA (C). *hOAT* concentration for the reaction with L-Orn and AVA was 9 μM. For the studies with DABA, the enzyme concentration was 10.4 μM. The observed rate constants were plotted against substrate concentrations and fit to hyperbolic function (L-Orn, AVA, equation 3) or linear function (DABA, equation 4). The direction of the gray arrow in the plots to the left indicates the trend of substrate's concentration change towards higher values. The markers are shown as hollow black circles overlaying the blue relative error bars.

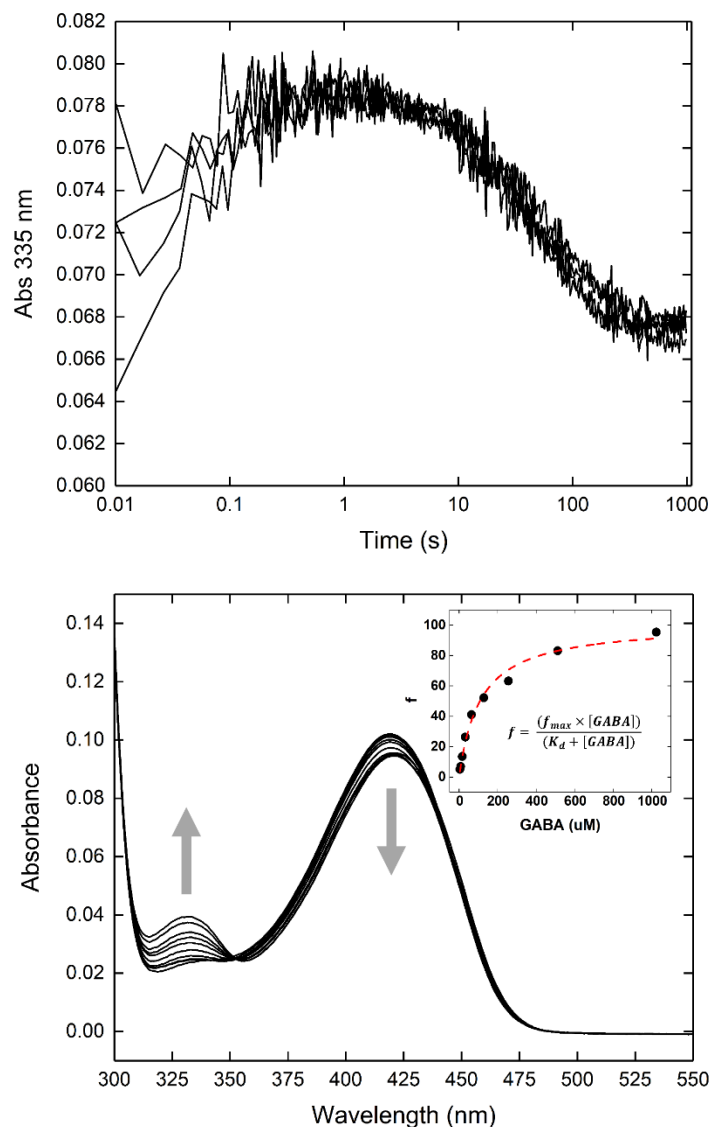


Figure 7. Top: Transient-state absorption changes observed at 420 nm for 9 μM (final) *hOAT* reacting with 250, 500, 1000, and 2000 μM (final) GABA. Bottom: The binding assay of 14.5 μM (final) *hOAT* with 4, 8, 16, 32, 64, 128, 256, 512, 1024 μM (final) GABA. In the top right corner is shown dependence of enzyme's fractional saturation from GABA concentration, the data were fit into hyperbolic curve.

For each ligand, including L-Orn, it was evident that an early step of the reaction was rate-limiting; hence, no intermediates after the formation of the external aldimine (that forms in

the dead-time) were observed. This early rate-limiting step is assigned to the conversion of the external aldimine to the quinonoid state. A comparison of the observed spectra with the initial spectra after the addition of the AVA, GABA or DABA, revealed a small red shift from ~420 nm to ~425 nm. This happened within the deadtime of the instrument and was assigned as the conversion of internal to external aldimine (Figure 8).

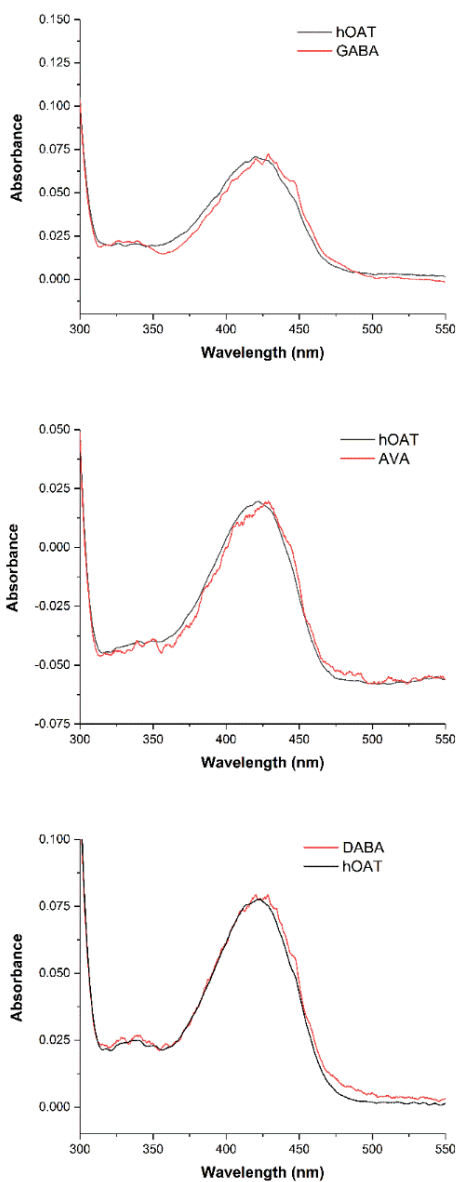


Figure 8. Comparison of the *hOAT* holoenzyme spectrum with the initial spectrum after addition of the 2 mM GABA (top), 1 mM AVA (middle), or 8 mM DABA (bottom).

The observed small red shift is a unique signal of the external aldimine formation for the alternative substrates. For L-Orn, the conversion of internal to external aldimine was less apparent than those of other ligands presumably because the structure of the external aldimine

complex closely resembles the internal aldimine tethered by the catalytic Lys292. Nevertheless, the existence of external aldimine in the reaction with L-Orn was validated through the following pH-dependent phenomena. The absorption spectra of 9 μM holo-*h*OAT were measured and compared at different pH values. No observable shift of the internal aldimine peak was detected. Then, initial absorption spectra of the reaction between 36 μM *h*OAT and 2 mM L-Orn at different pH values were compared (Figure 9). It transpired that the peak observed at ~ 420 nm at pH 9.0 is progressively shifted to ~ 425 nm at lower pH values. This transition was assigned to the different protonation states of the external aldimine, where the absorption peak of the protonated form is red-shifted compared to the deprotonated form.

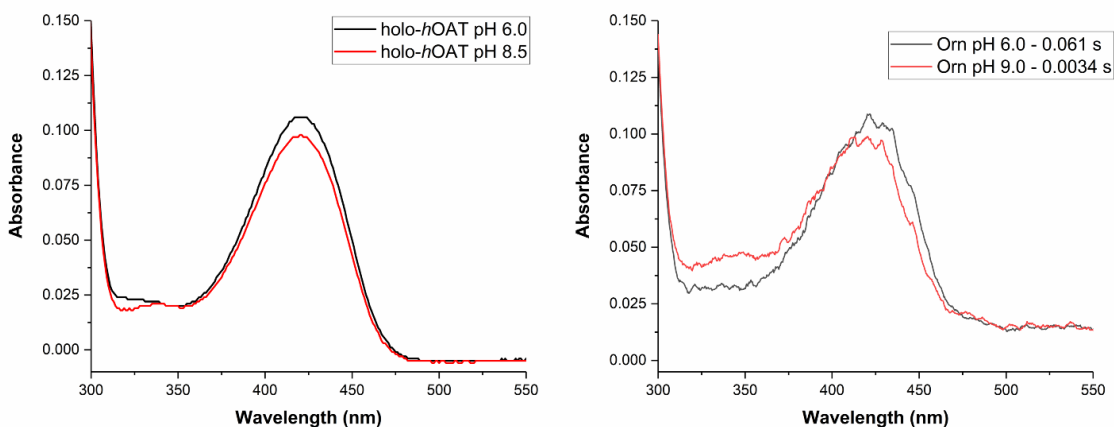


Figure 9. The absorption spectra of 9 μM holoenzyme *h*OAT at pH 6.0 and pH 8.5 (left). Initial absorption spectra of the reaction between 36 μM *h*OAT and 2 mM L-ornithine at pH 6.0 and pH 9.0.

The reaction traces with L-Orn, AVA, and DABA were fit into a single exponential (equation 2) to obtain sets of observed rate constants. For each substrate, the observed rates were

plotted against substrate concentrations and fit to a hyperbolic function (L-Orn, AVA, equation 3) or linear function (DABA, equation 4). The kinetic data are summarized in Table 1.

Table 1. Summary of kinetic parameters for *hOAT* using various substrates. N.D. = Not determined.

Ligand	Limiting rate constant (k_{lim})	Dissociation Constant (K_d)	k_{lim}/K_d
L-Orn	$48.6 \pm 1.2 \text{ s}^{-1}$	$4700 \pm 290 \text{ }\mu\text{M}$	$10,340 \pm 687 \text{ M}^{-1} \text{ s}^{-1}$
AVA	$0.097 \pm 0.003 \text{ s}^{-1}$	$735 \pm 78 \text{ }\mu\text{M}$	$131.9 \pm 14.6 \text{ M}^{-1} \text{ s}^{-1}$
DABA	N.D.	N.D.	$0.249 \pm 0.006 \text{ M}^{-1} \text{ s}^{-1}$
GABA	N.D.	$110 \pm 15 \text{ }\mu\text{M}$	N.D.

The native substrate L-Orn possesses the highest observed limiting rate constant and highest pseudo-second-order rate constant k_{lim}/K_d , which is a measure of substrate specificity in the first half-reaction. AVA exhibited a higher binding affinity to *hOAT*, ~6.4-fold that observed for L-Orn but reacted ~500-fold more slowly. For DABA, the dependence of the observed rate on substrate concentration was linear from 4 to 64 mM, indicating that the reaction of *hOAT* with DABA is either collision-based and/or has a diminished tendency to form the external aldimine state. The slope of the line either represents the true second order rate constant or is k_{lim}/K_d for DABA. If the latter is true, *hOAT* has ~41,500-fold less specificity for DABA than for L-Orn and ~530 times less for AVA.

Among the four substrates studied, GABA expressed the highest binding affinity towards *hOAT*. However, in reaction with GABA, the full decay of external aldimine was never achieved, even when the enzyme was fully saturated, possibly due to a bias in terms of binding

and rate for the second half-reaction returning the enzyme to the external aldimine state. The binding of GABA was confirmed spectrophotometrically by the rapid and small red shift of absorbance peak from ~420 nm (internal aldimine) to ~425 nm (external aldimine) within the deadtime of the instrument. The subsequent decay of external aldimine and formation of PMP went slowly and was completed in 1000 seconds (Figure S5). According to the observed change in the amplitude of the external aldimine at 425 nm, only a fraction of the enzyme accumulated as the PMP state at equilibrium (Figure S5). The K_d of GABA was measured separately (Figure S5) and was estimated to be $110 \pm 15 \mu\text{M}$, ~40 times lower than that for L-Orn and ~6 times lower than that for AVA.

Crystal structure of hOAT soaked with GABA and AVA

The transient-state kinetics of *hOAT* using alternative substrates suggest possible diversity in their binding modes and chemical mechanisms. Much like observations made for L-Orn, the decay rate of the external aldimine species is the rate-limiting process in the first half-reaction for all alternative substrates. Soaking experiments of holo-*hOAT* crystals were set up in an attempt to trap the reaction intermediates for all three compounds under the assumption that the catalysis may occur slowly *in crystallo*. For each ligand, the crystals were soaked for various time intervals from three minutes to an hour for AVA and DABA, and from 50 minutes to 2.5 hours for GABA. The crystals soaked with GABA for one hour and 30 minutes and the crystals soaked with AVA for 30 minutes, diffracted to similar resolutions of ~2.2 Å. DABA crystals had poor diffraction and were omitted from further structural analysis. Complex structures were solved by molecular replacement (search model PDB ID: 1OAT²⁵). The *hOAT*-GABA crystal structure was processed in the $P 3_1 2 1$ space group, while that of *hOAT*-AVA was processed as

P 3₂ 2 1. The active sites for structures of *h*OAT soaked with GABA and AVA are shown in Figure 10.

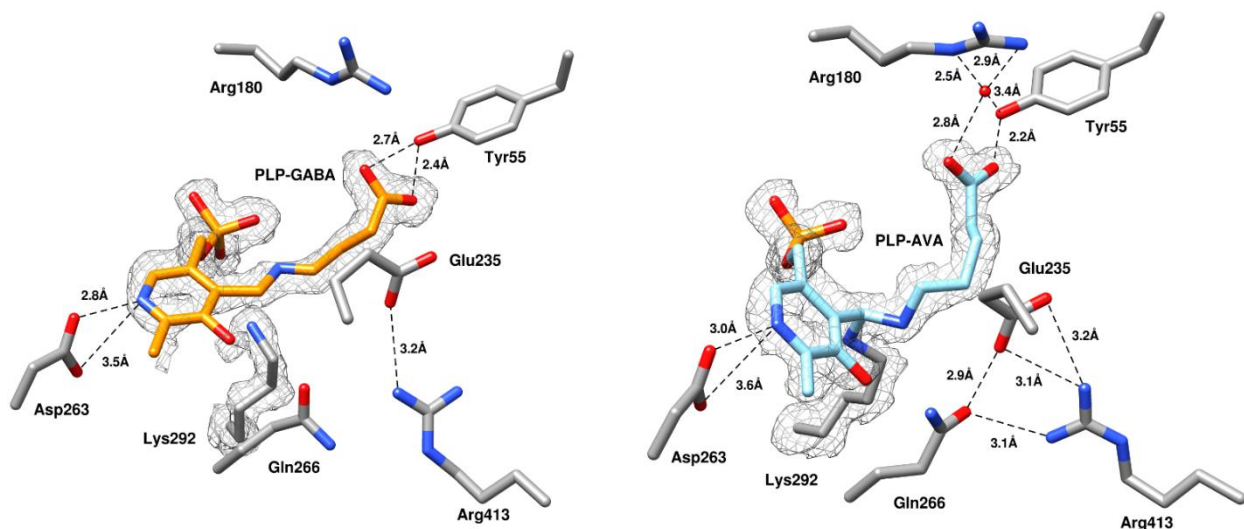


Figure 10. Polder map ($F_o - F_c$, at 3.0σ) of the *h*OAT structure soaked with GABA (left, PDB ID: 7TA1) and AVA (right, PDB ID: 7TA0). In both structures, the reaction intermediates of GABA and AVA with *h*OAT are shown within its active site. Based on the observed electron density and transient kinetic results, an external aldimine intermediate state was built for the reaction with GABA, while gem-diamine intermediate was built for the reaction with AVA. Dashed black lines indicate hydrogen bonds or charge interactions. Electron density maps are shown as gray mesh around the ligands and catalytic lysine.

In both soaking experiments, reaction intermediates were trapped. For GABA, an intermediate formed that exhibited a covalent linkage with PLP and was detached from the catalytic Lys292, a structure consistent with the proposed external aldimine intermediate. The carboxylate group of the ligand formed two hydrogen bonds with Tyr55 instead of interacting with Arg180, which is proposed to interact with the carboxylate of L-Orn³⁷. No other interactions were observed between the ligand and the active site residues. For two monomer copies in an asymmetric unit, the Glu235-Arg413 salt bridge that is a key feature in the holo-*h*OAT was

found partially disrupted: the side chain of Arg413 moved away from Glu235 and Gln266. In other monomer copies, the Glu235-Arg413 salt bridge remained intact. Previous kinetic experiments on GABA carried out by Markova et al.³³ showed that *h*OAT has the capacity to process GABA into succinic semialdehyde despite a low rate constant ($k_{\text{lim}} = 0.006 \pm 0.004 \text{ s}^{-1}$ at 25°C). Considering the exceedingly slow reaction rate, relatively short soaking time, and good fit of the model into the observed electron density, it can be concluded that the species observed in the structure is not a final adduct, but rather an external aldimine intermediate.

The structure of the *h*OAT crystal soaked with AVA revealed an intermediate that closely resembles the gem-diamine intermediate (Figure S1). Unlike other intermediates in a typical transamination reaction, gem-diamine is a species in which the catalytic lysine, the PLP, and the substrate are covalently joined together, and the observed electron density can be fit convincingly to such an intermediate state (Figure 10). The carboxylate group of AVA formed a strong hydrogen bond (measured as 2.2 Å) with Tyr55 and indirectly interacted with Arg180 through hydrogen bonds via a water molecule, and the Glu235-Arg413 salt bridge remained intact.

It also should be noted that in the soaking structure of AVA a strong tetrahedral electron density was detected in the proximity of Ser186, Met201, and Phe204 in two out of three monomer copies in the asymmetric unit (Figure 11).

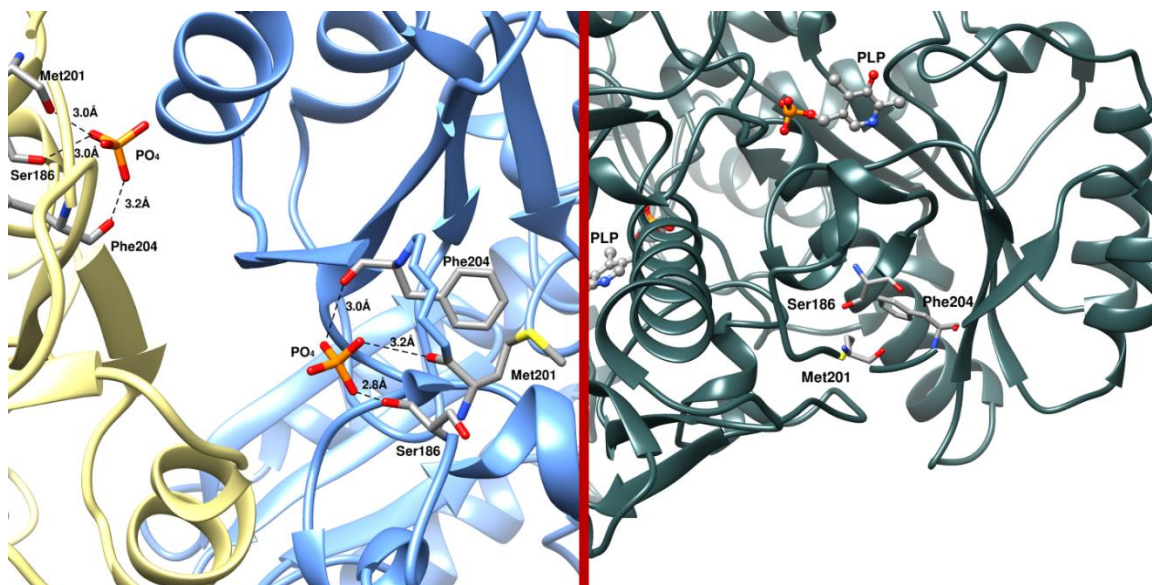


Figure 11. Comparison of the phosphate binding site in the crystal structure of *hOAT* soaked with AVA (left) and biological dimer of holoenzyme (right).

Out of all chemical species present in the crystallization conditions, only the phosphate group of PLP possesses the right geometry to fit into the observed electron density. The electron density elongates toward Asp205, but it becomes weaker extending from the tetrahedral center. For this reason, only the phosphoryl group of PLP was built and refined into the observed density. This phosphate-binding site is located at the interface of two monomers that are crystallographically adjacent creating a cavity where PLP could potentially bind. This cavity does not exist in the biological dimer of *hOAT*. In the biological dimer, the Ser186-Met201-Phe204 site is located on the surface of the enzyme, exposed to the bulk solvent. The electron density observed in the Ser186-Met201-Phe204 site likely represents a PLP bound only as a crystallographic artifact. Theoretically, the binding triad of Ser186, Met201, and Phe204 could interact with tetrahedral ligands such as phosphate in the biological dimer, but it is unclear whether this potential binding site is functional.

Discussion

Despite the fact that *h*OAT is an important target in anticancer therapy, many of its structural and mechanistic properties remain poorly described. In our current work, we attempted to address some of the fundamental questions associated with the substrate recognition, catalysis, and pH dependence of *h*OAT. Continued development of rationally designed mechanism-based inactivators of *h*OAT will be facilitated by an expanded understanding of the enzyme's structure and mechanism. Moreover, the discovery of various GABA analogs as potent and specific MBIs of *h*OAT prompted the investigation of the binding of GABA to the *h*OAT active site.

Virtually the same pKa values were determined for the initial and rate-limiting step of both the first and second half-reactions, suggesting that these dependencies arise from titration of the same group. Catalytic residue Lys292 is a candidate residue whose protonation state would critically influence multiple steps of the catalysis. For the first half-reaction, the rate is dependent on the abstraction of the proton from the δ -carbon of ornithine in the external aldimine state by the deprotonated amino group of Lys292. Hence, a basic pH facilitates the first half-reaction as Lys292 can more readily act as a general base to form the quinonoid intermediate (Figure 12).

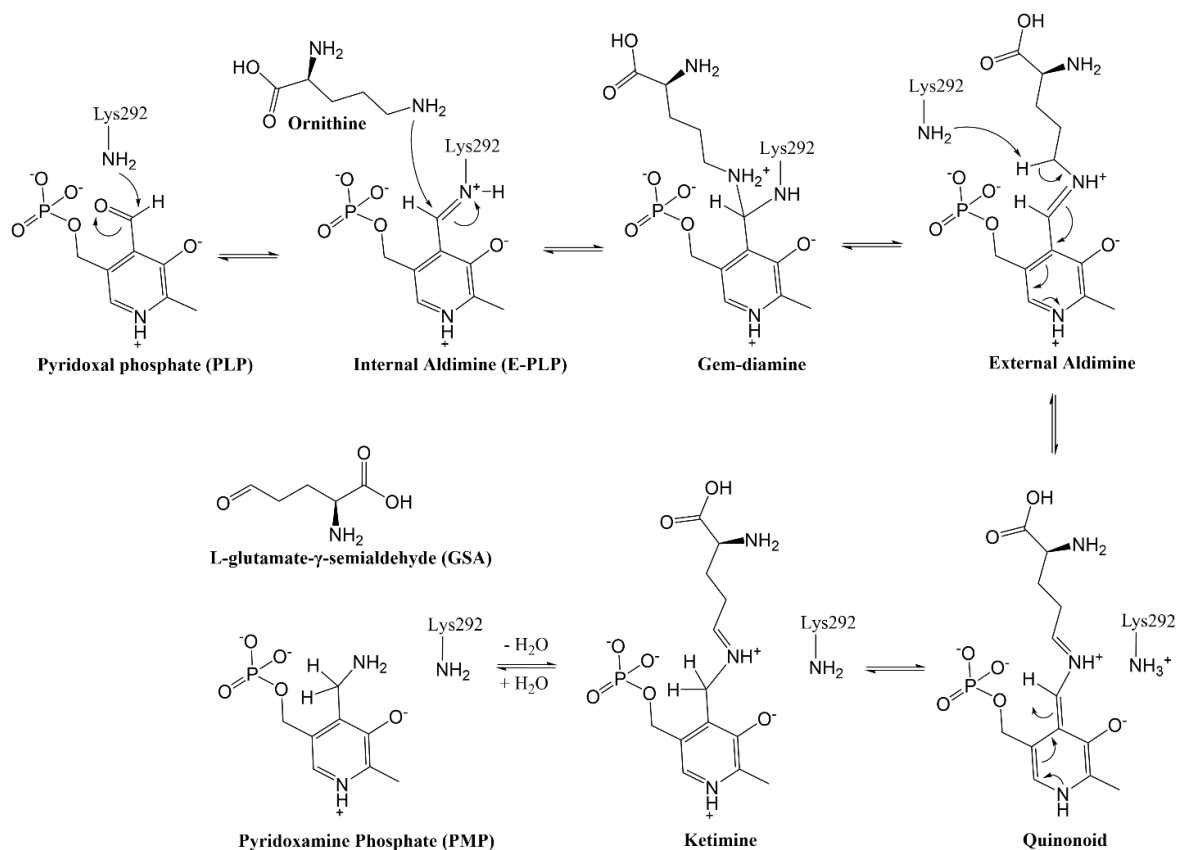


Figure 12. Simplified mechanism of reaction of *hOAT* with its native substrate L-ornithine.

In the second half-reaction, the rate likely depends on the formation of the PMP- α -KG Schiff base, which requires the amino group on the side chain of Lys292 to be in a protonated state. In the process of the ketimine formation, protonation of Lys292 lowers the pKa of the PMP amino group facilitating nucleophilic attack of the α -ketoglutarate carbonyl. Thus, it is conceivable that in both half-reactions, the protonation state of Lys292 governs the rate-limiting step.

The structure from *hOAT* crystallized at pH 6.0 revealed that the enzyme's active site has rearranged sidechain conformations that hinder ligand entry to the catalytic pocket. The side chains of Arg180 and Glu235 were found to deviate from their functional positions observed at

pH values above neutrality. At low pH, both residues partially occupy the L-Orn binding pocket. Almost no activity was observed with L-Orn at pH 6.6 and lower, but the second half-reaction with α -KG had the maximum reaction rate at pH values below 6.0 and decreased toward higher pH values. Despite the constriction of the active site pocket at low pH, α -KG is evidently able to react with the PMP form of the enzyme productively. Moreover, this observation may infer a critical role of Arg413 in facilitating the reverse reaction of *h*OAT. It is possible to surmise that once PMP is formed and the Arg413-Glu235 salt bridge is broken, the active site has a preference to bind α -KG for the second half-reaction through direct interaction with Arg413. This conformational constriction selectively inhibits the first half-reaction and ensures that the enzyme remains in a PLP form at low pH values.

*h*OAT can be found in almost all tissues of the human body, but it predominates in the liver (pH 7.0), kidney (pH 7.4), intestine (pH varies from ~6.0 to ~7.4), duodenum (pH 6.0), and retina (pH 7.2)³⁸⁻⁴¹. In most cases, *h*OAT is found in tissues where pH is below the determined kinetic pKa, in some cases by multiple pH units. In the most acidic conditions, the first half-reaction of *h*OAT with L-Orn would be ostensibly non-functioning. It should be noted, however, that in mammals, OAT localizes within the mitochondrial matrix where the pH is ~7.8⁴²⁻⁴³. Thus, the enzyme is likely less or nonfunctional outside the mitochondria, especially if intracellular/extracellular pH is lower than 7.8. Cancer cells are generally associated with higher values of intracellular pH (pH_i) of 7.12–7.65 (compared to pH_i 7.0–7.2 for normal cells)⁴⁴⁻⁴⁵. Such a rise in pH could result in activation of *h*OAT and acceleration of its first half-reaction without significant diminishment of the second half-reaction (Figure 2). Recently published work suggests that HCC cells are characterized by hydroxyproline accumulation and accelerated

consumption of L-proline¹⁹ resulting from an abnormal proline metabolism. At the end of its first half-reaction, *hOAT* produces L-GSA which cyclizes to form P5C, a precursor to *L*-proline. Thus, *hOAT* could serve as a regulator of HCC progression *via* the proline metabolic pathway¹⁸. For this reason, the pH dependence of *hOAT* may exacerbate its contribution to HCC progression.

Of the substrates studied, AVA and GABA demonstrated a tighter binding to *hOAT* than L-Orn. The turnover of AVA serves as a proof that the missing α -amino group doesn't prevent substrate's initial binding to the enzyme. In comparison to L-Orn, it appears that the α -amino group plays a crucial role in further catalysis since the observed reaction rate for L-Orn was ~500 times faster than for AVA. It's also important to note that the first half-reactions with L-Orn and DABA went to completion and didn't demonstrate significant reversibility unlike the fractional net conversion to predominant PMP form for the enzyme observed with AVA and GABA. The stopped-flow experiments with AVA showed the dependence of absorbance amplitudes at different ligand concentrations. We propose that the reaction is readily reversible based on the observation that ~50% of products are converted back to reactants when 8 mM of AVA is added (Figures 13, 14, 15).

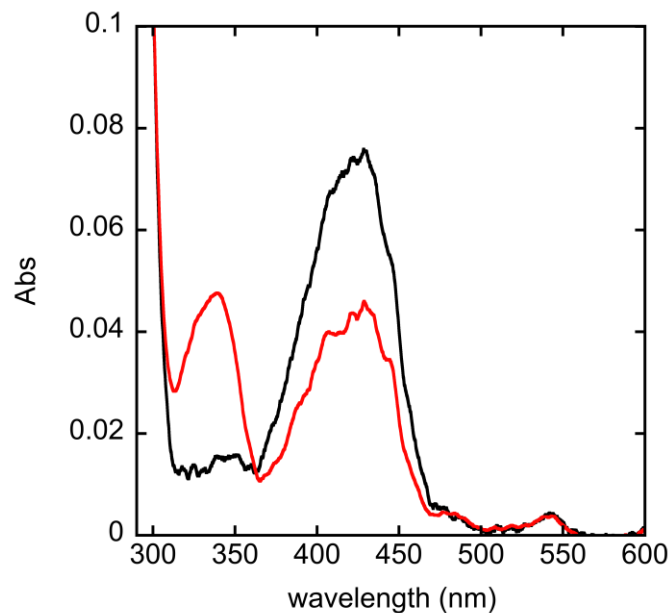


Figure 13. Initial (black) and final (red) spectra of the reaction between 8 mM AVA and 9 μ M *hOAT*.

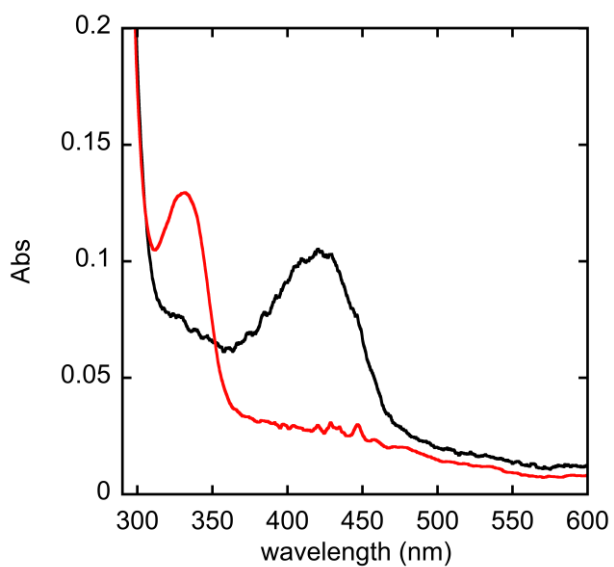


Figure 14. Initial (black) and final (red) spectra of the reaction between 8 mM DABA and 10.4 μ M *hOAT*.

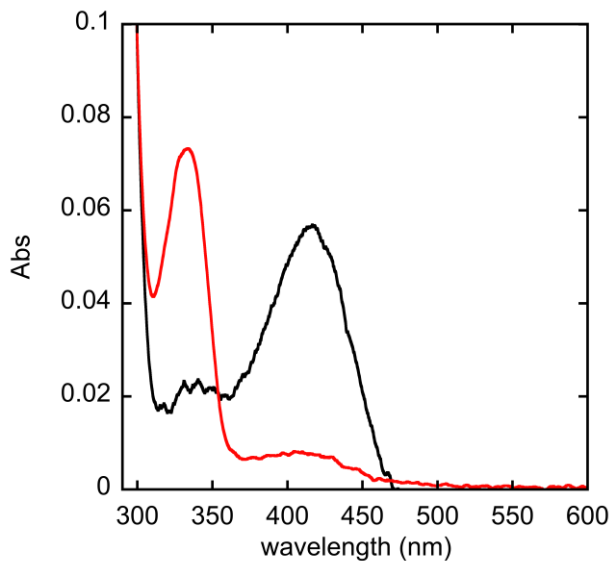
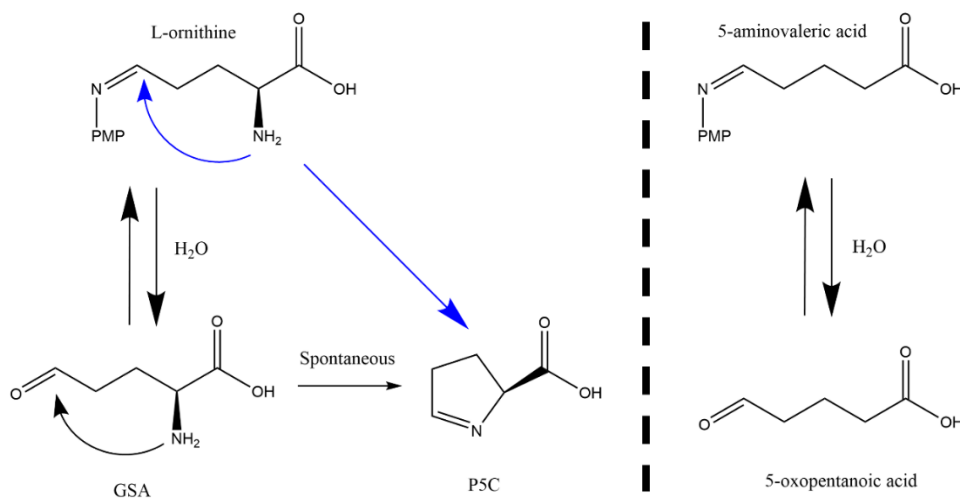


Figure 15. Initial (black) and final (red) spectra of the reaction between 8 mM L-ornithine and 9 μ M *h*OAT.

The reversibility of the reaction could be explained by the missing α -amino group in the structure of AVA. Due to the absence of the α -amino group, the reaction product of AVA, 5-oxopentanoic acid, cannot cyclize, unlike products from other substrates such as glutamate semialdehyde and 2-amino-4-oxobutanoic acid. As a result, it can react with PMP to form PLP and AVA. A similar result was observed for GABA; the reversibility of the GABA reaction catalyzed by *h*OAT is even more dramatic, displaying ~92% PLP at equilibrium in the presence of 1 mM GABA (based on the observed change in the amplitude of external aldimine at 423 nm).

The slow reaction rate of AVA could also indirectly support a hypothesis that the last reaction step of *h*OAT may not be solely hydrolysis followed by spontaneous cyclization of the product in solution. Instead, the dissociation of the ligand from PMP could also proceed through 5-exo-trig cyclization initiated by the nucleophilic attack of the α -amino group (Scheme 2)

before release. Moreover, we speculate that a faster product release route can be achieved via a cyclization step initiated by the α -amino group within the active site by bypassing a hydrolysis step and the formation of GSA. However, our data for *hOAT* with L-Orn indicate that the reaction comes to aldimine/PMP equilibrium at low pH values establishing L-GSA as the product of the reaction and that cyclization to P5C occurs in solution.



Scheme 2. Two potential pathways for cyclization in the last step of the forward half-reaction of *hOAT* (left). AVA, in turn, has only one possible way to dissociate from PMP: through hydrolysis.

For all *hOAT* ligands studied in this work, the transient-state kinetic experiments showed that an early step in all reactions was rate-limiting in the first half-reaction. The rate-limiting step corresponding to the decay of a species with an absorbance peak at ~ 425 nm likely indicates the conversion of external aldimine. The crystal soaking experiments with GABA and AVA revealed two different stable intermediates. The structure obtained by soaking with GABA could be equally well described by the external aldimine, quinonoid, or ketimine species. However, considering the transient-state data, the external aldimine appears to be the most probable

reaction intermediate to be observed in the crystal structure. For AVA, the observed structure correlates with a gem-diamine species. The gem-diamine intermediate found in the AVA crystal structure was not detected in the kinetic studies. This could mean that *in crystallo* the rate-limiting step of the *hOAT* reaction with AVA is the decay of the gem-diamine rather than the external aldimine. To the best of our knowledge, this is the first experimentally observed gem-diamine structure among all *hOAT* substrates.

AVA is a natural metabolite of L-lysine catabolism in the aminovalerate pathway in various bacteria⁴⁶. In some bacteria, it is involved in the L-proline anabolic pathway⁴⁷. It is also a normal metabolite present in human saliva. The elevated concentration of AVA is typically found in the mouths of patients with chronic periodontitis⁴⁸. Being a methylene homolog of GABA, AVA functions as a weak GABA agonist by interacting both with GABA_A (IC₅₀ = 4 μM) and GABA_B (IC₅₀ = 9 μM) receptors⁴⁹. In the context of *hOAT*, AVA acts as a slow substrate with a binding affinity ~6.4 times higher than that for L-Orn. In fact, its binding affinity is comparable and, in some situations, stronger than those of some known *hOAT* inactivators.

In the current work, structural and kinetic properties of *hOAT* were tested and analyzed. New important information concerning kinetic pK_a, potential routes for product cyclization, and roles of α- and δ- amino groups in substrate recognition and catalysis was obtained. The kinetic and structural results could enhance the foundation for the rational design of a new generation of *hOAT* inactivators. Specifically, the reported results revealed intrinsic information about the active site nucleophile Lys292, which often forms a covalent linkage attacking the electrophilic centers during MBI inactivation^{21-22, 29}. In addition, the results also provided a rationale that the potent GABA-mimicking MBIs follow the same binding mode as GABA. This supports the

notion that mimicking fragment-sized slow-reacting alternative substrates like GABA could be a more effective approach in structure-based drug design instead of mimicking the enzyme's native substrates (ornithine or glutamate).

As alternative substrates, GABA and AVA displayed potential inhibitory effects against an established drug target (*hOAT*) due to a combination of stronger binding affinity and slow turnovers. The data for AVA and GABA also lead to a hypothesis of an alternative catalytic mechanism in which a cyclization step bypasses hydrolysis of the ketamine state. Potentially, the “uncyclizable” analogs of GABA could be developed as inhibitory therapeutics against the cancer target *hOAT* if binding selectivity was achieved.

Experimental procedures

Expression and purification of human OAT

hOAT was expressed and purified according to previously published protocols³⁰. Briefly, *E. coli* BL21(DE3) cells containing the pMAL-*t-hOAT* plasmid were incubated at 37 °C with shaking in Lysogeny Broth (LB) medium supplemented with 100 µg/mL ampicillin. When the culture OD600 reached a value of 0.7, expression of the MBP-*t-hOAT* fusion protein was induced by the addition of 0.3 mM isopropyl β-D-1-thiogalactopyranoside and incubated for an additional 16–18 h at 25 °C. Cells were harvested by centrifugation, washed with buffer A comprised of 20 mM Tris-HCl, 200 mM NaCl, and 100 µM PLP, pH 7.4, frozen in liquid nitrogen, and stored at –80 °C. The frozen cell pellet was then thawed, sonicated in buffer A, and centrifuged at 40,000 x g for 20 min. The resulting supernatant was loaded onto an amylose affinity column pre-equilibrated with buffer A. The column was washed thoroughly, and the MBP-*t-hOAT* fusion protein was eluted from the column with 10 mM maltose. Fractions

containing the fusion protein were combined and treated with TEV protease to remove the MBP tag. The cleaved *hOAT* protein was collected and concentrated using a centrifugal filter. The protein was then further purified by size exclusion chromatography using a HiLoad Superdex-200PG column. The column was pre-equilibrated, and the protein was eluted in buffer containing 50 mM HEPES, 100 μ M PLP, and 300 mM NaCl, pH 7.5.

Transient-state experiments for pH studies

To ensure a constant osmotic pressure for experiments that required a range of pH values, a mixture of 50 mM MES, 50 mM acetic acid, 100 mM Tris, and 50 mM NaCl (MAT buffer) was used to buffer for pHs 5.0 - 9.3⁵⁰. For the forward *hOAT* reaction with L-Orn, the enzyme was buffer-exchanged into 1/20 MAT buffer, pH 7.5, and concentrated to 36 μ M. A separate 2/1 MAT buffer with 2 mM L-Orn was prepared and its pH was adjusted to 5.0 using concentrated acetic acid. Solutions with 36 μ M *hOAT* and 2 mM L-Orn were mounted into two separate syringes and loaded onto a Hitech Scientific (TgK) stopped-flow spectrophotometer. The absorption changes that occurred when these solutions were combined were observed at all wavelengths from 250 to 800 nm using charge-coupled device (CCD) detection at the temperature of 10°C. Depending on the pH, the time recorded for each reaction varied in accordance with the observed rate. For pH 5.8 spectra were recorded for 0.001-30 and 0.001-1600 seconds, for pH 6.0 to 6.6 spectra were recorded for 0.001-30 and 0.001-790 seconds, for pH 6.9 to 7.2, 0.001-1.5 and 0.001-317 seconds, for pH 7.5 to 7.8, 0.001-1.5 and 0.001-30 seconds, for pH 8.1 to 9.0, spectra were collected for 0.001-1.5 seconds. Kinetic data collected on two time-frames were spliced together at the limit of the shorter collection period to form composite datasets with time resolution sufficient to describe all events.

For pH studies of the second half-reaction of *h*OAT, the enzyme was buffer-exchanged to 1/20 MAT, pH 7.0 with 2 mM (final) L-Orn and left to react at 4°C for 16 hours. The PMP form of *h*OAT was then extensively buffer-exchanged to 1/20 MAT, pH 7.0. The protein was further concentrated to 24 μM by centrifugation using 10 kDa molecular weight cut-off filters (Amicon). A separate 2/1 MAT buffer with 2 mM α-KG was prepared and its pH was adjusted to 5.0 using concentrated acetic acid. Solutions with 24 μM *h*OAT and 2 mM α-KG were placed into two separate syringes and loaded onto the stopped-flow spectrophotometer. The absorption changes were observed at all wavelengths from 250 to 800 nm using a CCD detector at 10°C. Depending on the pH, the time recorded for each reaction varied in accordance with their observed rates and completeness. For pH 5.0 to 8.7 the spectrum was recorded for 0.001 - 1.5 seconds, for pH 9.0, 0.001 - 3 seconds, for pH 9.3, 0.001 - 8 seconds. Since reactant ratios establish pseudo-first-order conditions, the obtained data for 420 nm were extracted from the data set for each pH value and fit to a single exponential to obtain the observed rate constants (equation 1). In this equation, k_{obs} is the observed rate constant, Abs_t is 420 nm absorbance at time t , Abs_{end} is final absorbance at 420 nm, ΔAbs is the difference between the initial absorbance and the final absorbance (Abs_{end})

Equation 1:

$$Abs_t = \Delta Abs \cdot e^{(-k_{obs}t)} + Abs_{end}$$

The pH dependence of k_{obs} was fit into equation 2. K_a values determined from titratable phenomena X , (in this case k_{obs}) were determined by plotting the pH against k_{obs} ; where X_{AH} and X_{A^-} represent the respective fully protonated and unprotonated arms of the titration.

Equation 2:

$$X = \frac{(X_{AH}[H^+] + K_a X_{A^-})}{[H^+] + K_a}$$

Transient-state kinetics for hOAT substrate analogs

For the stopped-flow experiments, purified *hOAT* was buffer-exchanged into 100 mM HEPES, 50 mM NaCl, pH 7.5 buffer, and concentrated by centrifugation using 10 kDa molecular weight cut-off filters. For the single turnover experiments, three substrate analogs of *hOAT* were chosen: AVA, DABA, and GABA. Equivalent experiments were carried out on L-Orn as a control. For each ligand, a stock solution in 100 mM HEPES, 50 mM NaCl, pH 7.5 was prepared and two-fold serially diluted using the same buffer. Chemical reactions were observed using a stopped-flow spectrophotometer in combination with CCD in a range from 250 to 800 nm. For all reactions, the temperature was held constant at 20°C. For each set of experiments, *hOAT* and one of the ligands were mounted from two separate syringes onto the stopped-flow instrument where they were rapidly mixed at a 1:1 ratio. For the *hOAT* reaction with L-Orn, the final concentrations after mixing were: 9 μM *hOAT*, and 16 mM, 8 mM, 4 mM, 2 mM, 1 mM, 500 μM , 250 μM , 125 μM for L-Orn. For the *hOAT* reaction with AVA, the final concentrations after mixing were: 9 μM *hOAT*, and 8 mM, 4 mM, 2 mM, 1 mM, 500 μM , 250 μM , 125 μM AVA. For the *hOAT* reaction with DABA, the final concentrations after mixing were: 10.40 μM *hOAT*, and 64 mM, 32 mM, 16 mM, 8 mM, 4 mM DABA. For the *hOAT* reaction with GABA, the final concentrations upon mixing were: 9 μM for *hOAT*, and 2 mM, 1 mM, 500 μM , 250 μM , 125 μM GABA. The above reactant ratios establish pseudo-first-order conditions for all reactions. As such, the data for 335 nm obtained for L-Orn, AVA, and DABA were extracted from the data set for each and fit to a single exponential to obtain the observed rate constants (equation 1). In this equation, k_{obs} is the observed rate constant, Abs_t is 335 nm absorbance at

time t , Abs_{end} is final absorbance at 335 nm, ΔAbs is the difference between the initial absorbance and the final absorbance (Abs_{end}).

For each alternative substrate, the rates were plotted against the ligand's concentration and fit into hyperbolic (L-Orn, AVA, equation 3) or linear fit (DABA, equation 4). In equation 3, k_{obs} represents the observed rate constant, k_{lim} is the limiting rate constant, $[S]$ is the concentration of alternative substrate, and K_d is a dissociation constant. In equation 4, k_{obs} represents observed rate constant, k_{on} is association rate constant, $[S]$ is the concentration of alternative substrate, k_{off} is the dissociation rate constant.

Equation 3:
$$k_{obs} = \frac{(k_{lim} \times [S])}{(K_d + [S])}$$

Equation 4:
$$k_{obs} = k_{on} \cdot [S] + k_{off}$$

The K_d of GABA was measured in a separate titration experiment. 14.5 μ M (final) *hOAT* in 100 mM HEPES, 50 mM NaCl, pH 7.5 buffer was titrated with 4, 8, 16, 32, 64, 128, 256, 512, 1024 μ M (final) GABA and was allowed to react over 12,000 seconds. The absorbance spectrum was measured on a UV-Vis spectrophotometer from 250 to 700 nm. From the resulting data, a double-reciprocal plot of $1/[GABA]$ vs $1/\Delta Abs$ at 335 nm was made and fit into equation 5.

ΔAbs_{max} represents the maximum change in absorbance, $[GABA]$ is the concentration of GABA, K_d is dissociation constant.

Equation 5:
$$\frac{1}{\Delta Abs} = \frac{K_d}{\frac{1}{\Delta Abs_{max}} \times [GABA]} + \frac{1}{\Delta Abs_{max}}$$

The GABA concentration was plotted against the saturated fraction of *hOAT* and fitted into a hyperbolic curve (equation 6). In equation 6, f_{max} represents a fraction of fully saturated enzyme, $[GABA]$ is the concentration of GABA, K_d is dissociation constant.

Equation 6:
$$f = \frac{(f_{max} \times [GABA])}{(K_d + [GABA])}$$

hOAT holoenzyme pH 6.0 crystallization

Purified holo-*hOAT* was buffer-exchanged into 100 mM MES, 200 mM NaCl, 100 μ M PLP, pH 6.0 buffer, and then concentrated to \sim 6 mg/mL. The crystallization was performed via the hanging drop vapor diffusion method according to previously published conditions with 50 mM Tricine pH 7.8 substituted to 50 mM MES pH 6.0 buffer. The crystals grew at room temperature within three days and reached their maximum size in a week. The crystals had cubic morphology with the largest dimension of \sim 0.3 mm. Once no further growth of crystals was observed, they were transferred into cryoprotectant solution (well solution + 30% glycerol) and flash-frozen in liquid nitrogen.

hOAT crystal soaking with GABA and AVA

Once *hOAT* was purified, it was transferred to a 10 kDa centrifugal filter tube and concentrated to \sim 6 mg/mL. The holoenzyme crystals were first grown via a hanging drop vapor diffusion method. Each drop contained 2 μ L of protein and 2 μ L of well solution. The best crystallization condition contained 8% PEG 6000, 100 mM NaCl, 5% glycerol, and 50 mM Tricine pH 7.8. Once holoenzyme crystals reached their maximum size within seven days, 1 μ L of 10 mM GABA or AVA was added to the drop with crystals. The crystals were soaked for different time periods from 3 to 59 minutes for AVA and from 50 minutes to 2.5 hours for GABA. After soaking, crystals were transferred into a cryoprotective solution (well solution supplemented with 30% glycerol), and then flash-frozen in liquid nitrogen.

X-ray diffraction and data processing

Monochromatic X-ray diffraction data were collected at the LS-CAT beamline 21-ID-D at the Advanced Photon Source at Argonne National Laboratory. Data were collected at a wavelength of 1.127 Å and a temperature of 100 K using a Dectris Eiger 9M detector. Data sets were processed and analyzed with autoPROC⁵¹ or iMosflm⁵² software.

Model building and refinement

The *hOAT* structure was solved by molecular replacement using PHASER⁵³ in Phenix⁵⁴. The starting search model was the previously published structure of *hOAT* (PDB code: 1OAT). The model building and refinement were accomplished in Coot⁵⁵ and Phenix, respectively, as an iterative process until the lowest possible $R_{\text{free}}/R_{\text{work}}$ factor values were attained. Structural depiction figures were prepared using UCSF Chimera⁵⁶.

Table 2. Statistics of the crystal structures of holoenzyme *h*OAT crystallized at pH 6.0, soaked with AVA, and soaked with GABA.

Complex	<i>h</i> OAT: holoenzyme, pH 6.0	<i>h</i> OAT: AVA soaking	<i>h</i> OAT: GABA soaking
PDB code	7T9Z	7TA0	7TA1
Space group	C 1 2 1	P 3 ₂ 2 1	P 3 ₁ 2 1
Cell dimension			
α, β, γ (deg)	90.0, 106.4, 90.0	90.0, 90.0, 120.0	90.0, 90.0, 120.0
a, b, c (Å)	200.9, 110.8, 56.9	114.9, 114.9, 185.1	114.6, 114.6, 349.3
Processed Resolution (Å)	2.15	2.33	2.20
Rmerge ^a (%)	16.9 (121.4)	48.7 (524.4)	18.7 (182.4)
Rpim ^c (%)	10.3 (73.8)	12.8 (135.3)	8 (84.1)
I/σ (I)	4.9 (1.2)	7.0 (0.8)	6.7 (1.0)
CC ½ ^d (%)	98.6 (37.1)	99.4 (33.0)	99.3 (41.7)
Completeness (%)	92.5 (90.2)	99.9 (100.0)	99.8 (99.9)
Multiplicity	3.4 (3.4)	15.3 (16.0)	6.1 (5.4)
No. Reflections	258822 (14325)	939082 (47999)	1075016 (137321)
No. Unique Reflections	75968 (4201)	61264 (2995)	177531 (25577)
Refinement			
Rwork ^e /Rfree ^f (%)	27.6/28.0	21.3/23.5	25.3/27.1
No. of Atoms			
protein	9458	9440	18951
ligand	45	106	118
water	576	325	896
B factors (Å ²)			
protein	23.0	45.0	39.0
RMSD ^g			
bond lengths (Å)	0.66	0.55	0.82
bond angles (deg)	0.006	0.002	0.005
Ramachandran plot (%)			
favored	97.0	95.0	95.0
allowed	3.0	4.9	4.8
outliers	0.0	0.1	0.2
^a $R_{\text{merge}} = \sum I_{\text{obs}} - I_{\text{avg}} / \sum I_{\text{avg}}$ ^b The values for the highest-resolution bin are in parentheses ^c Precision-indicating merging R ^d Pearson correlation coefficient of two “half” data sets ^e $R_{\text{work}} = \sum F_{\text{obs}} - F_{\text{calc}} / \sum F_{\text{obs}}$ ^f Five percent of the reflection data were selected at random as a test set, and only these data were used to calculate R_{free} ^g Root-mean square deviation			

CHAPTER TWO

STRUCTURAL AND TRANSIENT KINETIC ANALYSES REVEAL THE DUAL INHIBITION MODES OF HUMAN ORNITHINE AMINOTRANSFERASE BY (1*S*,3*S*)-3- AMINO-4-(HEXAFLUOROPROPAN-2-YLIDENYL)-CYCLOPENTANE-1-CARBOXYLIC ACID (BCF₃)

Summary

Hepatocellular carcinoma (HCC) is the most common form of liver cancer and the leading cause of death among people with liver cirrhosis. HCC is typically diagnosed in advanced stages when tumors are resistant to both radio- and chemotherapy. Human ornithine aminotransferase (*hOAT*) is a pyridoxal-5'-phosphate (PLP)-dependent enzyme involved in glutamine and proline metabolism. Because *hOAT* is overexpressed in HCC cells and a contributing factor for the uncontrolled cellular division that propagates malignant tumors (Ueno, *A. et al., J. Hepatol.* 2014, *61*, 1080-1087), it is a potential drug target for the treatment of HCC. (1*S*,3*S*)-3-Amino-4-(hexafluoropropan-2-ylidene)-cyclopentane-1-carboxylic acid (BCF₃) has been shown in animal models to slow the progression of HCC by acting as a selective and potent mechanism-based inactivator of OAT (Zigmond *et al., ACS Med. Chem. Lett.* 2015, *6*, 8, 840–844). Previous studies have shown that the BCF₃-*hOAT* reaction has a bifurcation in which only 8% of the inhibitor inactivates the enzyme while the remaining 92% ultimately acts as a substrate

and undergoes hydrolysis to regenerate the active PLP form of the enzyme. In this chapter, the rate-limiting step of the inactivation mechanism was determined by stopped-flow spectrophotometry and time-dependent ^{19}F -NMR experiments to be the decay of a long-lived external aldimine species. A crystal structure of this transient complex revealed both the structural basis for fractional irreversible inhibition and the principal mode of inhibition of *hOAT* by BCF_3 , which is to trap the enzyme in this transient but quasi-stable external aldimine form.

Introduction

Aminotransferases represent a group of PLP-dependent enzymes that use a “Bi-Bi, Ping-Pong” mechanism to catalyze the transfer of an amino group, typically donated by an amino acid, to an acceptor α -keto acid⁵⁷⁻⁵⁹. In the first half-reaction, an amino acid is oxidized with the concomitant reduction of the PLP coenzyme to pyridoxamine-5'-phosphate (PMP). In the second half-reaction, the amino group from PMP is transferred to a suitable α -keto acid acceptor with the concomitant oxidation of PMP to regenerate the PLP coenzyme. The transamination mechanism of *hOAT* exhibits these two canonical half-reactions, with the conversion of L-ornithine and PLP to glutamate- γ -semialdehyde and PMP followed by the conversion of α -ketoglutarate and PMP to L-glutamate and PLP.

hOAT in mammals is transported into the mitochondrial matrix and is in high abundance in the brain, intestines, kidneys, and liver. It functions at a nexus for multiple metabolic pathways including glutamine metabolism, proline synthesis, and the urea cycle⁶⁰. Knockout experiments of the *oat* gene revealed that OAT may not have an important role in mitosis within normally developing cells⁶⁰. However, studies by Wang et al. have implicated *hOAT* in the

assembly of the mitotic spindle in human cancer cells⁶¹. Complex coordination of the components of the mitotic spindle is essential for successful separation of the sister chromatids. Moreover, inhibition of OAT is expected to diminish cellular glutamate and proline, both of which are important metabolites in neoplastic cells. Therefore, inhibition of *hOAT* is one path to slow cell division in cancer cells.

Mehta et al.⁵⁸ performed a sequence alignment of 14 aminotransferases, including GABA aminotransferase (GABA-AT), L-aspartate aminotransferase (Asp-AT), and *hOAT*, and found that while they share low sequence identity, the available structures indicate highly similar tertiary folds^{57, 62}. The highly conserved residues in the active sites of different aminotransferases make it difficult to selectively inhibit one enzyme without generating off-target reactivity and associated toxicity. Known irreversible inhibitors for both OAT and GABA-AT, such as gabaculine and 4-amino-5-hexynoic acid, indicate that available inactivators lack desired selectivity⁶². Although active site residues may be conserved, aspects of the chemical mechanism of each enzyme are unique. Therefore, the key to the rational design of a selective inactivator of an aminotransferase is based on an understanding of the specific chemistry involved.

that showed promising results for suppression of HCC tumor growth in athymic mice implanted with human-derived HCC¹⁸. BCF₃ covalently and irreversibly modifies both the catalytic lysine 292 and PLP, forming a tethered tertiary adduct that inactivates the enzyme. The currently proposed inactivation mechanism of BCF₃ lacks experimental proof for the proposed intermediate complexes, and the rate-limiting step was hitherto yet to be identified⁶³. To better understand the nature of *h*OAT as a drug target and facilitate the rational design of agents active against HCC, it is essential to quantitatively establish and verify the mechanism of BCF₃ inhibition. This work presents an investigation of *h*OAT inactivation by BCF₃ using a combined approach of transient-state kinetics and X-ray crystallography. The conclusions we have drawn incorporating the data from these additional methodologies are summarized in Scheme 3.

Results

Mechanism-based inactivators commandeer the chemical mechanism of an enzyme to covalently and irreparably alter functional groups in the active site⁶⁴. The rational design of covalent inactivators based on a detailed understanding of the chemical mechanism has great potential for drug discovery, as such an approach builds in both potency and specificity simultaneously. Methods to verify the chemistry of such inactivators most often include inhibition assays, mass spectrometry and X-ray crystallography⁶⁵⁻⁶⁹. Although these approaches have been successful in evaluating the inactivation mechanisms of PLP-dependent enzymes, the amenability of such enzymes to transient-state approaches allows for more comprehensive evaluation of the mechanism of inactivation, particularly those that exhibit multiple intermediates and partitions.

PLP-dependent transaminase reactions are often studied by spectrophotometric transient-state measurements as they exhibit predictable sequences of spectrophotometrically identifiable intermediates with absorption transitions from 300-650 nm⁷⁰⁻⁷². Such approaches can be quite definitive, identifying signature spectra of known intermediate states. However, the identity of new intermediates or reaction endpoints cannot be based solely on absorption spectra. For such species, it is necessary to employ complementary approaches in parallel to define the chemistry that is occurring. The kinetics of the BCF₃ inhibition of *h*OAT has rates that span seven orders of magnitude (Scheme 3) and, therefore, can be studied by spectroscopic methods that have fast and slow integration times. Here we employ rapid mixing spectrophotometric, time-dependent NMR, and steady-state X-ray crystallography/crystal-soaking methods to reveal the detailed inhibition mechanism of *h*OAT reacting with BCF₃.

Transient State Measurements of hOAT Inactivation by BCF₃

A combination of spectrophotometric and NMR measurements was used to capture the kinetics of the inhibition of *hOAT* by BCF_3 . This inhibition process had previously been characterized by mass spectroscopy and X-ray crystallography⁶³. The approach used here takes advantage of the highly conjugated species that occur sequentially in the inactivation reaction in combination with additional X-ray structural data (see below). These measurements provide a more complete assignment of the inactivation chemistry of *hOAT* by BCF_3 . Titration of *hOAT* with BCF_3 modulated the rate of accumulation of a quinonoid intermediate observed maximally at 567 nm (Figure 16).

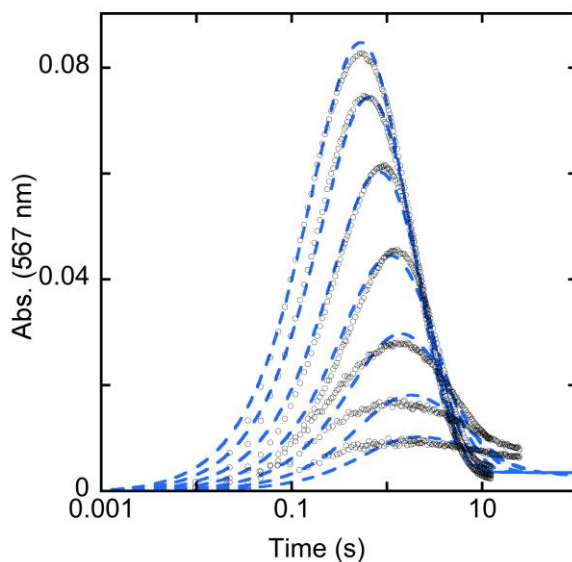


Figure 16. Transient state absorption changes observed at 567 nm for *hOAT* reacting with BCF_3 . *hOAT* ($9.84 \mu\text{M}$) was allowed to react with BCF_3 ($63, 127, 254, 508, 1016, 2035, 4065 \mu\text{M}$) and CCD spectra were collected on two timeframes ($0.009\text{--}12.3$ seconds for concentrations $63, 127, 254 \mu\text{M}$, and $0.02\text{--}24$ sec for concentrations $508, 1016, 2035, 4065 \mu\text{M}$). The extracted 576 nm data were fit to a linear model shown in beige in Scheme 4 and returned the rate constants shown in Scheme 3.

The formation and decay of this intermediate could be fit to a reversible three-step model shown in beige on Scheme 4 and the rate constants returned from the fit are shown in Scheme 3. The observed rate of formation of the quinonoid is a function of the extent of population and rate of decay of the preceding external aldimine species (see below). As such these data report both on the individual rate constants for formation and decay of three species and the prior equilibrium for formation of the initial external aldimine. The global fit gave rate constants of $k_1 = 1.5 \times 10^5 \pm 3 \times 10^4 \text{ M}^{-1} \text{ s}^{-1}$, $k_{-1} = 421 \pm 64 \text{ s}^{-1}$ for formation of the external aldimine I (Scheme 3). The dissociation constant for the reversible formation of this species was therefore $3.0 \pm 0.5 \text{ mM}$. The subsequent formation of the quinonoid species was described by rate constants $k_2 = 6.18 \pm 0.24 \text{ s}^{-1}$ and $k_{-2} = 0.81 \pm 0.02 \text{ s}^{-1}$. The irreversible decay of the quinonoid was fit to yield a rate constant of $k_3 = 0.74 \pm 0.01 \text{ s}^{-1}$.

Three-dimensional CCD data recorded for a single concentration of BCF_3 (Figure 17A) were fit globally using SVD to deconvolute and define pure spectra of the intermediates observed (Figure 17B). These data were fit to a simplified three-step irreversible model and thus did not include evidence of reversibility. The rate constants obtained from the fit agree well with those determined from the single wavelength analysis at 567 nm ($k_2 = 5.13 \pm 0.03 \text{ s}^{-1}$ and $k_3 = 0.51 \pm 0.01 \text{ s}^{-1}$).

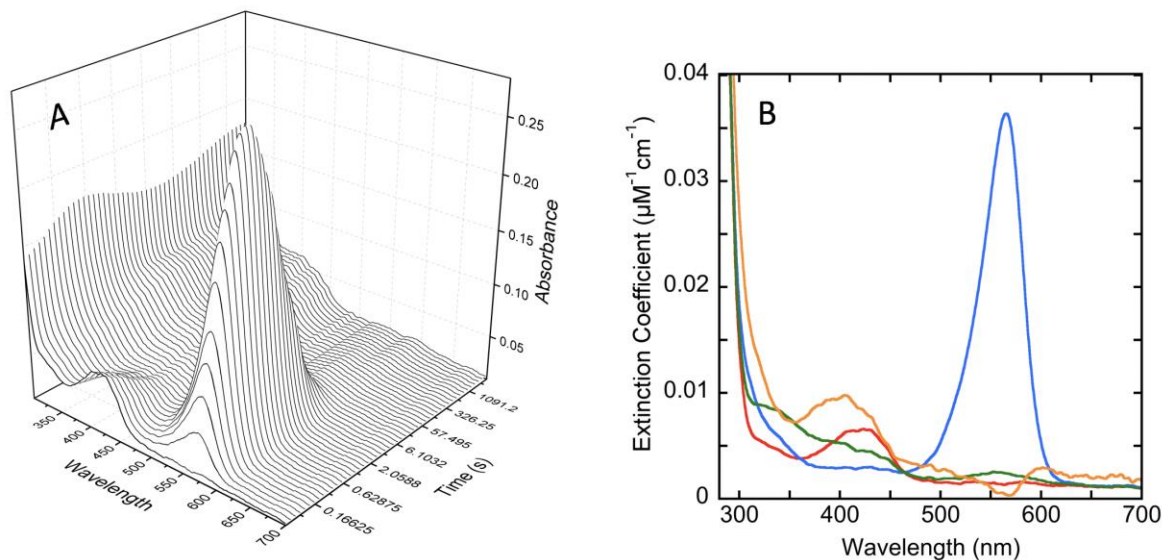


Figure 17. Transient state CCD data for *hOAT* reacting with BCF_3 . A. *hOAT* ($9.84 \mu\text{M}$ final) was mixed with BCF_3 ($4065 \mu\text{M}$) and CCD spectra were collected on two timeframes (0.0025 – 12.5, 15-2500 sec) and spliced together at ~ 12 sec to form a single data set for analysis. The data were fit using the SVD routine available in KinTek Explorer software to a linear model shown in green in Scheme 4, where the last rate constant was fixed to that determined from the time-dependent NMR data shown in Figure 18 and returned rate constants shown in Scheme 3. B. Spectra shown are the deconvoluted spectra assigned as follows: red; external aldimine I, blue; quinonoid I, green; external aldimine II, and orange; pyridoxal 5'-phosphate.

As described above, the final step k_4 was fixed to the value measured by transient state ^{19}F -NMR spectrometry. Time-dependent ^{19}F -NMR signals were fit using the SVD module of KinTek Explorer software (Figure 18) and returned a rate constant of $0.00015 \pm 0.00003 \text{ s}^{-1}$. This value is a net rate that describes a bifurcation and includes events for the decay of the external aldimine II species that liberates PLP (Scheme 3) and the rate of formation of the covalently modified *hOAT*. Prior data indicated that in any one turnover, 92% of the reaction yields PLP^{63} ; as such, the two rate constants diverging from the bifurcating step are summed from this rate and are $k_{\text{cat}} = 0.00014 \text{ s}^{-1}$ and $k_{\text{inact}} = 0.00001 \text{ s}^{-1}$. These values describe the rates for substrate and inhibitor roles of BCF_3 , respectively. The dominant path for decay of external

aldimine II reinstates the PLP form of the cofactor permitting subsequent turnovers with BCF_3 . This net rate constant is four orders of magnitude slower than any other step which dictates that the BCF_3 turnover rate is defined by this value (k_{cat}). That no other spectrophotometrically conspicuous species, such as a subsequent quinonoid state, are observed suggests that the measured k_{inact} can be ascribed specifically to the first step in the inhibitory path for decay of external aldimine II.

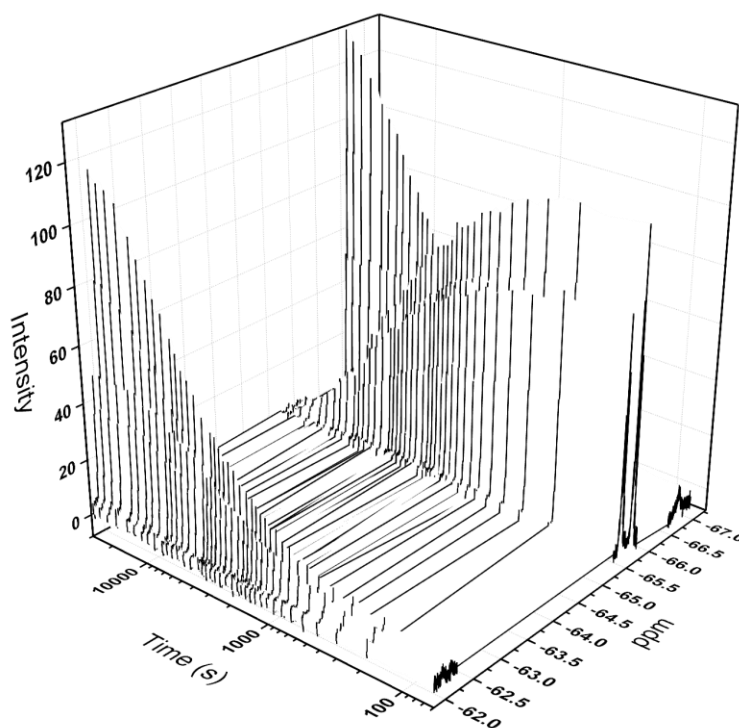


Figure 18. Transient state nuclear magnetic resonance changes observed for *hOAT* reacting with BCF_3 . *hOAT* ($333 \mu\text{M}$ final) was mixed with BCF_3 ($247 \mu\text{M}$) and ^{19}F spectra (16 scans per spectrum) were collected every 1 min for 8 h. The spectra were culled to approximate a logarithmic time base and were fit simultaneously to a linear $\text{A} \rightarrow \text{B}$ model that returned a rate constant of $0.00015 \pm 0.00003 \text{ s}^{-1}$.

The transient-state single turnover NMR spectral data report only on the slow steps of the *hOAT* – BCF_3 reaction. The initial spectrum obtained at ~ 300 sec is assigned as external

aldimine II. This state of the reaction has eliminated one fluorine as a fluoride (by integration) that is observed at -120 ppm (Figure 19).

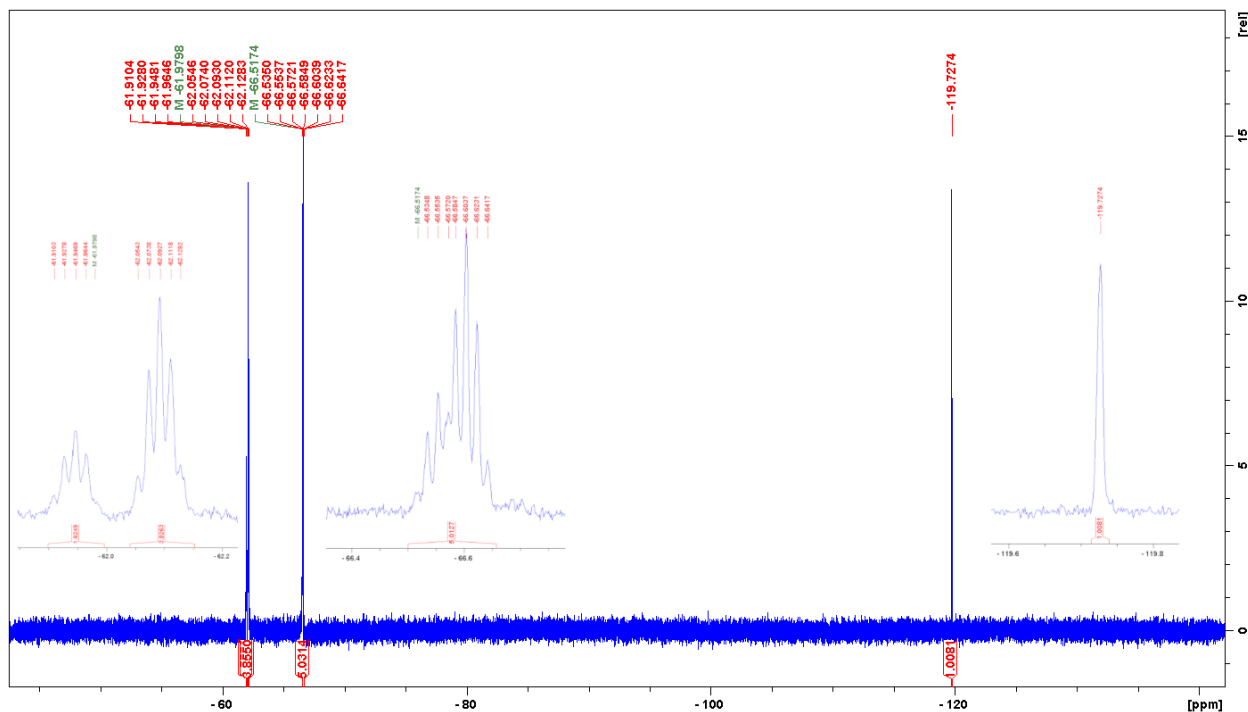


Figure 19. ^{19}F -NMR spectrum of *h*OAT- BCF_3 inactivation reaction after 8 hours. Four sets of peaks are observed: one corresponds to the free fluoride ion (singlet), two other sets of resonances are for two catalytic products derived from pathway *a* in Scheme 2. ^{19}F -NMR (CFCl_3 , 471 MHz, 283.2°K): δ -119.73 (s, F, F⁻), δ -66.60 (ddd, 3F, *E*- CF_3 , $J = 9$ Hz, ddd, 3F, *Z*- CF_3 , $J = 9$ Hz), δ -62.10 (dq, 2F, *E*- CF_2H , $J = 9$ Hz), δ -61.94 (dq, 2F, *Z*- CF_2H , $J = 9$ Hz).

The elimination of the single fluorine conceivably could occur to yield the *E* or *Z* configuration about the exocyclic vinylic bond at external aldimine II. That one set of NMR signals is observed at 300 sec indicates that the external aldimine II species is permitted free rotation within the active site (Figure 20).

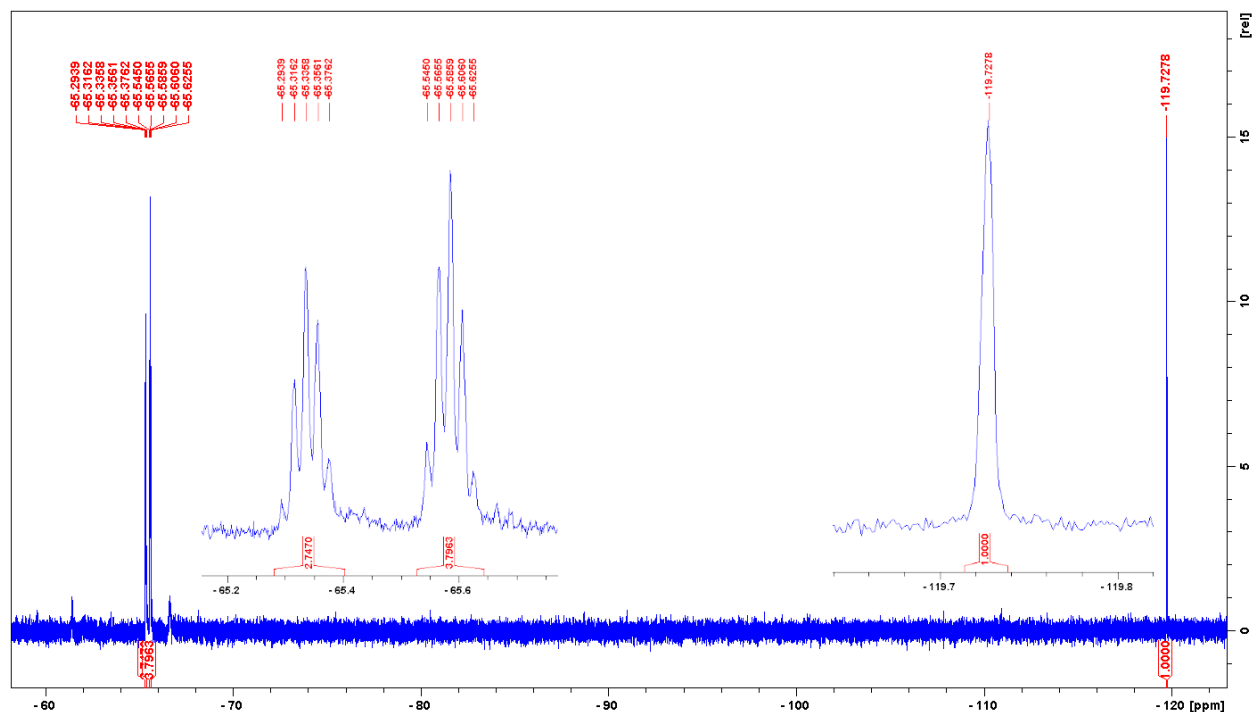


Figure 20. ^{19}F -NMR spectrum of the *hOAT* reaction with BCF_3 after 5 minutes. Three distinguishable sets of peaks are observed, which correspond to two species: free fluoride ion (singlet) and external aldimine II intermediate (doublet of doublet of doublets and doublet of quartets): ^{19}F -NMR (CFCl_3 , 471 MHz, 283.2°K): δ -119.73 (s, F, F^-), δ -65.58 (ddd, 3F, CF_3 , $J = 9$ Hz), δ -65.34 (dq, 2F, CF_2 , $J = 9$ Hz).

These signals resolve to products with two configurations by 480 min, both of which have a predicted mass equivalent to the mass determined for this product(s) in prior studies with BCF_3 ⁶³. While the proportion of E and Z configurations of the turnover products cannot be known by these methods, the structure of the covalently inhibited state indicates that only the E configuration formed by nucleophilic attack by Lys292 is able to bring about irreversible *hOAT* inhibition (Scheme 3)⁶³.

Crystal structure of hOAT inhibited by BCF₃

Holoenzyme *hOAT* crystals were obtained in 3 days and had hexagonal prism morphology with the largest dimension of ~ 0.4 mm. The crystals were stable during soaking and diffracted to

1.96 Å resolution. After molecular replacement and refinement, the best refined molecular model had three monomers in an asymmetric unit in the $P3_221$ space group (Table 1). The biological assembly of *hOAT* is a typical homodimer which can be reconstructed using the symmetrically related subunit in the crystal lattice (Figure 21).

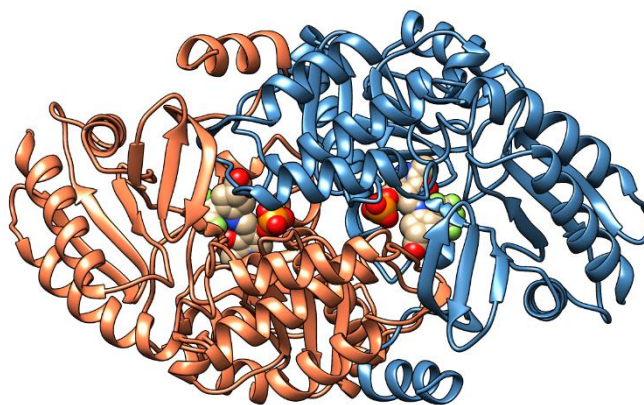


Figure 21. The structure of *hOAT* homodimer in the external aldimine II state. The biological assembly is reconstructed by adding a crystallographically symmetric monomer (blue) to an observed monomer (orange) in an asymmetric unit using Coot. The active site locations are indicated by the bound external aldimine II shown in space filling form.

The decay of external aldimine II is exceedingly slow compared to all prior steps observed. For this reason, we attempted to trap this intermediate by soaking. Crystallized *hOAT* was soaked with 1 mM BCF_3 (1 μL added to a 4 μL hanging drop) for 40 min and then frozen in liquid nitrogen. Given that the decay of the external aldimine II intermediate is rate limiting for both BCF_3 inactivation and turnover, the majority fraction of *hOAT* will accumulate as external aldimine II in the presence of excess BCF_3 . The active site structure of *hOAT* soaked with BCF_3

is shown in Figure 22 and compared with the structure of the covalently inhibited state of *hOAT* determined previously⁷ (pathway *b*, Scheme 3). The density observed in the active site was interpreted as the external aldimine II intermediate. The electron density supports that PLP has been covalently modified while the conserved Lys292 is detached from the PLP-inactivator adduct. The resolution of these structural data (1.96 Å) permitted definitive assignment of the five remaining fluorine atoms in this adduct (Figure 23). At this stage of the reaction, Lys292 is available for a nucleophilic attack either at the PLP imine carbon or the carbon of a difluoromethylenyl group (pathway *a* and *b* respectively in Scheme 3).

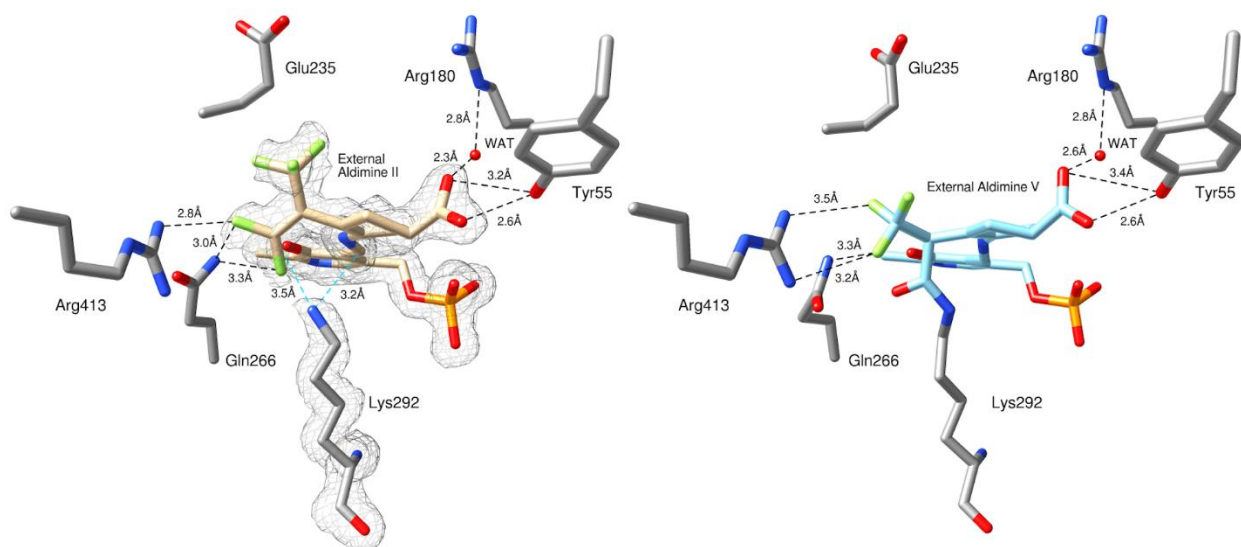


Figure 22. Comparison of the *hOAT* structures of the external aldimine II state and the covalently inhibited complex, external aldimine V. (Left) Crystal structure of external aldimine II (intermediate, PDB code: 7JX9). The proposed attack distances are shown as dashed lines in cyan and potential hydrogen bonding distances are shown as dashed lines in black. A simulated annealing composite map (2Fo-Fc) at 1.1 σ level is shown in gray color for Lys292 and the external aldimine II intermediate. (Right) Crystal structure of external aldimine V (final product, PDB code: 6OIA). A water molecule is labeled as WAT.

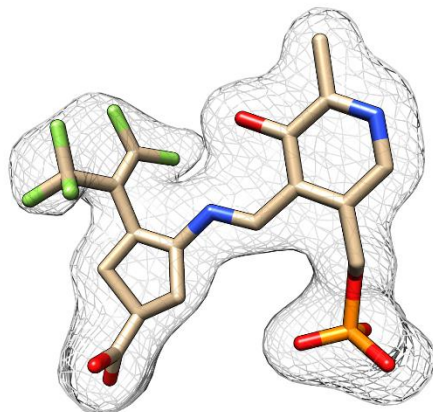


Figure 23. Polder map (F_o-F_c at 3.8σ) generated by omitting the external aldimine II from the structure.

The external aldimine II intermediate interacts with key residues in the *h*OAT active site (Figure 22). The carboxylate group forms apparent hydrogen bonds with Tyr55 whose native function is to bind the α amino group of the ornithine⁷³. The distance between the carboxylate and amino group in BCF₃ is shorter than the distance between the ϵ amino group and the α carboxylate in ornithine. To ensure the formation of external aldimine I, it is required that the carboxylate of BCF₃ be more proximal to PLP than ornithine. As a result, the conserved Arg180, which is proposed to interact with the α carboxylate group of ornithine, interacts instead with BCF₃ indirectly via an ordered water molecule (Figures 22 & 24).

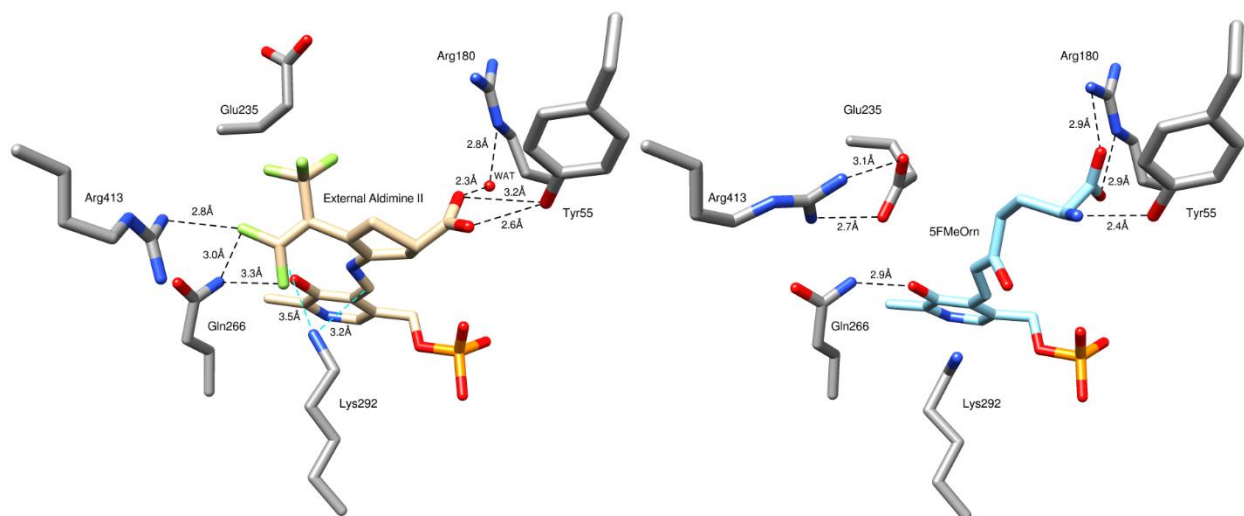


Figure 24. Comparison of the *hOAT* BCF₃ derived external aldimine II to that formed from 5-fluoromethylornithine (5FMeOrn). Interactions are shown as dashed lines in black. Left: Active site of *hOAT* bound with external aldimine II intermediate trapped during BCF₃ inactivation reaction. The distances of the proposed nucleophilic attacks are shown as dashed lines in cyan. Right: Active site of *hOAT* with 5-fluoromethylornithine (5FMeOrn) inactivation product (PDB Code: 2OAT). A water molecule is labeled as WAT.

The difluoromethylenyl group is observed to interact with Arg413 and Gln266. The native function of Gln266 is to interact with PLP via the pyridyl 5'-hydroxyl group. In the native reaction Arg413 is prevented from interacting with the ornithine carboxylate by a salt bridge with Glu235. In the native OAT reaction, this salt bridge can be broken by the dicarboxylic substrates α -ketoglutarate or glutamate (Scheme 1). The trifluoromethyl group of the external aldimine II state is crowded against the aliphatic portion of the Glu235 side chain constraining its conformation away from complementary interaction with the guanidinium of Arg413. In addition to the aliphatic portion of Glu235, two other residues contribute to the binding of external aldimine II via hydrophobic interactions: Phe177 and Tyr85. Collectively, these interactions

define an active site cavity that closely contours about the BCF₃ derived moiety, providing specific molecular recognition (Figure 25).

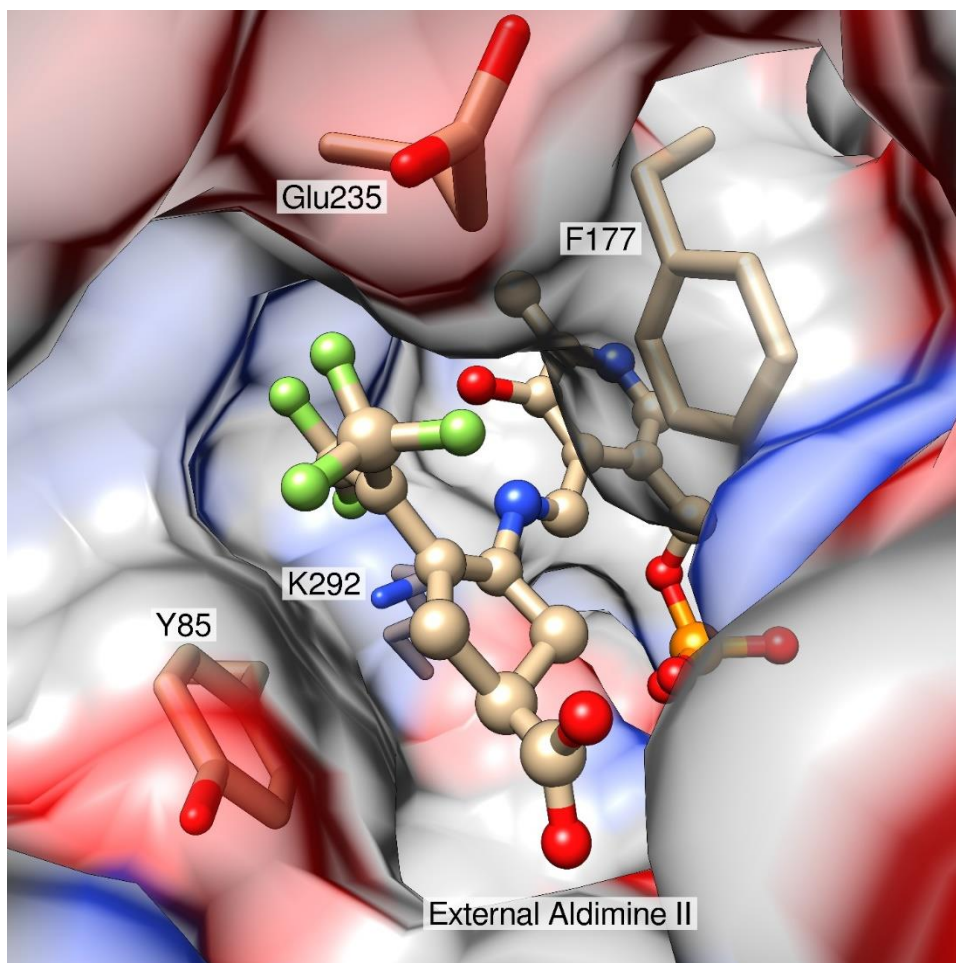


Figure 25. External aldimine II in the active site cavity. Three residues interacting hydrophobically with the ligand are shown as sticks, and the external aldimine ligand is rendered as ball-and-stick. The surface is shown is the active site cavity colored according to the contributing atoms, red for oxygen, blue for nitrogen, and gray for carbon.

The primary difference between the crystal structure of the external aldimine II intermediate, and the final adduct is covalency of the syn-allylic carbon of what was initially the hexafluoropropan-2-ylidene group with Lys292. The structure of this intermediate indicates that the covalent linkage to Lys292 is yet to form. This unliganded lysine and the five remaining

fluorine atoms are the defining features of the density that identifies the external aldimine II state. The loss of one fluorine atom from this structure correlates well with the fluoride ion observed to accumulate within the first scans in single turnover monitored by ^{19}F -NMR spectrometry (Figure 20). Moreover, the free fluoride ion signal was unchanging throughout subsequent data acquisition, indicating that only one fluorine atom is displaced prior to the reformation of the PLP. The difluoromethylene group in external aldimine II was converted to form the amide bond in aldimine V linked to Lys292. The transition to the covalently inhibited state leaves the remaining trifluoromethyl group to interact with Arg413 and Gln236. Glu235 remained oriented away from interaction with Arg413, but less crowded against the trifluoromethyl group of the inactivator.

Discussion

Formulating the mechanism for inhibition of *h*OAT by BCF_3 required the use of complementary time-dependent spectroscopic methods. These approaches provide redundancy to the cumulative observations facilitating definitive assignment of the reaction coordinate intermediates. *h*OAT reacts with BCF_3 to form an initial external aldimine species that accumulates in the deadtime of the stopped-flow instrument. The dependence of the decay of this species to the quinonoid provided a means of characterizing the equilibrium that forms the external aldimine species. These data indicate that the dissociation constant of this species is relatively weak (~ 3 mM), consistent with BCF_3 being a nonnative substrate. Decay of external aldimine I resulted in characteristic spectral transitions associated with a quinonoid species (Figure 17, Scheme 3). The fit of the formation and decay of this species returned rate constants that indicate $\sim 75\%$ accumulation of a quinonoid at the highest concentrations of BCF_3 with an

extinction coefficient for this species at 567 nm of $36,000 \text{ M}^{-1}\text{cm}^{-1}$. These observations yielded a relatively good kinetic description for the steps that led to the formation of the quinonoid and its ensuing decay. It is the decay of quinonoid I that forms the quasi-stable and key intermediate for *hOAT* inhibition, external aldimine II. Prior characterization of the interaction of BCF_3 with *hOAT* identified that only 8% of any turnover reaction resulted in irreversible inactivation of the enzyme (pathway *b* in Scheme 3)⁶⁸. Consequently, BCF_3 is for the majority fraction a substrate for *hOAT*, and only repeated turnovers with fractional partitioning inactivate the entire enzyme population. Previous studies had also suggested that PLP is hydrolyzed from external aldimine V, leaving Lys292 covalently modified by BCF_3 . The basis for this conclusion was the detection of PLP in inactivated *hOAT* solutions by mass spectrometry⁶³. The origin of this PLP is now known to be from the substrate mode of BCF_3 , as the final inhibited state of the enzyme was since shown by X-ray crystallographic characterization to be external aldimine V⁶³.

Different interactions with the active site for the external aldimine II intermediate and the external aldimine V product indicate that the initial binding mode of BCF_3 is significantly different from the orientation of the final product (Figures 22 & 24). In the context of designing a drug with high specificity, knowledge of the initial binding orientation is desirable. The structure reported herein for external aldimine II provides evidence of the initial binding orientation of BCF_3 . It is likely that the carboxylate group of BCF_3 interacts with the hydroxyl group of Tyr55 throughout the inactivation reaction. This is caused by a shorter distance between the carboxylate and the amino group in BCF_3 compared to the α -carboxylate and the ϵ -amino group of ornithine. For the Schiff base formation between BCF_3 and PLP, the carboxylate pivots toward the PLP

cofactor, interacting with Tyr55 instead of Arg180, which has been proposed to interact with the α -carboxylate of ornithine (Figure 24).⁷³

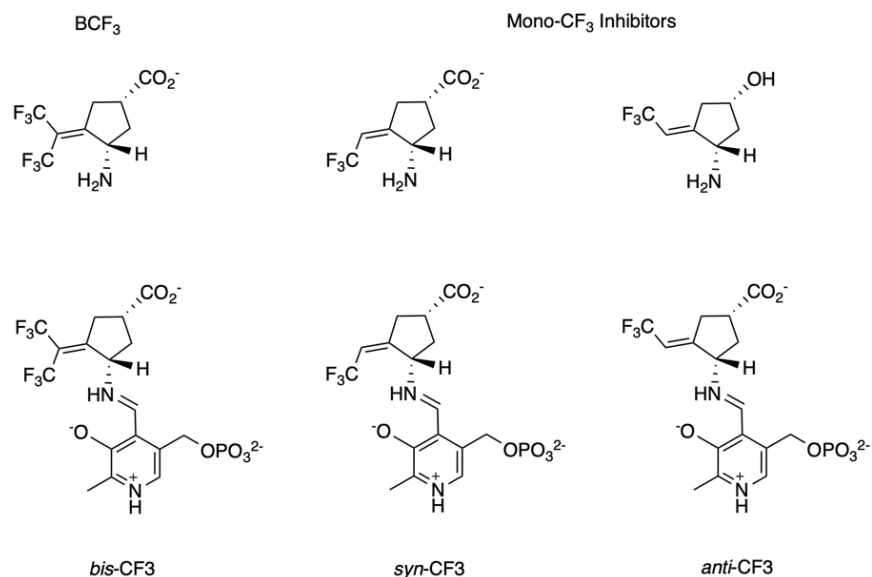


Figure 26. BCF₃ and previously developed mono-trifluoromethyl inhibitors. Top: Structures of the inhibitors. Bottom: Structures of the first intermediates (external aldimines) after initial binding.

In previous studies, two mono-trifluoromethyl derivatives similar to BCF₃ were tested as *hOAT* inhibitors (Figure 26).^{18, 63} The data indicated that the bistrifluoromethyl compound BCF₃ is a better inactivator than either the *syn*- or *anti*-monotrifluoromethyl compounds. Based on the structures reported in this work and previously⁶³ (Figure 22), the role of the bistrifluoromethyl group in improved potency can be attributed to three factors. First, BCF₃ possesses a larger volume that better fills the active site cavity of *hOAT*, confining the chemical possibilities. Second, both trifluoromethyl groups contribute to binding in the initial complex. The *anti*-positioned trifluoromethyl group disrupts a salt bridge between Arg413 and Glu235. Arg413 in turn interacts initially with the *syn*-positioned trifluoromethyl group and the difluoromethylenyl

group in the external aldimine II intermediate. Third, elimination of one fluoro group as fluoride, can yield either the E or Z isomer. The E and Z states of external aldimine II both advance on dominant pathway *a* and yield two products that differ only in their configuration about the exocyclic vinylic bond (Scheme 3). The structure of the covalently inhibited enzyme indicates that only the E-isomer of external aldimine II can advance to form the covalently inhibited complex. The remaining CF₃ group can reassume the role of interacting with Arg413, thereby contributing to the formation of the final adduct external aldimine V. As a direct consequence of these interactions, BCF₃ displays improved specificity against *h*OAT compared to prior drug candidates with similar structures such as gabaculine, canaline, and FCP.^{67, 74-75}

The electronegative nature of fluorine atoms in the BCF₃ trifluoromethyl groups has substantial impact on the orientation during initial binding and during the ensuing chemistry. Due to the electronegativity of the fluorine atom its propensity to form hydrogen bonds is weaker than oxygen or nitrogen atoms. Consequently, in many cases hydrophobic interactions with fluoro groups can have a significant impact on the stabilization of enzyme-substrate complexes compared to fluorine-hydrogen bonding interactions⁷⁶. Vulpetti et al. hypothesized that relatively shielded fluorine atoms tend to form hydrogen bonds when bound to proteins, while relatively deshielded fluorines prefer hydrophobic interactions⁷⁷⁻⁷⁸. Initially, during inactivation of *h*OAT by BCF₃, the fluorine atoms of both trifluoromethyl groups are deshielded by proximity to the other fluorines. The anti-CF₃ group thus interacts with the aliphatic carbons of the Glu235 sidechain via hydrophobic interactions, breaking the salt bridge between this residue and Arg413. As the reaction proceeds, either the anti- or syn-CF₃ group loses one fluorine atom shielding the remaining two fluorines at this site. Therefore, the difluoromethyl group of external

aldimine II preferentially forms hydrogen bonds with Arg413 and Gln266. (Figures 22 & 26).

This interaction may in turn project weak shielding effects over the distant CF₃ group that would preferentially participate in hydrophobic interactions with Glu235. Conversely, in the external aldimine V state, the local chemical environment of the vicinal CF₃ group has changed. The amide linkage to Lys292 is expected to shield this group so that it prefers to form hydrogen bonds with Arg413 and Gln266.

According to the proposed chemical mechanism the irreversible inactivation of *h*OAT proceeds via a series of chemical transformations between aldimine and quinonoid states (Scheme 3). The nucleophilic attack of Lys292 to the difluoromethylene of external aldimine II tethers only the E-configuration of the inhibitor and each subsequent decay of ensuing quinonoid state yields one fluoride ion. This repeating process ultimately denudes all fluorines from one of the two CF₃ groups, solidifying the covalent link to Lys292 and eliminating a path to reinstate an active form of the cofactor. This oscillation terminates with a chemically isolated aldimine, external aldimine V (Figure 18). In contrast, in the dominant substrate pathway (pathway *a*) for BCF₃, Lys292 attacks at the carbon of the PLP imine of external aldimine II, and subsequent hydrolysis results in the regeneration of the active pyridoxal form of the active enzyme. The latter pathway is dominant and does not regenerate BCF₃ so that multiple turnovers are required to bring about complete inactivation. The decay of aldimine II is slow, resulting in nearly complete fractional accumulation of this species in the steady-state, which facilitates capture of this state *in crystallo* (Figures 22 & 23). This structure not only provides direct structural evidence for the proposed inactivation mechanism, but also a foundation for design of molecules that bias the partition of this species toward covalent inhibition. Collapse of the iminium ion of

external aldimine II to form quinonoid II would require the Lys292 ϵ -amino group to be positioned at an angle of $\sim 107^\circ$ from the plane of the π -system of the difluoromethylenyl group⁷⁹. Although the crystal structure does indicate that the position of the ϵ -amino group of Lys292 is proximal (3.3 Å, Figure 24), it is in the same plane as the difluoromethylenyl group, and one of the fluorine atoms partially occludes the electrophilic carbon. While neither pathway is particularly favored by the observed intermediate's position, it is these conformational restrictions that dictate the order of magnitude lower probability for the pathway that inactivates *hOAT* relative to PLP regeneration.

The above analysis serves as a revision of the previously proposed inactivation mechanism of *hOAT* by BCF₃. Within ~ 20 seconds the interaction of BCF₃ with *hOAT* would result in the formation and accumulation of external aldimine II and inhibit the target enzyme effectively by stabilizing this state. Inactivation via aldimine V would require an excess amount of BCF₃ compared to the enzyme so that multiple turnovers bring about the irreversible inactivation⁷. The rate constants determined for the decay of external aldimine II state can be modelled using numerical integration to show that covalent inactivation requires ~ 20 -fold excess of BCF₃ and then only asymptotically approaches complete inactivation over ~ 10 days. By itself, this slow rate of inactivation to aldimine V is unlikely to be effective in suppressing *hOAT* activity *in vivo*, as the high rate of expression in cancer cells is very likely to exceed the rate of covalent inhibition. Therefore, the primary and medically relevant mode of BCF₃ inhibition is trapping the vast majority of *hOAT* as aldimine II, and formation of aldimine V only modestly contributes to the long-term potency of the compound. In regard to iterative rational design, it

may be desirable to create the next generation of drug candidates that bias the conversion from external aldimine II to quinonoid II, thereby altering the partition ratio for irreversible inactivation and thus requiring less inhibitor for complete covalent inactivation. Transient inhibition of *h*OAT using stoichiometric doses of BCF₃ will trap the enzyme as aldimine II and return the majority fraction to an active state within a few days. Therefore, BCF₃ also has the potential to be used as a chemotherapy sensitizer⁸⁰ that transiently halts the activity of *h*OAT to increase the susceptibility of cancer cells to other chemotherapeutic agents.

Conventional methods to characterize mechanism-based inhibition involving combinations of mass spectrometry and ligand cocrystallization are effective to both identify the final adduct and to propose overall mechanisms. However, for amenable systems transient kinetic studies are an effective additional method to reveal further mechanistic details to deduce more complete chemical descriptions of inactivation. The characteristic intermediate spectra observed for *h*OAT reacting with BCF₃ and the slow kinetics under single turnover conditions provide considerably greater detail about the inactivation mechanism, prompting a revision of BCF₃'s potency that is now ascribed to the formation of the external aldimine II species and not the irreversible covalent external aldimine V species as previously described. The accumulation of this quasi-stable intermediate in a short time frame (~20 sec) provides a high steady-state concentration of this species such that crystal soaking could be employed to trap a near homogenous intermediate in the crystal structure during turnover. The crystal structure obtained provides the structural basis for rational design of future inhibitor/inactivator candidates. We confirm that BCF₃ is a prominent drug candidate that relies on its overall structure for specificity but requires an excess to ensure irreversible inactivation. Such a requirement is a result of a non-

ideal attack angle during the conversion from external aldimine II to quinonoid II. However, the slow decay of aldimine II results in essentially all the enzyme being trapped in this state and thus effectively inhibited soon after administration.

Experimental procedures

Materials

All chemicals were purchased from Millipore-Sigma, unless otherwise noted. All enzymes used for cloning were purchased from New England Biolabs.

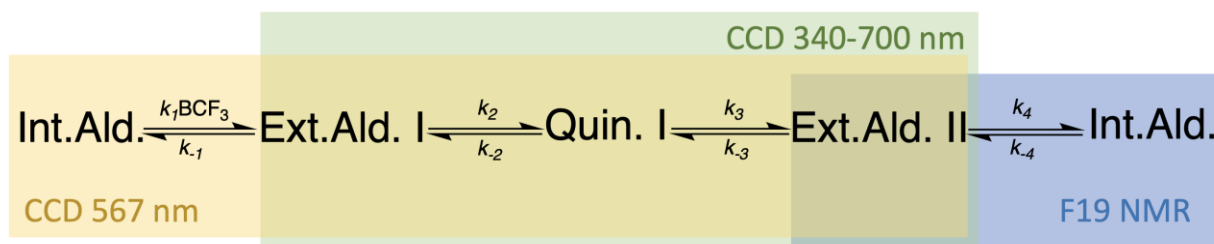
Expression, and Purification of Human OAT

hOAT was expressed and purified according to previously published protocols⁶⁷. Briefly, *E. coli* BL21(DE3) cells containing the pMAL-*t-hOAT* plasmid were incubated at 37 °C with shaking in Lysogeny Broth (LB) medium supplemented with 100 µg/mL ampicillin. When the culture OD₆₀₀ reached a value of 0.7, expression of the MBP-*t-hOAT* fusion protein was induced by addition of 0.3 mM isopropyl β-D-1-thiogalactopyranoside, and incubated for an additional 16–18 h at 25 °C. Cells were harvested by centrifugation, washed with buffer A comprised of 20 mM Tris-HCl, 200 mM NaCl, and 100 µM PLP, pH 7.4, flash-frozen in liquid nitrogen and stored at –80 °C. The frozen cell pellet was then thawed, sonicated in buffer A, and centrifuged at 40,000 x g for 20 min. The resulting supernatant was loaded onto an amylose affinity column pre-equilibrated with buffer A. The column was washed thoroughly, and the MBP-*t-hOAT* fusion protein was eluted from the column with 10 mM maltose. Fractions containing the fusion protein were combined and treated with TEV protease to remove the MBP tag. The cleaved *hOAT* protein was collected and concentrated using a centrifugal filter. The protein was then further purified by size exclusion chromatography using a HiLoad Superdex-200PG column. The

column was pre-equilibrated, and the protein eluted in buffer containing 50 mM HEPES, 100 μ M PLP and 300 mM NaCl, pH 7.5.

Transient State Methods

The reaction of BCF_3 with *h*OAT was observed in transient state using three approaches. These methods captured signals for both relatively fast and slow chemical transformations. The first three steps in the reaction were captured using a Hitech Scientific (TgK) stopped-flow spectrophotometer in combination with charged coupled device detection (260-800 nm). In these experiments 9.84 μ M *h*OAT was allowed to react with 2-fold serially diluted BCF_3 concentrations (63, 127, 254, 508, 1,016, 2,035, 4,065 μ M) in 50 mM HEPES, 200 mM NaCl, pH 7.5 at 10 $^\circ\text{C}$ (all reported concentrations are after mixing in a 1:1 ratio).



Scheme 4. Four-step model for the intermediates observed via CCD 340-700 nm and ^{19}F -NMR spectrometry. The first three reaction steps were observed for a range of BCF_3 concentrations and analyzed globally by numerical integration (beige box) at a single wavelength (567 nm). The rate constants associated with the second and third steps were derived from CCD data using singular value decomposition (SVD) (green box). The data for the last step were acquired with ^{19}F -NMR spectrometry and analyzed using SVD (blue box).

Individual reaction traces at 567 nm for each BCF_3 concentration were extracted from the multiwavelength datasets and combined into a single file. These data were fit globally to the beige portion of the model depicted in Scheme 4 using KinTek Explorer software (KinTek Corp). The CCD spectral datasets for singular value decomposition (SVD) deconvolution were

collected at a concentration of BCF_3 equal to 2.08, 4.16 and 8.32 mM. Duplicate shots were acquired using a log time base for two timeframes (0.0025 – 12.4 seconds and 0.0025 – 2,480 seconds). Duplicate datasets for any one timeframe were averaged and spliced together at 12 seconds to form one dataset with sufficient time resolution to accurately describe fast and slow processes. The hybrid dataset was fit globally to the green portion of the model depicted in Scheme 4 using the Spectrafit SVD module of KinTek Explorer software. In this model the rate constant for k_4 was fixed to the value measured using transient state NMR.

^{19}F -NMR spectral observation of the reaction was used both to measure the slowest step observed and to verify the chemistry through spectral assignment of the species that decay and accumulate. A single turnover condition was established by mixing *hOAT* (333 μM) with BCF_3 (247 μM), and ^{19}F -NMR spectra (16 scans per spectrum) were acquired at 1 min intervals for 8 hours (for acquisition parameters, see Supporting Information). The time of the first spectrum equated to ~300 seconds after the reaction commenced and so captures data for the external aldimine II species onward. Spectra were culled to approximate a logarithmic time base and to eliminate intervening portions of the ppm axis that contained no data. The time dependence of these NMR spectra were fit globally to a one-step model that is depicted as the blue portion of Scheme 4.

Crystallization and Crystal soaking of hOAT with BCF_3

Purified *hOAT* was buffer exchanged into 50 mM HEPES, pH 7.5 and concentrated to a protein concentration of 6 mg/mL. The previously reported crystallization conditions⁶⁷ were further optimized using the hanging drop vapor diffusion method by varying PEG 6000 (8-12%), NaCl (100-250 mM), and glycerol (0-10%) with a fixed buffer concentration of 100 mM Tricine,

pH 7.8. For each hanging drop, either 2 or 3 μL of protein solution was mixed with equal volume of well solution. Several rounds of seeding were applied to improve crystal size and quality. The crystals with the best morphology and size grew in a final condition containing 10% PEG 6000, 100 mM NaCl, and 10% glycerol. BCF_3 (0.5 μL , 1 mM final) was added to the *hOAT* crystal drop and allowed to soak for 40 min. After soaking, crystals were transferred to a cryo-protectant solution (well solution supplemented with 30% glycerol and 1 mM BCF_3) and frozen in liquid nitrogen.

X-ray Diffraction and Data Processing

Monochromatic X-ray diffraction data were collected at the LS-CAT beamline 21-ID-D at the Advanced Photon Source at Argonne National Laboratory. Data were collected at a wavelength of 1.127 Å and a temperature of 100 K using a Dectris Eiger 9M detector. Data sets were processed and analyzed with autoPROC software⁵¹.

Model Building and Refinement

The *hOAT* structure was solved by molecular replacement using PHASER⁵³ in Phenix. The starting search model was the previously published structure of *hOAT* (PDB code: 1OAT⁸¹). The model building and refinement were accomplished in Coot⁵⁵ and Phenix⁵⁴, respectively, as an iterative process until the lowest possible R_{free}/R factor values were attained. Structural depiction figures were prepared using UCSF Chimera⁵⁶.

Table 3. Statistics table for *h*OAT-external aldimine II crystal structure.

PDB code	7JX9
Space group	P3 ₂ 21
Cell dimension	
α, β, γ (deg)	90,90,120
a, b, c (Å)	115.304, 115.304, 185.431
Processed Resolution (Å)	1.96
Resolution at $I/\sigma(I) = 2$ (Å) ^a	2.07
Rmerge ^b (%)	18.6 (185.0) ^c
Rpim ^d (%)	6.2 (68.6)
$I/\sigma(I)$	11.5 (1.2)
CC 1/2 ^e (%)	99.8 (38.1)
Completeness (%)	96.6 (99.6)
Multiplicity	10.0 (7.9)
No. Reflections	102153
No. Unique Reflections	9746
Refinement	
Rwork ^f /Rfree ^g (%)	16.0/18.0
No. of Atoms	
protein	9449
ligand	96
water	649
B factors (Å ²)	
protein	39.58
RMSD ^h	
bond lengths (Å)	0.008
bond angles (deg)	0.92
Ramachandran plot (%)	
favored	95.33
allowed	4.00
outliers	0.67
^a Provided Resolution at $I/\sigma = 2$ for conventional assessment of data quality ^b $R_{\text{merge}} = \sum I_{\text{obs}} - I_{\text{avg}} / \sum I_{\text{avg}}$ ^c The values for the highest-resolution bin are in parentheses ^d Precision-indicating merging R ^e Pearson correlation coefficient of two "half" data sets ^f $R_{\text{work}} = \sum F_{\text{obs}} - F_{\text{calc}} / \sum F_{\text{obs}}$ ^g Five percent of the reflection data were selected at random as a test set, and only these data were used to calculate R_{free} ^h Root-mean square deviation	

CHAPTER THREE

TURNOVER AND INACTIVATION MECHANISMS FOR (S)-3-AMINO-4,4-DIFLUOROCYCLOPENT-1-ENECARBOXYLIC ACID, A SELECTIVE MECHANISM-BASED INACTIVATOR OF *h*OAT

Summary

In the last years, the inhibition of human ornithine-aminotransferase has been proposed as a novel way of potential treatment of hepatocellular carcinoma. Several mechanism-based inactivators of *h*OAT have been designed and their mechanisms have been studied. Recently, a new potent *h*OAT mechanism-based inactivator, (S)-3-amino-4,4-difluorocyclopent-1-enecarboxylic acid (SS-1-148, 148) was designed. In addition to its potency, 148 showed remarkable selectivity over other related aminotransferases (e.g., GABA-AT, Asp-AT, Ala-AT). A complex mechanistic study was performed in attempt to investigate the turnover and inactivation mechanisms of 148. As a primary metabolite of 148 in *h*OAT, a monofluorinated ketone (M10) was identified. Gem-diamine intermediate preceding to M10 species has been successfully trapped in *h*OAT holoenzyme crystals soaked with 148. The achieved structure of gem-diamine was the first experimental proof of the existence of this intermediate in *h*OAT. Additional cocrystallization experiments of *h*OAT with 148 helped to reveal a novel noncovalent inactivation mechanism in *h*OAT. The transient-kinetic experiments provided a rationale both for the turnover and inactivation mechanisms and further facilitated the results obtained from other techniques. Overall, the combination of X-ray crystallography employing both soaking and

cocrystallization methods and stopped-flow kinetics provided a lot of details and elucidated the unusual turnover and inactivation pathway for 148.

Introduction

The major challenge in the design of a selective MBI of *hOAT* is possible side reactions of the inhibitor with other aminotransferases, especially γ -aminobutyric acid aminotransferase (GABA-AT), which is involved in central metabolism and has a high structural similarity with *hOAT*. Both OAT and GABA-AT belong to fold-type I structural group of PLP-dependent enzymes, both proteins possess high similarity in the active site residues. In the active site pocket of *hOAT*, two major differences have been reported: Tyr85 and Tyr55 in *hOAT* are substituted by Ile72 and Phe351* (asterisk denotes arising from the adjacent subunit) in GABA-AT, respectively. This substitution results in a narrower and more hydrophobic active site of GABA-AT when compared to *hOAT*. In *hOAT*, the hydroxyl group of Tyr55 is involved in the initial binding of the substrate via formation of a hydrogen bond with its α -amino group. Tyr85, in turn, plays an important role in substrate specificity and conformational flexibility to adopt bulky substrates.⁶² Due to the high similarity between these two aminotransferases, a preliminary screening against *hOAT* was carried out previously using the stock of GABA-AT inhibitors.¹⁸ A cyclopentane-based analogue, termed BCF₃, bearing a bis(trifluoromethyl) group as its warhead, was identified to be a selective MBI of *hOAT* while only showing millimolar reversible inhibition of GABA-AT. Mechanistic studies on BCF₃ from previous chapter have shown that one of its trifluoromethyl groups undergoes fluoride ion elimination, leading to the covalent modification of the catalytic Lys292. It is considered that the sterically bulky bis(trifluoromethyl) group may not enter the narrower active site pocket of GABA-AT as readily,

influencing the initial binding pose between the ligand and the enzyme, which may be responsible for its reversible inhibition of this enzyme. 5-fluoromethylornithine (5-FMeOrn) serves as an additional example of selective *hOAT* inactivator. The structure of 5-FMeOrn was inspired by the structure of the native substrate of *hOAT*, L-Orn, and it's also related to the structure of nonselective GABA-AT inactivator (S)-4-amino-5-fluoropentanoic acid (AFPA).⁷³ As was previously shown, this ligand inactivates *hOAT* via an enamine pathway by forming a ternary adduct.⁸²

Recently a new cyclopentene-based analogue, 148, was designed as a novel *hOAT* mechanism-based inactivator and its turnover and inactivation mechanisms were investigated. The new inactivator incorporated an additional double bond into the cyclopentane ring system and demonstrated itself as a potent and selective *hOAT* inactivator. The more detailed study on 148 was published recently²². In it, the performed mechanistic studies include the results obtained with protein crystallography, multiple modes of mass spectrometry, transient-state spectrophotometric measurements, and computational simulations. This dissertation, however, solely focuses on X-ray crystallography and stopped-flow results.

Results

Crystal structures of hOAT resulting from soaking and cocrystallization

Based on the mass-spec experiments on 148 it was proposed that as in case of BCF₃, 148 reaction mechanism consists of two possible pathways: inactivation and turnover.²² In an attempt to capture the primary intermediate of the non-inactivation pathway, *hOAT* holoenzyme crystals were utilized to perform one-hour soaking experiments with 148. The *hOAT* structure was solved by molecular replacement from a previously reported structure (PDB entry: 1OAT). The

space group for the 148 soaking structure was found to be P3₂21, and the structure contains three copies of the protein monomer in one asymmetric unit. The crystal structure (PDB entry 7LK1) shown in Figure 27A indicates that PLP is covalently linked to 148, and a covalent bond between Lys292 and 148 tethering the compound to the enzyme. The covalent bond between Lys292 and 148 represents a stable *gem*-diamine species that has not been observed in any previous *hOAT*/inactivator crystals.^{63, 67, 69, 83} Moreover, two alternate conformations of this intermediate were observed which differ in the position of the carboxylate group derived from 148. The first conformation forms a hydrogen bond between Tyr55 and the carboxylate of 148, while the second forms a salt bridge with Arg413. The interpretation that there are two alternate conformations for the intermediate structure was based on the positive density in proximity to Arg413 and Tyr55 as well as the relatively high B-factors for any single conformation. An alternative explanation could include two different, yet structurally similar, intermediate species that could interact with the protein active site in different ways.

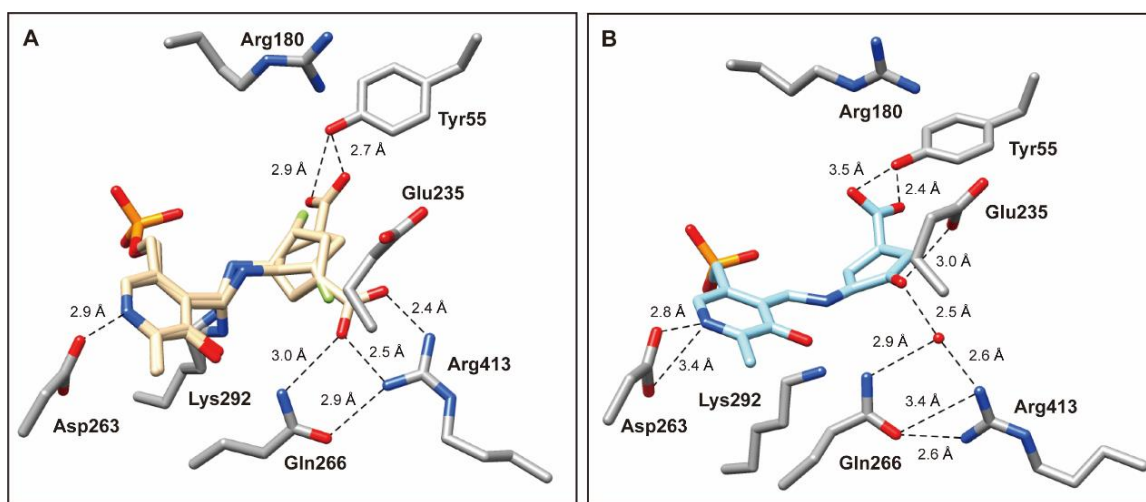


Figure 27. Crystal structures of *hOAT* resulting from soaking experiment (A; PDB entry 7LK1) and cocrystallization (B; PDB entry 7LK0) with compound 148. 148 soaking structure is shown in two alternate conformations: one in which the carboxylate group interacts with Tyr55 (conformation A) and the other in which carboxylate forms a salt bridge with Arg413 (conformation B). For this specific chain, the refined occupancies of conformers are 0.51 (conformation A) and 0.49 (conformation B). *hOAT* residues and 148 are in stick representation with carbon atoms colored gray and blue/off-white, respectively, the water molecule is shown as a red sphere. Hydrogen bonding distances between atoms in angstroms (\AA) are shown as black dashed lines.

Transient-State Measurements of hOAT Inhibited by 148

As a variety of transient states are involved in the proposed mechanisms, rapid-mixing spectrophotometric measurements were performed in an attempt to capture the kinetics of the inhibition of *hOAT* by 148. This approach takes advantage of the conjugated species that accumulate sequentially in PLP-dependent transaminase reactions.⁸³ The inhibition reaction that occurs with 148 was interpreted in combination with crystal structures (abovementioned) acquired for different stages of the reaction progression. The experimental data shown in Figures 29 and 30 indicate that the reaction of 148 with *hOAT* is complex. Four discernable phases were observed with evidence of at least two parallel reaction paths (Figure 28), indicating that the

mechanistic conclusions drawn are necessarily from undetermined models. Within the deadtime of the stopped-flow instrument, the reaction of 148 with *h*OAT formed a spectrum signal (~420 nm) consistent with an external aldimine (red spectrum, Figure 29 A-B). Titration of *h*OAT with 148 modulated the rate and the extent of accumulation of a second external aldimine that is presumably additive with the aldimine formed in the deadtime (green spectrum, Figure 29 A-B). The second external aldimine forms with a rate dependence that indicates a bimolecular reaction ($6.2 \times 10^3 \text{ M}^{-1}\text{s}^{-1}$) and suggest that 148 interacts with *h*OAT in the least two ways, resulting in parallel reaction paths (Figure 28 A-B). The intensity of the combined external aldimine spectra decays partially with the accumulation of a spectral transition characteristic for a quinonoid species (~560 nm) at 0.4 s^{-1} (Figure 28 A-B and 30 A-B). The apparent quinonoid species is formed with concomitant and partial decay of the external aldimine transitions that are approximately equal in amplitude to that gained with the second external aldimine accumulation. This suggests that these species reside on the same reaction pathway.

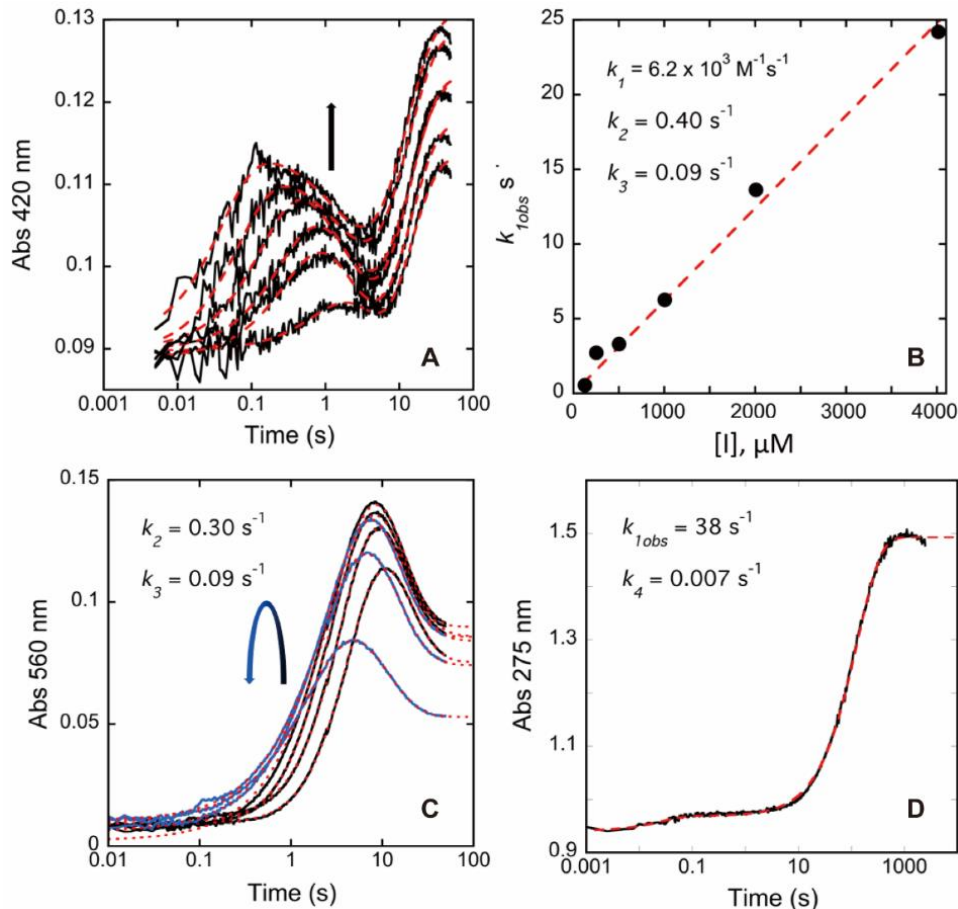
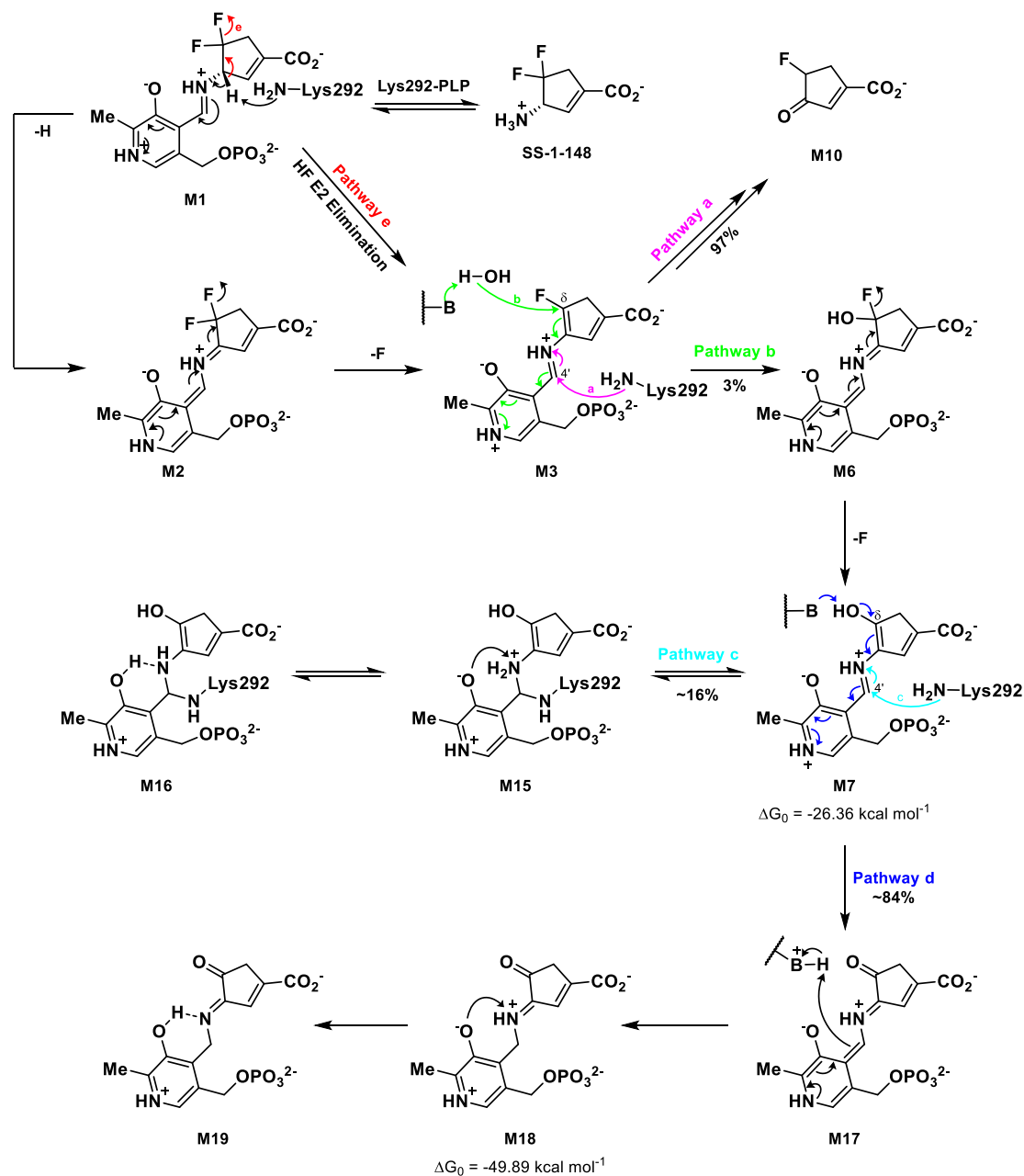


Figure 28. Transient state absorption changes observed at 275, 420, and 560 nm for *h*OAT reacting with 148. OAT (12.7 μM final) was mixed with 148 (126, 251, 502, 1004, 2008, 4016 μM), and CCD spectra were collected for the timeframe 0.009–49.2 seconds. (A) The data observed at 420 nm fit to a linear combination of three exponential terms according to equation 7 described in the materials and methods section. The arrow indicates the trend observed in amplitude for increasing inhibitor concentration. (B) The observed rate constant dependence of the first phase observed at 420 nm fit to equation 9 described in the materials and methods section. The values for k_2 and k_3 indicated are the average values obtained from the fit in Figure 29 A. The fit is shown in red dashes. (C) The data observed at 560 nm. The curved arrow indicates the trend observed in amplitude for increasing inhibitor concentration. These data were fit to a linear combination of two (1004, 2008, and 4016 μM , blue traces) or three (126, 251, and 502 μM , black traces) exponential terms according to equation 8 described in the materials and methods section. The fit is shown in red dashes. (D) The data observed at 275 nm over 2000 sec obtained in the presence of 8032 μM 148 fit to a linear combination of two exponential terms according to equation 8 in the materials and methods section. The fit is shown in red dashes.

It has been reported that the deprotonation of the initial external aldimine M1 and stepwise fluoride elimination steps proposed in Scheme 5 are typically considered as an E1CB

elimination mechanism.⁸⁴⁻⁸⁵ The electron-withdrawing effect of fluorine and the protonated nitrogen of the aldimine may stabilize the formed carbanion state during the elimination reaction.⁸⁵⁻⁸⁶ Meanwhile, quinonoid transient state M2 is supposed to form between the first and second external aldimines (M1 and M3). However, the stopped-flow experimental results suggest that antiperiplanar hydrogen and fluorine in M1 undergoes an unusual Lys292-assisted E2 mechanism⁸⁴ with simultaneous loss of a proton, the release of fluoride ion, and formation of alkene as a more favorable fluoride elimination pathway, affording the second external aldimine M3 as the single transient state species (Pathway e; Scheme 5). This result has never been observed experimentally in previous mechanistic studies of other related PLP-dependent aminotransferase inactivators.^{62, 87}

Assuming a quinonoid extinction coefficient of $\sim 30 \text{ mM}^{-1} \text{ cm}^{-1}$,²¹ the fractional accumulation of the quinonoid observed is $\sim 20\%$ of total reacting species at 1 mM 148. The quinonoid then decays at a rate of 0.09 s^{-1} , while the residual transitions assigned to the external aldimine species broaden and persist (orange spectrum, Figure 29 A-B). Quinonoid M6 seems to be a rare case of quinonoid species ($\sim 560 \text{ nm}$) that can be observed based on the turnover (Pathway a; Scheme 5) and inactivation (Pathway b; Scheme 5) mechanisms. The final phase observed occurs with a rate constant of 0.007 s^{-1} . And in this phase, the features of the external aldimine decay with a pronounced increase in absorption intensity at $\sim 275 \text{ nm}$, indicative of a loss of conjugation (blue spectrum, Figure 29 A-B), consistent with *gem*-diamine M16 and ketimine M19 proposed as the final products in Scheme 5.



Scheme 5. Plausible Inactivation Mechanisms of 148 with *h*OAT.

Collectively, these data support a dominant pathway comprised of multiple distinct external aldimine species that ultimately decay to a less conjugated product (turnover mechanism; Pathways a and e; Scheme 5) and a second minor pathway that forms an initial

external aldimine more slowly but then proceeds through a quinonoid intermediate and decays to also form a non-conjugated product (inactivation mechanism; Pathways b-e; Scheme 5). The data shown in Figure 29 C indicate that the proportion of each pathway is dependent on the concentration of 148. Higher concentrations of 148 diminish the accumulation of the quinonoid species but do not alter the observed rates of accumulation and decay, suggesting that the more rapid and dominant pathway sequesters a larger fraction of enzyme at higher 148 concentrations.

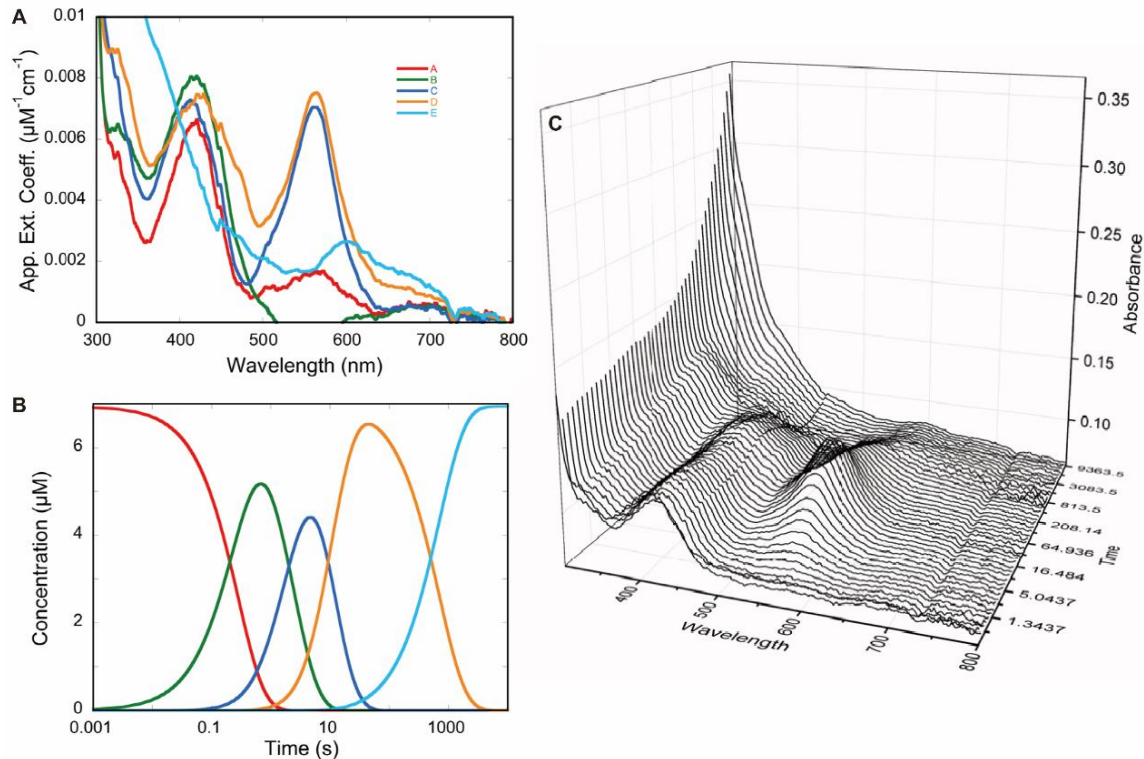


Figure 29. Partial deconvolution by singular value decomposition (SVD) of transient state absorption changes observed for *h*OAT reacting with 148. *h*OAT (6.94 μM ; final concentration) was reacted in a stopped-flow spectrophotometer with 148 (1040 μM ; final concentration) at 10 $^{\circ}\text{C}$. To obtain time resolution sufficient to analyze kinetic rates spanning four orders of magnitude, a composite CCD absorbance dataset was prepared spanning 250-800 nm and 0.0137-9843 sec by splicing together averaged short and long time-frame datasets. These data were fit to a linear irreversible four-step model in which the rate constants were constrained to those determined from single-wavelength analyses (Figure 28). Deconvoluted composite spectra derived from SVD analysis (A). The species concentration profile based on the rate constants used to fit the dataset (B). A three-dimensional depiction of a subset of spectra from the dataset analyzed (C).

Discussion

Proposed inactivation pathways for 148 with *h*OAT are summarized in Scheme 5. The initial external aldimine M1 undergoes deprotonation, catalyzed by Lys292, and forms the first quinonoid (M2). The elimination of a single fluoride ion follows to yield monofluoro aldimine M3 from M2. The C4' position of the majority of M3 (~97%; determined by its partition ratio) is

attacked by Lys292, which releases an enamine metabolite that hydrolyzes to ketone M10 as the primary metabolite (Pathway a; Scheme 5). The C₈ position of a small portion of M3 (~3%) goes through a water-mediated nucleophilic attack (Pathway b; Scheme 5), generating the second quinonoid (M6). Intermediate M6 undergoes another fluoride ion elimination to form M7. Subsequently, a small fraction of M7 (~16%) may covalently bond to Lys292 at its C4' position via a gem-diamine form (M15) (Pathway c; Scheme 5), which is in equilibrium with M7 and also facilitates further proton transfer to generate the neutral gem-diamine (M16), which should be a more stable form. However, the majority of M7 (~84%) tautomerizes to a more favorable ketimine (M18, the most stable tautomeric form), which is followed by proton transfer to afford ketimine M19 as the primary final product (Pathway d; Scheme 5).

In the current work, it was demonstrated that (S)-3-amino-4,4-difluorocyclopent-1-enecarboxylic acid (SS-1-148, 148) can exhibit comparable inactivation efficiency to that of preclinical stage selective *hOAT* inactivator BCF₃. The kinetic studies provided an experimental evidence to support the hypothesis that the conjugated alkene of 148 in its cyclopentene ring is essential for retaining high *hOAT* inactivation efficiency. A soaking experiment was performed to obtain a quasi-stable gem-diamine intermediate covalently bound to Lys292 in the soaked crystal, an intermediate that has never been captured in other studies of related aminotransferase inactivators. The Cocrystallization of *hOAT* and 148 captured a stable noncovalent final product in the *hOAT* cocrystal complex. The critical salt bridge of Arg413-Glu235 in *hOAT* was found to be broken in both crystal complexes. Using rapid-mixing experiments, we observed, for the first time, that the first external aldimine of 148 undergoes a lysine-assisted E2 fluoride ion elimination instead of the typical E1cB elimination mechanism, forming the second external

aldimine as the single transient state. Overall, we have carried out comprehensive mechanistic studies to demonstrate that 148 mainly inactivates *hOAT* through a noncovalent water-mediated mechanism. However, it is still unclear why there are distinct inactivation mechanisms for cyclopentene 148 and the corresponding cyclohexene.

Experimental procedures

hOAT crystal soaking

The holoenzyme crystals were first grown via a hanging drop vapor diffusion method. Each drop contained 2 μL of protein and 2 μL of well solution. The best crystallization condition contained 10% PEG 6000, 200 mM NaCl, 10% glycerol, and 100 mM Tricine pH 7.8. Once the holoenzyme crystals reached their maximum size, 2 μL of 16 mM 148 was added to the drop with crystals. Within the first five minutes of 148 addition, the *hOAT* crystals turned their color from yellow to blue. The crystals were soaked for one hour, transferred into cryoprotective solution (well solution supplemented with 30% glycerol), and then flash-frozen in liquid nitrogen.

hOAT cocrystallization

After purification, *hOAT* was buffer exchanged into crystallization buffer (50 mM Tricine pH 7.8) supplied with 1 mM α -ketoglutarate. Then the protein was concentrated to 6 mg/mL. Previously reported crystallization condition⁶³ was optimized using the hanging drop vapor diffusion method by varying PEG 6000 (8-12%), NaCl (100-250 mM), glycerol (0%-10%) with 100 mM Tricine pH 7.8 kept constant as the buffer. For each hanging drop, 2 μL of protein solution was mixed with an equal volume of well solution and 0.5 μL of 10 mM 148. The crystals with the best morphology and size grew in a final condition containing 10% PEG 6000,

200 mM NaCl, 10% glycerol, and 100 mM Tricine pH 7.8. Crystals were transferred to a cryo-protectant solution (well solution supplemented with 30% glycerol) and later flash-frozen in liquid nitrogen.

X-ray diffraction and data processing

Monochromatic X-ray diffraction data were collected at the LS-CAT beamline 21-ID-D at the Advanced Photon Source at Argonne National Laboratory. Data were collected at a wavelength of 1.127 Å and a temperature of 100 K using a Dectris Eiger 9M detector. Data sets were processed and analyzed with Xia2 software.⁸⁸

Model building and refinement

The *h*OAT structure was solved by molecular replacement using PHASER⁵³ in Phenix. The starting search model was the previously published structure of *h*OAT (PDB code: 1OAT). The model building and refinement were accomplished in Coot⁵⁵ and Phenix⁵⁴, respectively, as an iterative process until the lowest possible R_{free}/R factor values were attained. Structural depiction figures were prepared using UCSF Chimera.⁵⁶

Transient State Methods

The reaction of 148 with *h*OAT was observed in a transient state using a Hitech Scientific (TgK) stopped-flow spectrophotometer in combination with charged coupled device detection (Ocean Optics, 260-800 nm). *h*OAT (12.68 μM) was reacted with varied concentrations (125, 251, 502, 1004, 2008, 4016, 8032 μM) of 148 in the buffer (pH 7.5) containing 50 mM HEPES and 200 mM NaCl at 10°C. For each concentration of the inhibitor, CCD spectral datasets were collected in duplicate for 50 sec, and the duplicates were averaged. For the highest concentration of inhibitor (8 mM) duplicate CCD datasets were acquired for two timeframes (0.0025 – 12.4 sec

and 0.0025 – 2480 sec). Duplicate datasets for anyone timeframe were averaged and then spliced together at 12 sec to form one dataset with sufficient time resolution to adequately describe rapid and slow processes. The hybrid dataset was deconvoluted based on a linear four-species model using the Spectrafit singular value decomposition module of KinTek Explorer software. In the process, the rate constants were fixed to the values measured using analytical fits to data extracted for single wavelengths that assume successive first-order processes according to the equations 7, 8, and 9. *Abs* is absorbance, A_x are the amplitudes associated with each observed phase, k_x are the corresponding rate constants, and *C* is the absorbance endpoint.

Equation 7:
$$Abs = A_1(e^{-k_{1obs}t}) + A_2(e^{-k_2t}) + A_3(e^{-k_3t}) + C$$

Equation 8:
$$Abs = A_1(e^{-k_1t}) + A_2(e^{-k_2t}) + C$$

Equation 9:
$$k_{1obs} = k_1[I]$$

Table 4. Statistics of the crystal structures of *h*OAT inactivated by 148.

Complex	<i>h</i> OAT-148 cocrystal	<i>h</i> OAT-148 soaking
PDB code	7LK0	7LK1
Space group	P 3 ₁ 1 2	P 3 ₂ 2 1
Unit Cell dimension		
α, β, γ (deg)	90, 90, 120	90, 90, 120
a, b, c (Å)	192.7, 192.7, 56.8	115.6, 115.6, 186.6
Processed Resolution (Å)	1.96	1.79
Rmerge ^a (%)	16.9 (81.7)	8.4 (248.7)
Rpim ^c (%)	8.3 (60.4)	2.8 (83.3)
I/σ (I)	5.6 (1.1)	13.7 (0.9)
CC ½ d (%)	99.7 (78.3)	99.9 (34.4)
Completeness (%)	91.6 (72.1)	100.0 (100.0)
Multiplicity	8.7 (4.1)	9.6 (9.8)
No. Reflections	685516	1311708
No. Unique Reflections	79187	136181
Refinement		
Rwork ^e /Rfree ^f (%)	24.54/26.60	21.60/24.80
No. of Atoms		
protein	9462	9444
ligand	75	170
water	582	766
Average B factors (Å ²)		
protein	37.17	44.34
RMSD ^g		
bond lengths (Å)	0.004	0.005
bond angles (deg)	0.69	0.84
Ramachandran plot (%)		
favored	94.75	94.90
allowed	5.16	4.93
outliers	0.08	0.17
^a R _{merge} = $\sum I_{\text{obs}} - I_{\text{avg}} / \sum I_{\text{avg}}$, ^b The values for the highest-resolution bin are in parentheses, ^c Precision-indicating merging R, ^d Pearson correlation coefficient of two "half" data sets, ^e R _{work} = $\sum F_{\text{obs}} - F_{\text{calc}} / \sum F_{\text{obs}}$, ^f Five percent of the reflection data were selected at random as a test set, and only these data were used to calculate R _{free} , ^g Root-mean square deviation.		

CHAPTER FOUR

RATIONAL DESIGN, SYNTHESIS, AND MECHANISM OF (3*S*,4*R*)-3-AMINO-4-(DIFLUOROMETHYL) CYCLOPENT-1-ENE-1-CARBOXYLIC ACID EMPLOYING A SECOND DEPROTONATION STRATEGY FOR SELECTIVITY OF *h*OAT OVER GABA-AT

Summary

Human ornithine aminotransferase is a PLP-dependent enzyme that shares the same fold type and similar active site residues with γ -aminobutyric acid aminotransferase (GABA-AT). Recently, *h*OAT was recognized as a potential drug target for treatment of hepatocellular carcinoma. In the current work, the inactivation of *h*OAT by two established GABA-AT inactivators (CPP-115 and OV329) has been studied. Based on the observed inactivation mechanistic difference between *h*OAT and GABA-AT, a series of new analogs was designed and synthesized. This led to the discovery of analog 136 (10b) which showed itself as a highly potent and selective *h*OAT inhibitor. In the mechanistic study on 136, a combination of various techniques was employed including intact protein mass spectrometry, protein crystallography, dialysis experiments, fluoride ion release, and transient-state kinetics experiments. Notably, the stopped-flow experiments were highly consistent with the proposed mechanism, suggesting a relatively slow hydrolysis rate for *h*OAT when compared to GABA-AT. Based on the results obtained in this study, it was concluded that the novel second-deprotonation mechanism of 10b

contributes to its high potency and significantly enhances selectivity over other aminotransferases. The manuscript with results of this work was submitted for publication and recently accepted to Journal of the American Chemical Society (Zhu W*.; Butrin A.*; et al. Rational Design, Synthesis, and Mechanism of (3*S*,4*R*)-3-Amino-4-(difluoromethyl)cyclopent-1-ene-1-carboxylic Acid Employing a Second Deprotonation Strategy for Selectivity of *h*OAT over GABA-AT. 2022). In this dissertation, only transient-state kinetics and protein crystallography results are shown and discussed.

Introduction

Hepatocellular carcinoma is a primary type of liver cancer and is the leading cause of death among people with cirrhosis worldwide.¹¹⁻¹³ HCC is highly prone to malignancy and is typically discovered at the later disease stages when systemic treatment with the standard-of-care receptor tyrosine kinase inhibitor, sorafenib, and radiotherapy are inefficient¹⁴⁻¹⁷. It was found that *h*OAT and glutaminogenic enzymes are commonly overexpressed or activated in HCC due to oncogenic Wnt/ β -catenin signaling.⁸⁻⁹ Thus, *h*OAT was identified as a potential drug target against HCC, since it has a capacity to regulate proline metabolic pathways.¹⁹ Metabolic reprogramming in HCC is characterized by the accumulation of hydroxyproline and accelerated consumption of proline, which induces a hypoxia-inducible factor-1 α (HIF1 α) transcriptional program and sorafenib resistance.⁹⁴

Ornithine aminotransferase is a PLP-dependent enzyme that uses “Bi-Bi, Ping-Pong” mechanism to catalyze two coupled transamination reactions (Figure 30). In the first half-reaction, OAT catalyzes the conversion of PLP cofactor and *L*-ornithine substrate to pyridoxamine phosphate and *L*-glutamate-5-semialdehyde (*L*-GSA). *L*-GSA is then further

cyclized to Δ^1 -pyrroline-5-carboxylate (P5C) and can be further converted to *L*-proline by pyrroline-5-carboxylate reductase (PYCR).⁸⁹ In its second half-reaction, OAT catalyzes conversion of α -ketoglutarate to *L*-glutamate, regenerating PLP from PMP. It has been shown recently that the proline metabolism is crucial for metabolic reprogramming, since it helps to sustain cancer cell proliferation by the upregulated synthesis of P5C as a central intermediate.⁹⁰⁻⁹² In addition, the *L*-glutamate generated by *h*OAT in its second half-reaction can be further converted to *L*-glutamine by glutamine synthetase (GS) to support *de novo* nucleotide biosynthesis and anabolic cell programs.⁹³

The studies have shown that inhibition of *h*OAT exhibited potent *in vivo* antitumor activity in the HCC mouse model, along with dramatically reduced alpha-fetoprotein (AFP, a biomarker for HCC) levels.¹⁸ In another study done by Liu, Y. et al., the knockdown of *h*OAT in non-small cell lung cancer (NSCLC) suppressed *in vitro* cell proliferation and *in vivo* tumor growth.⁹⁵ Therefore, *h*OAT appears to be a promising therapeutic target for HCC and other related cancers.

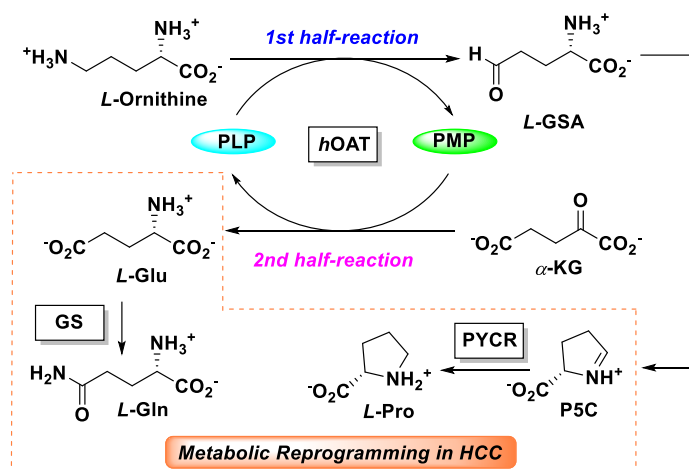


Figure 30. The metabolic role of *h*OAT.

Both OAT and GABA-AT belong to the class-III aminotransferases and demonstrate a similar active site and catalytic mechanism. In contrast to OAT, in the first half-reaction of GABA-AT, GABA is converted to succinic semialdehyde (SSA) in its first half-reaction. The second half-reaction is same for both enzymes though (Figure 30). Over the last few decades, a multidisciplinary research work has been focused on the development of mechanism-based inactivators of GABA-AT for the potential treatment of epilepsies and addictions.⁸⁷ At the early reaction stages, MBIs act as substrates and later they induce chemical transformations that diverge from the native reaction pathway. These new intermediates eventually lead to the inactivation of the target enzymes, mostly by formation of the covalent or tight-binding complexes.⁹⁶ For example, (1*S*,3*S*)-3-amino-4-(difluoromethylene)cyclopentane-1-carboxylic acid (CPP-115, **1**, Figure 31)⁹⁷⁻⁹⁸ was designed and synthesized as a GABA-AT inactivator based on the structure of previously known inactivator, vigabatrin.

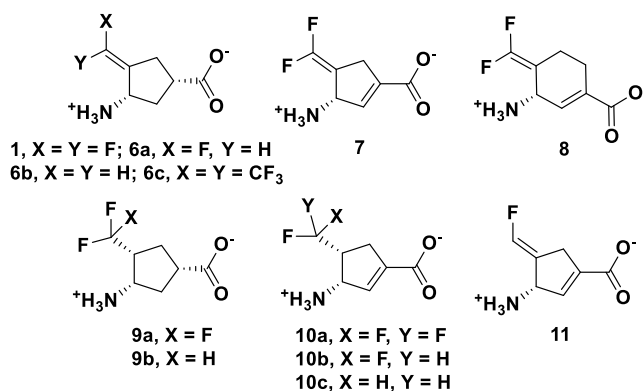


Figure 31. Structures of GABA analogs **1**, **6**-**11**.

In this work, the inactivation mechanisms of *h*OAT by analogs **1** and **7** are presented. In the obtained cocrystal structures of **1** and **7**, the observed *h*OAT inactivation mechanisms were found different from those observed in GABA-AT. Based on the observed cocrystal structures,

synthesized analogs 9a-9b and 10a-10c, along with analog 11 were rationally designed, studied, and compared. The inactivation and turnover mechanisms for 10b were investigated using various biochemical methods such as mass spectrometry (MS), protein crystallography, dialysis experiments, turnover experiments, and fluoride ion release experiments. Subsequently, a stopped-flow experiment was conducted for *hOAT* and 10b, for which the results were consistent with the mechanistic hypothesis and the proposed mechanism. In this thesis, only transient-state kinetics and protein crystallography results are shown and discussed.

Results

X-ray Crystallography of hOAT inactivated by 1 and 7

To investigate the inhibited states of *hOAT* with 1 and 7, we obtained cocrystal structures for both compounds incubated with *hOAT*. The *hOAT* cocrystals with 1 and 7 were grown via the hanging drop vapor diffusion method. The complex formed with 1 diffracted to 2.7Å, while the *hOAT* cocrystal with 7 diffracted to 2.0Å. Both structures were solved by molecular replacement (search model PDB code: 1OAT) and refined using Phenix. As shown in Figure 32, both compounds 1 and 7 formed covalent bonds with the catalytic Lys292 residue in the active site of *hOAT*, which differs from the noncovalent complexes observed in the case of GABA-AT.^{65, 99}

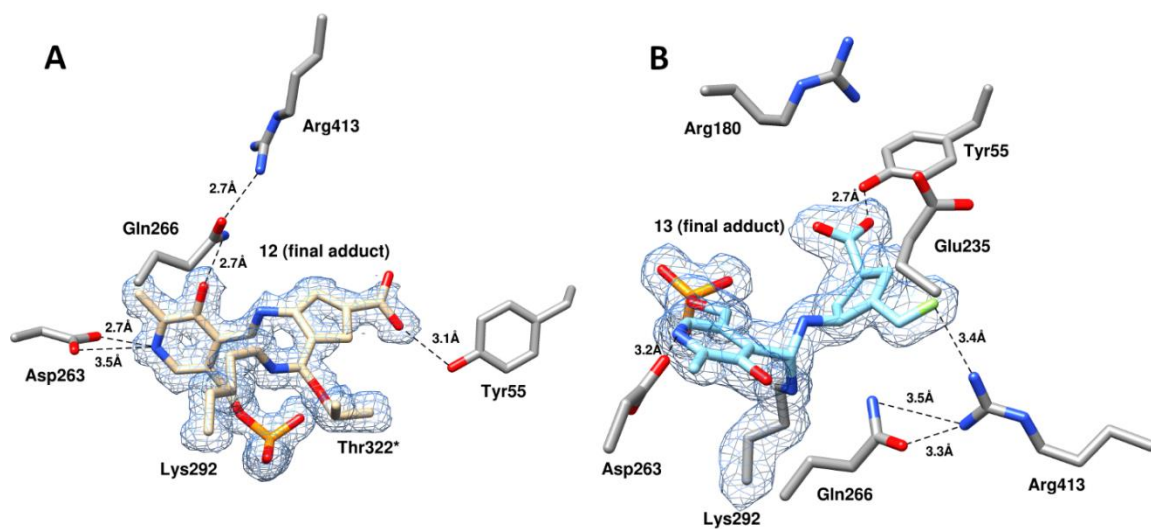
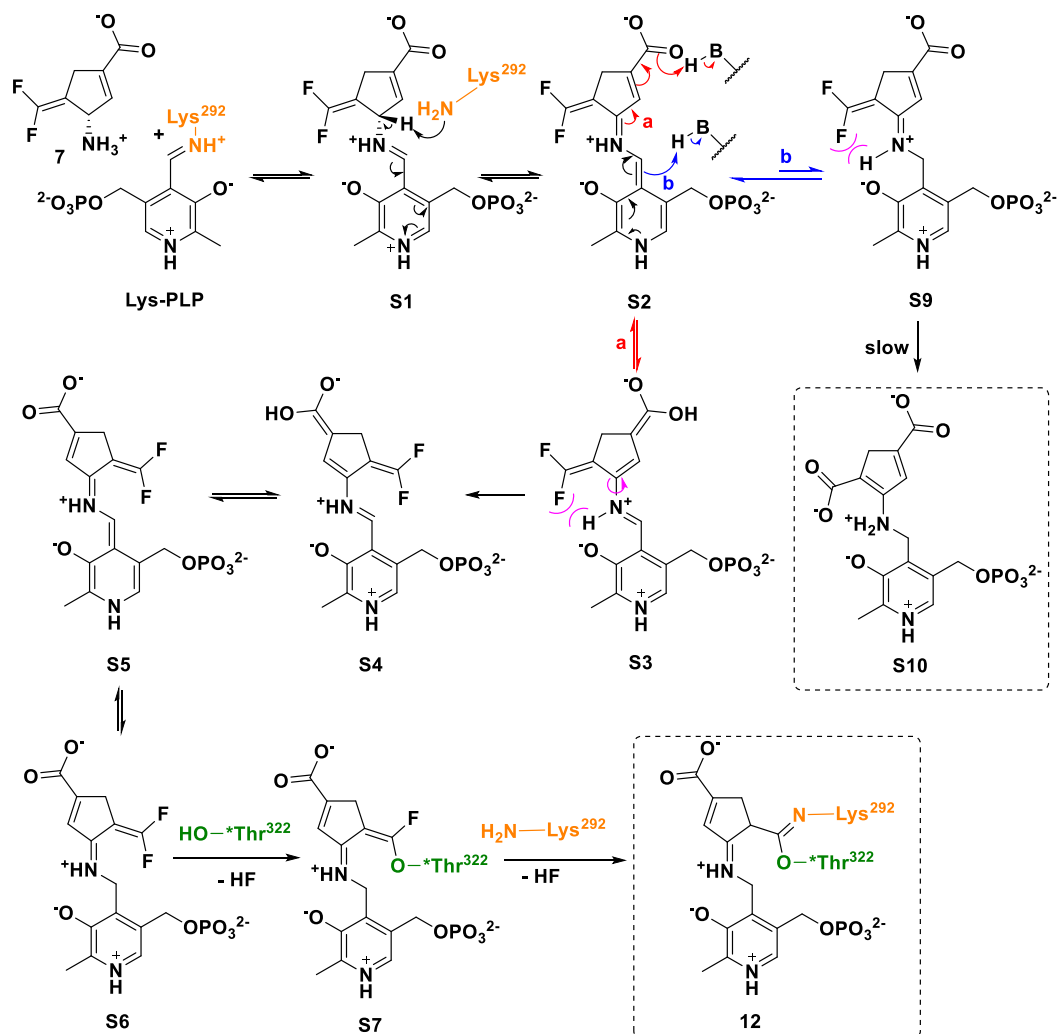


Figure 32. Cocystal structures of *hOAT* inactivated by 7 (A, PDB ID: 7LNM) and 1 (B, PDB ID: 7TFP). For both crystal structures polder ($F_o - F_c$) maps are shown at 3.0 σ .

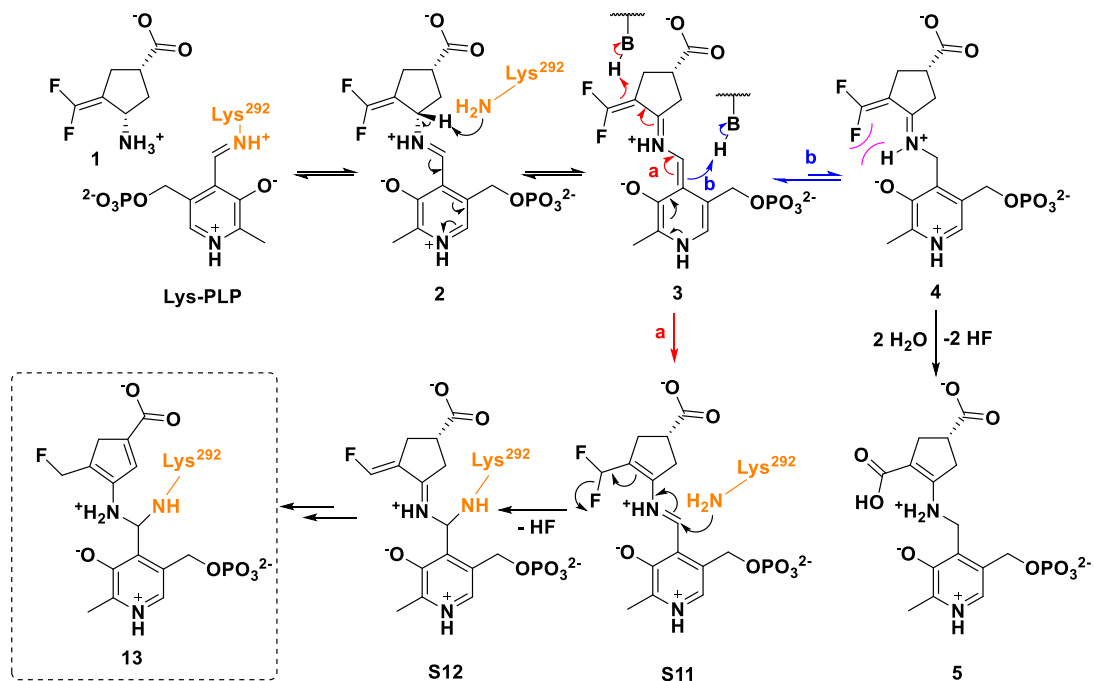
Similar to its six-membered ring analog (8)²⁸, compound 7 was converted to a covalent adduct with the attachments to nearby residues Lys292 and *Thr322 from the adjacent subunit (Figure 32 A). Based on the previous report²⁸, a plausible inactivation mechanism for *hOAT* by 7 is proposed as shown in Scheme 6.



Scheme 6. Plausible Inactivation Mechanisms of *hOAT* by 7.

Michael acceptor intermediate S6 was principally formed because of the potential steric hindrance between the fluorine atom of the warhead and the internal H-bond in S3, followed by the sequential nucleophilic attacks from Lys292 and *Thr322 to form the final adduct (12). Notably, the endocyclic double bond is assumed to play an important role in transforming S2 to S5, as it was found in the mechanism for 8 and *hOAT*.²⁸ In contrast, compound 1 generated a diamine adduct (13, Scheme 7) in the catalytic pocket of *hOAT* (Figure 32 B), in which Lys292

was linked to the C4' position of PLP and one of the fluorine atoms was cleaved from the original warhead.



Scheme 7. Plausible Inactivation Mechanisms of *hOAT* by 1.

Accordingly, a potential inactivation mechanism was proposed as shown in Scheme 7. As with compound 7, potential steric hindrance disfavored the conversion of 3 to Michael acceptor 4 and instead led to the formation of tautomer S11 in the absence of the endocyclic double bond. The final adduct (13) was generated by attack of Lys292 with release of a fluoride ion, which is reminiscent of the enamine inactivation mechanism for vigabatrin.⁹⁹ Overall, crystallography results demonstrated that the mechanism differences between analogs 7 and 8 are derived from the enzymatic machinery rather than the ring size.

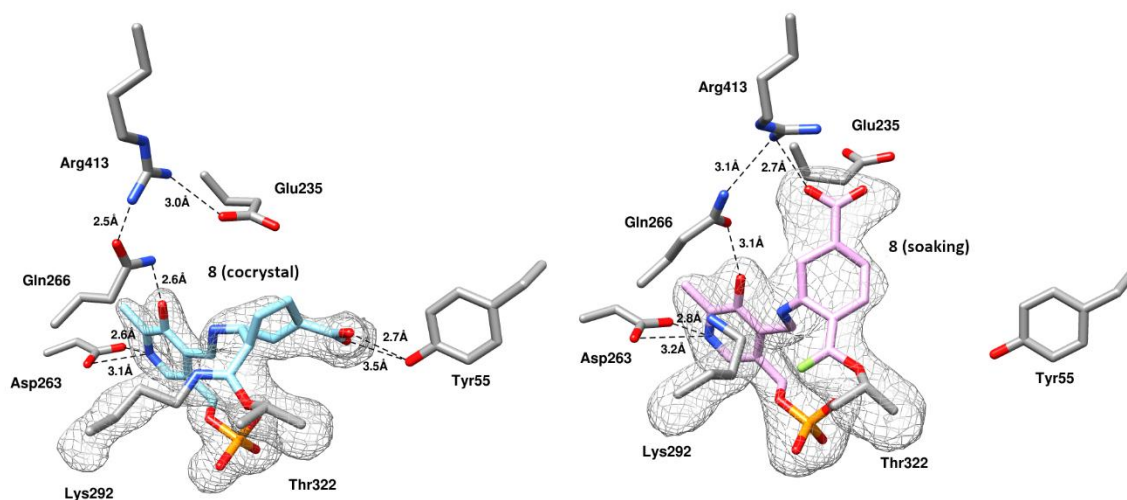


Figure 33. Left: Omit map (at 2.5σ) of *hOAT*-8 cocrystal structure. Right: Omit map (at 2.5σ) of an intermediate formed within active site of *hOAT* during inactivation. Black dashed lines indicate hydrogen bonds. Electron density maps are shown as gray mesh around the ligands.

Based on dialysis and crystallography results it was hypothesized that a ketimine intermediate would be more stable in the active site of *hOAT* compared to GABA-AT resulting selective inhibition potency against *hOAT*, possibly because of the slower rate of hydrolysis. The more stable ketimine could have a better chance to be further elaborated by *hOAT* to generate an active intermediate and then lead to the specific inactivation observed. Thus, analogs 10b and 11 were designed; their potential inactivation mechanisms are shown in Scheme 8.

X-ray Crystallography of hOAT inactivated by 10b and 11

To better elucidate the inactivation mechanism of 10b and 11, protein crystallography of *hOAT* inactivated by 10b and 11 was conducted according to the same procedure as that for *hOAT*-7. *hOAT*-10b crystals diffracted to 1.9 Å resolution and *hOAT*-11 crystals diffracted to 2.6 Å resolution. Both structures were solved by molecular replacement (search model PDB code: 1OAT) and were refined using Phenix.

The refined models for *hOAT-10b* and *hOAT-11* are shown in Figure 35 (polder maps). Both inactivators are covalently linked to the PLP but free from Lys292 and other active site residues. In both structures, the aldehyde group of the ligand forms a hydrogen bond with Gln266. One of the oxygen atoms on the carboxylate group of both inactivators forms a strong hydrogen bond with Tyr55 ($\leq 2.5\text{\AA}$), along with interactions with Arg180, resulting in high stability for the protein-ligand system. Overall, the two cocrystal structures are similar, except for the one water molecule observed close to the carboxylate group in the case of *hOAT-10b* (Figure 34) though fewer water molecules are resolved due to lower resolution.

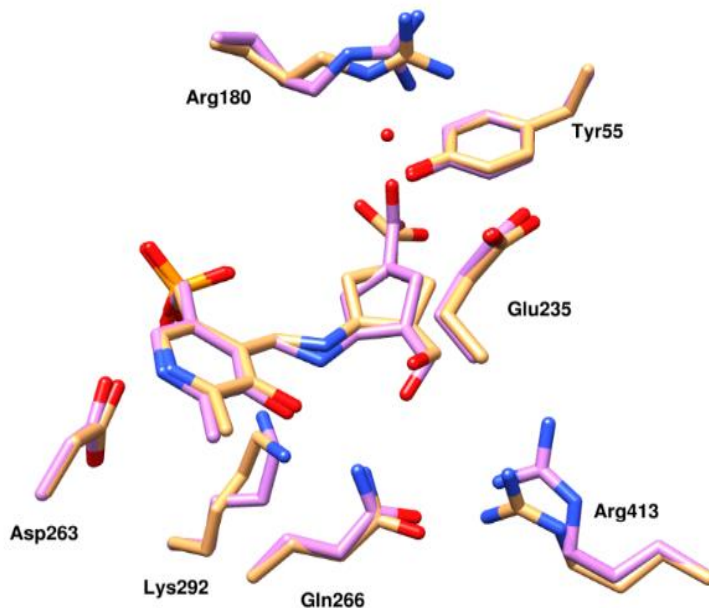


Figure 34. Comparison of *hOAT-10b* and *hOAT-11* models. The *hOAT-10b* model is shown in beige, while the *hOAT-11* model is shown in pink. The water molecule in proximity to Arg180 and Tyr55 belongs to the *hOAT-10b* model only.

Recent work by Carugo et al. has shown that at least a resolution of 1.6Å is required to observe a continuous hydration layer at the protein surface.^{38, 39} Thus, a water molecule resolved at 1.9Å in the *hOAT-10b* cocrystal structure could be present, but not observed at 2.6Å in the cocrystal of *hOAT-11*. Several possible tautomers of *hOAT-10b* and *hOAT-11* products were built into the model and refined using the same strategy. Among them, endocyclic adduct 34 (Figure 35 C) was chosen since it had the lowest B factors for the ligand in all three subunits within the asymmetric unit, although other possible tautomers cannot be excluded.

Based on the proposed inactivation mechanism for 1 and 7, active intermediate 17b (scheme 8) was assumed to be formed from analog 11 in the active site of *hOAT*, followed by water attack to afford tightly binding adduct 34 (Figure 35 C). This result is consistent with the hypothesis that there is a potential for steric hindrance between the fluorine of the warhead and the internal H-bond in the cases of difluoromethylene analogs 1 and 7.

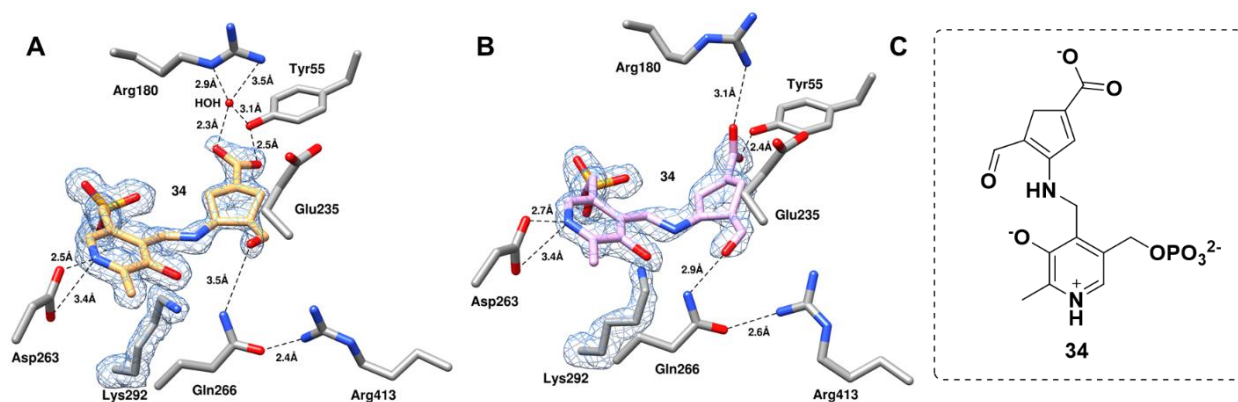
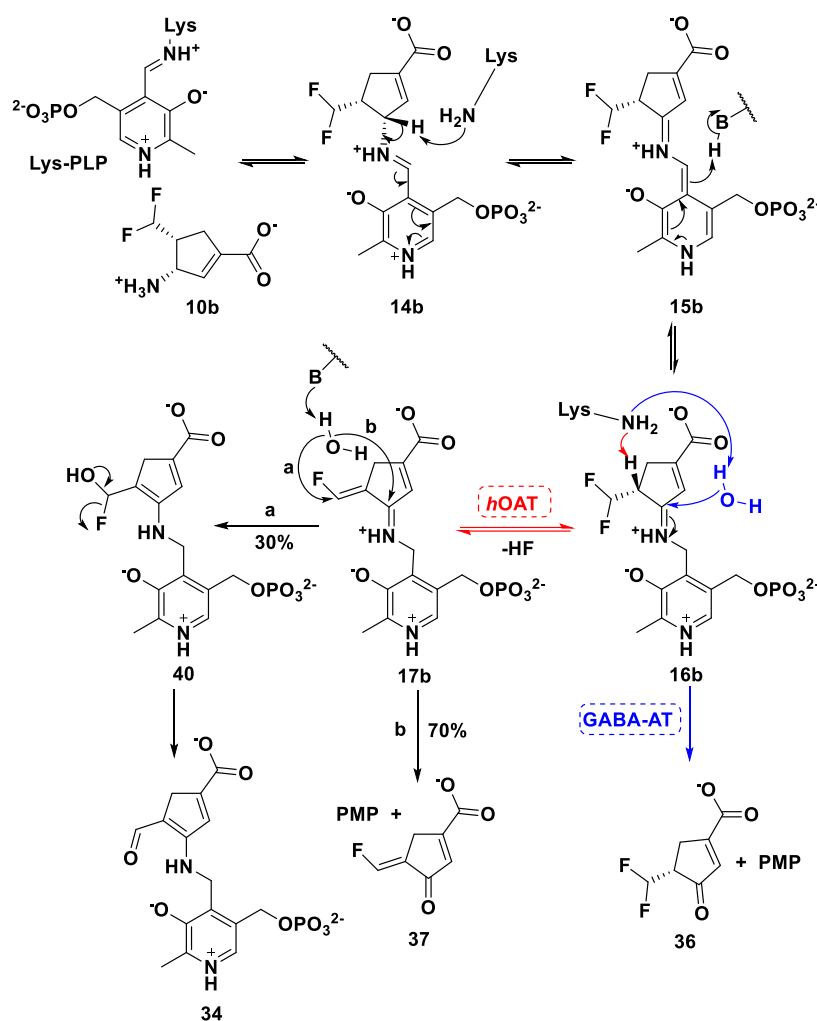


Figure 35. A) Cocystal structure of *hOAT* inactivated by 10b (PDB ID: 7TEV); B) Cocystal structure of *hOAT* inactivated by 11 (PDB ID: 7TED); for both crystal structures polder ($F_o - F_c$) maps are shown at 3.0σ . C) Structure of final adduct 34.

Considering the similarity between the above cocystal structures, the same intermediate (17b) is expected to be generated during the inactivation of *hOAT* by 10b. The subsequent water attack on the fluorinated methylene leads to the formation of final adduct 34 (Figure 35 C).

Transient State Measurements of hOAT Inhibited by 10b



Scheme 8. Plausible mechanism for 10b with *hOAT* and GABA-AT.

As shown in Scheme 8, various transient states were proposed to be involved in the mechanism of *hOAT* inhibition by 10b. For a better interpretation of this process, rapid mixing absorption measurements were performed to detect spectrophotometric evidence for the intermediate sequence. Initially, singular value decomposition analysis was performed on a spliced composite data set collected from two-time frames using a charge-coupled device (CCD) for a single concentration of 10b (500 μ M). The model-free analysis indicated the presence of

five components, but one of them was deemed to be noise and was culled. The data were thus fit to a three step, four species linear irreversible model (Figure 36). The wavelength of components (Int. Ald, Ext. Ald, M1, M2 and P1) observed in spectra matched well with the corresponding intermediates (Lys-PLP, 14b, 16b, 17b, and 34 + PMP) proposed in Scheme 8. To further investigate the wavelength of final adduct 34 and the composition of P1, it was further mixed with excess amounts of α -KG (250 μ M final) in the presence and absence of excess 10b, correspondingly. These data indicated that peaks at \sim 330 nm and \sim 380 nm in P1 were both increased when treated with excess 10b and α -KG (Figure 37, P2). This was interpreted as the reverse and forward half-reactions, consuming the residual PMP by conversion to PLP and successive fractional conversions to 34 that ultimately lead to complete inactivation. This suggested that there are two absorption maxima for 34, possibly as a result of its high conjugation (Scheme 9, P2). On the other hand, the peak at \sim 330 nm was greatly decreased, and the peak at \sim 380 nm was shifted toward the internal aldimine (\sim 420 nm) when only treated with excess α -KG (Figure 37, P3), which could be explained by the dominant conversion of PMP to PLP with limiting 10b (Scheme 9, P3). Overall, the deconvoluted spectra were highly consistent with the proposed mechanism.

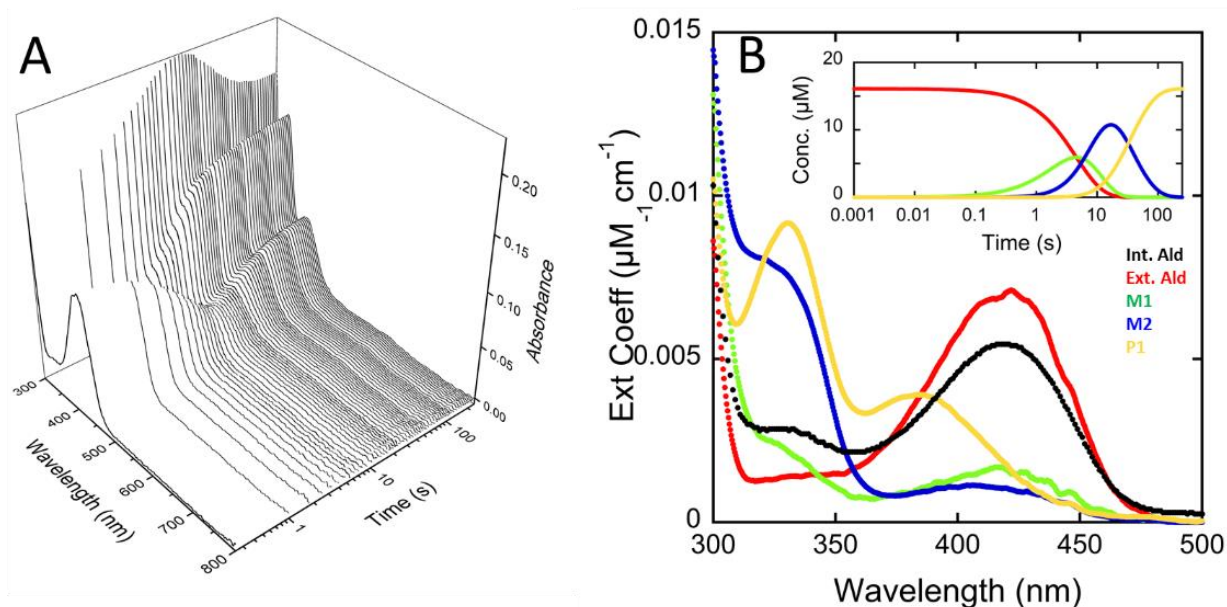


Figure 36. Spectral deconvolution of the *hOAT*, 10b reaction. A) *hOAT* (16.1 μM final) was mixed with 10b (500 μM final), and spectra were recorded with a logarithmic spacing for two time frames: 0.0025 – 12.4 sec and 0.0025 – 1280 sec. These datasets were spliced together at 12.4 sec, and the combined dataset was deconvoluted by fitting to a linear three-step model using singular value decomposition. B) Deconvoluted, noise-filtered spectra. The progression of species is indicated in the inset, and the spectrum of the resting internal aldimine of *hOAT* is shown in black and represents the zero-time spectrum.

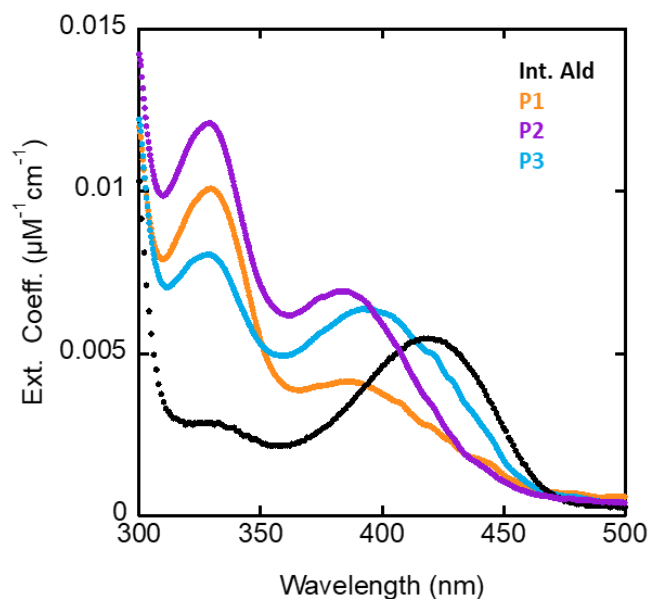


Figure 37. Spectra observed during inactivation by 10b. The black spectrum is the resting PLP state of *hOAT*, included here for reference. The orange spectrum is *hOAT* after reaction with excess 10b. The purple spectrum is obtained when the form shown in orange is allowed to react with both α -KG (250 μ M) and 10b (250 μ M) for 250 sec and presumably is the product of multiple turnovers in the forward and reverse directions that ultimately leads to complete covalent inhibition of *hOAT*. The blue spectrum is a successive composite state observed when the orange species is allowed to react with α -KG (250 μ M) alone.

converts the enzyme to the PMP state (P1). The dependence of the observed rate constant for the second phase showed no clear trend with data scattered about an average of 0.02 s^{-1} (Figure 38 C), which was assigned to the formation of P1 from intermediate M2 (Scheme 9) for this reaction that predicts only absorption changes for k_2 and k_4 at this wavelength (see below). The data obtained from 320 nm report on the latter steps in the forward reaction of *h*OAT with 10b (Figure 39).

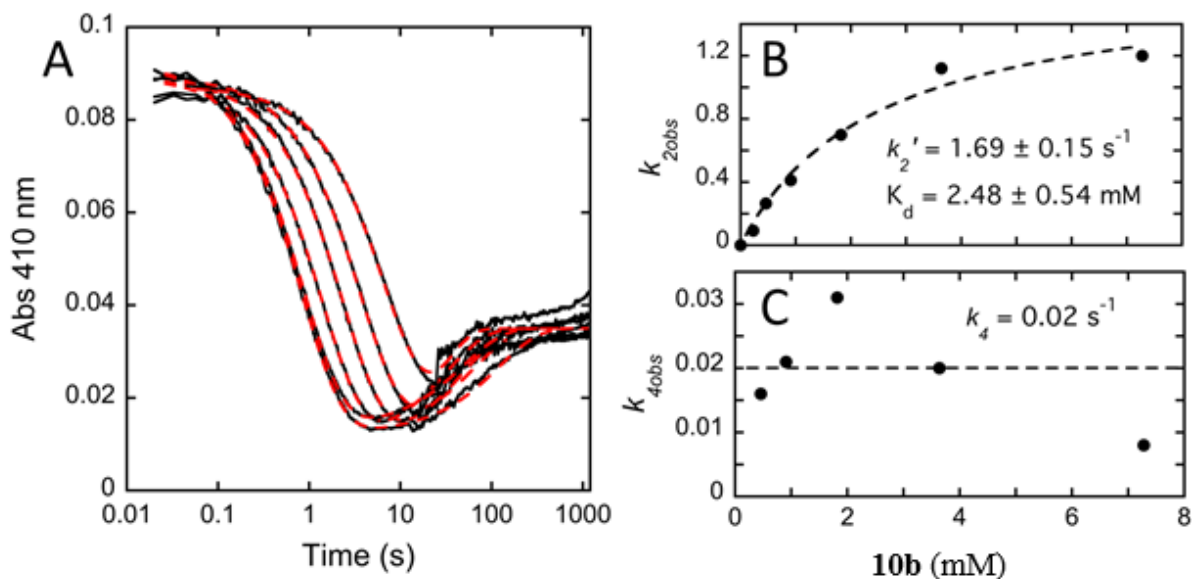


Figure 38. Kinetic analysis of the *h*OAT-10b reaction at 410 nm. *h*OAT ($16.1 \mu\text{M}$ final) was allowed to react with varied 10b concentrations (230, 460, 910, 1820, 3640, 7280 μM final). Spectra were recorded with a logarithmic spacing for two-time frames: 0.0025 – 12.4 sec and 0.0025 – 1280 sec. A. These datasets were spliced together at 12.4 sec and individual traces at 410 nm were extracted from the combined dataset. These data were fit analytically to equation ($Abs = A_1(e^{-k_1t}) + A_2(e^{-k_2t}) + C$) based on pseudo-first order reactant ratios. B & C. The dependence of the observed rate constants. The data in B. were fit to equation ($k_{1obs} = k_1[10b]/(K_{10b} + [10b])$), to determine the intrinsic rate of decay of the external aldimine and the dissociation constant for 10b to *h*OAT. The data did not fit, and the dashed line shown represents the average rate constant for the second phase observed.

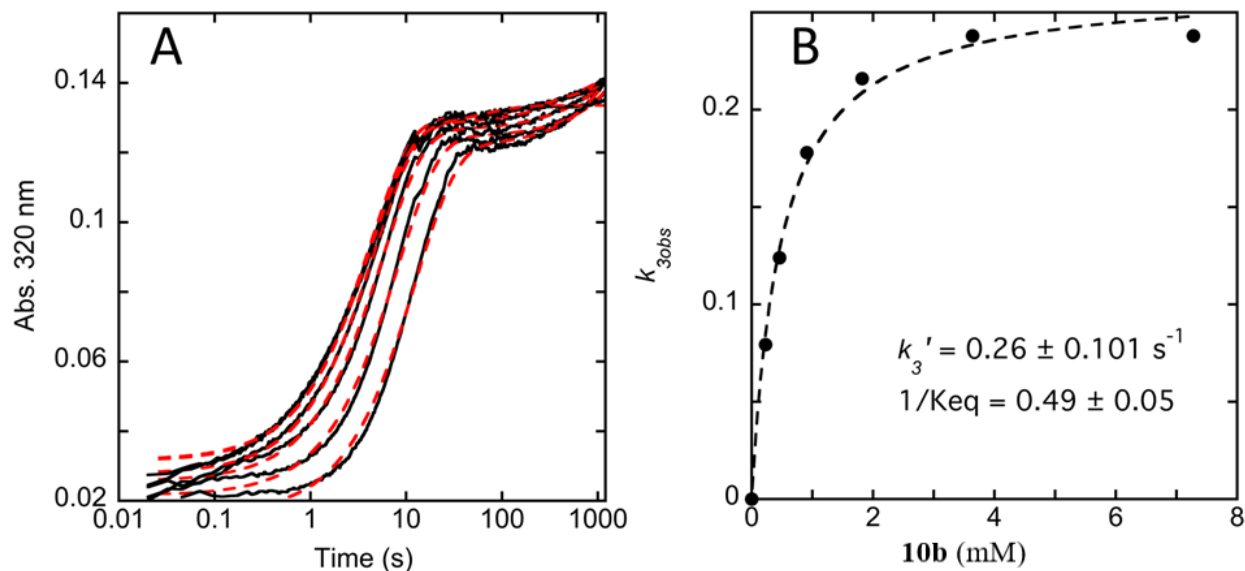


Figure 39. Kinetic analysis of the *h*OAT-10b reaction at 320 nm. *h*OAT (16.1 μ M final) was allowed to react with varied 10b concentrations (230, 460, 910, 1820, 3640, 7280 μ M final). Spectra were recorded with a logarithmic spacing for two time frames: 0.0025 – 12.4 sec and 0.0025 – 1280 sec. A. These datasets were spliced together at 12.4 sec and individual traces at 320 nm were extracted from the combined dataset. These data were fit analytically to equation ($Abs = A_1(e^{-k_1t}) + A_2(e^{-k_2t}) + C$) based on pseudo-first order reactant ratios. B. The dependence of the observed rate constant for the first phase. The data in B. were fit to equation ($k_{1obs} = k_1[10b]/(K_{10b} + [10b])$) to determine the net rate of decay of intermediate I and an estimate of the equilibrium constant for the preceding step.

The dependence of the observed rate constant at this wavelength is also described by a hyperbolic curve according to equation ($k_{1obs} = k_1[10b]/(K_{10b} + [10b])$), indicating the influence of reversibility in the preceding step (k_2, k_{-2}) that consumes the external aldimine. The limit of the dependence indicates a net rate constant (k_3' , Scheme 9) of $0.26 \pm 0.10 \text{ s}^{-1}$ for the formation of intermediate M2. The data at this wavelength also showed small increases in optical density beyond ~ 500 sec, which were not assigned in this analysis. Notably, the fit of the CCD data sets (500 μ M of 10b) indicated successive rate constants of 0.22, 0.21, 0.03 s^{-1} qualitatively in agreement with the observed rate constants for k_2', k_3', k_4 (Figures 38 & 39). The spectra

obtained are shown in Figure 36 B and are overlaid with the internal aldimine spectrum acquired from the resting enzyme that serves as a representation of the time zero state of the reaction. As shown in Scheme 9, this sequence of spectra combined with the concentration dependencies indicate that the external aldimine (14b) forms an equilibrium accumulation rapidly and reversibly within the deadtime of the stopped-flow instrument with a weak binding constant of ~ 2.5 mM (K_d). The first phase observed is the decay of the external aldimine (M1) with a rate constant of ~ 1.7 s⁻¹ (k_2') to yield a weakly absorbing intermediate state that then decays at ~ 0.26 s⁻¹ (k_3') to form a second intermediate species (M2) with a prominent shoulder at 320 nm. This state then decays at ~ 0.02 s⁻¹ (k_4) to form the PMP state (P1) of the enzyme (Figure 36 B). Although abstraction of the γ -proton was previously proven to be the rate-determining step for the reaction of GABA-AT and inactivators, kinetics measurements for the reaction of *h*OAT and 10b showed that the hydrolysis step (k_4) from M2 to P1 is much slower than the other two deprotonation steps (k_2' and k_3'), which supports our initial hypothesis that a relatively slower hydrolysis step might be involved for GABA analogs in the catalysis process of *h*OAT compared to that of GABA-AT.

Discussion

Human ornithine aminotransferase (*h*OAT) is a pyridoxal 5'-phosphate (PLP) dependent enzyme that demonstrates a similar active site to that of γ -aminobutyric acid aminotransferase (GABA-AT). Over the last few years, selective inhibition of *h*OAT has been recognized as a potential treatment for cancers, especially hepatocellular carcinoma (HCC). In this work, we first demonstrated the inactivation mechanisms of *h*OAT by two well-known GABA-AT inactivators, 1 and 7. Interestingly, irreversible covalent adducts (12 and 13) were generated from them in the

active site of *hOAT*, while 1 and 7 were identified as partially irreversible inhibitors of GABA-AT with the formation of noncovalent, tight-binding adducts. This observation might result from a potential enzymatic machinery difference between these two aminotransferases leading to a relatively slower hydrolysis rate with *hOAT*. Inspired by the above findings, a series of analogs (10a, 10b, and 11a-11c) were designed and synthesized. Among them, the best compound 10b was found to be 5.3 times more efficient as an inactivator of *hOAT* than 6c, which exhibited potent *in vivo* antitumor efficacy. Furthermore, analog 10b demonstrated weak inhibitory activity against other human aminotransferases (GABA-AT, Asp-AT, and Ala-AT), even at high concentrations. Intact protein mass spectrometry, protein crystallography, and dialysis experiments showed that analog 10b was converted to active intermediate 17b via a second-deprotonation process, leading to the formation of a tight-binding adduct (34) and irreversible inhibition of *hOAT*. To further elucidate the mechanistic details of *hOAT* and 10b, the stopped-flow experiments were conducted, which revealed the identity of intermediates and reaction rates for each step. Not only was this result highly consistent with the proposed mechanism (Scheme 8) but it also identified the slow hydrolysis step for *hOAT*, which matched with the inactivation mechanisms for 1 and 7. The novel second-deprotonation mechanism for 10b contributes to its high potency and significantly enhanced selectivity over other aminotransferases, especially GABA-AT.

Experimental procedures

Cocrystallization of hOAT with 1, 7, 10b and 11

After purification, *hOAT* was buffer exchanged into the crystallization buffer (50 mM Tricine pH 7.8) supplemented with 1 mM α -ketoglutarate. The protein was concentrated to 6.5

mg/mL. Previously reported crystallization⁵ conditions were optimized using the hanging drop vapor diffusion method by varying PEG 6000 (8-12%), NaCl (100-250 mM), and glycerol (0%-10%) with 100 mM Tricine pH 7.8 being kept constant as the buffer. For each hanging drop, 2 μ L of protein solution was mixed with an equal volume of well solution and 0.5 μ L of 10 mM 10b or 11. The crystals with the best morphology and size grew in a final condition containing 12% PEG 6000, 200 mM NaCl, 10% glycerol, and 100 mM Tricine pH 7.8. Crystals were transferred to a cryo-protectant solution (well solution supplemented with 30% glycerol) and flash-frozen in liquid nitrogen.

X-ray diffraction and data processing

Monochromatic X-ray diffraction data were collected at the LS-CAT beamline 21-ID-D at the Advanced Photon Source at Argonne National Laboratory. Data were collected at a wavelength of 1.127 Å and a temperature of 100 K using a Dectris Eiger 9M detector. Data sets were processed and analyzed with autoPROC⁵¹ or Xia2⁸⁸ software.

Model building and refinement

The *hOAT* structure was solved by molecular replacement using PHASER⁵³ in Phenix. The starting search model was the previously published structure of *hOAT* (PDB code: 1OAT). The model building and refinement were accomplished in Coot⁵⁵ and Phenix⁵⁴, respectively, as an iterative process until the lowest possible R_{free}/R factor values were attained. Structural depiction figures were prepared using UCSF Chimera⁵⁶.

Table 5. Statistics of the crystal structure of *hOAT* inactivated by compound 1, 7, 10b and 11.

Complex	<i>hOAT</i> -10b	<i>hOAT</i> -11	<i>hOAT</i> -1	<i>hOAT</i> -7
PDB code	7TEV	7TED	7TFP	7LNM
Space group	P 3 ₂ 2 1	C 1 2 1	P 3 ₂ 2 1	P 3 ₂
Unit Cell dimension				
α, β, γ (deg)	90.0, 90.0, 120.0	90.0, 94.8, 90.0	90.0, 90.0, 120.0	90.0, 90.0, 120.0
a, b, c (Å)	115.8, 115.8, 187.4	200.1, 115.4, 185.7	115.7, 115.7, 186.8	115.7, 115.7, 188.0
Processed Resolution (Å)	1.91	2.63	2.71	2.00
R _{merge} ^a (%)	14.5 (179.9)	14.8 (85.9)	23.6 (183.8)	11.8 (108.6)
R _{pim} ^c (%)	6.1 (80.4)	11.7 (68.1)	9.7 (77.4)	6.8 (67.8)
I/ σ (I)	10.6 (1.1)	8.2 (1.7)	6.0 (1.0)	4.6 (1.3)
CC 1/2 d (%)	99.8 (29.6)	98.7 (29.4)	98.6 (31.0)	99.3 (37.6)
Completeness (%)	99.8 (97.5)	98.9 (98.6)	96.5 (98.8)	100.0 (100.0)
Multiplicity	12.7 (10.4)	4.7 (4.7)	6.4 (6.3)	3.9 (3.5)
No. Reflections	1439824 (56625)	579095 (42812)	242439 (17920)	749788 (33035)
No. Unique Reflections	113351 (5443)	123624 (6094)	37903 (2823)	190270 (9377)
Refinement				
R _{work} ^e /R _{free} ^f (%)	25.50/26.80	28.00/28.60	22.60/26.80	15.80/18.60
No. of Atoms				
protein	9464	28449	9433	18938
ligand	78	234	65	246
water	592	326	252	1690
Average B factors (Å ²)				
protein	34.50	46.50	53.90	40.90
RMSD ^g				
bond lengths (Å)	0.012	0.011	0.002	0.003
bond angles (deg)	1.59	1.52	0.50	0.60
Ramachandran plot (%)				
favored	95.34	94.00	95.24	96.63
allowed	4.46	5.20	4.36	3.17
outliers	0.20	0.80	0.40	0.20
^a R _{merge} = $\sum I_{\text{obs}} - I_{\text{avg}} / \sum I_{\text{avg}}$, ^b The values for the highest-resolution bin are in parentheses, ^c Precision-indicating merging R, ^d Pearson correlation coefficient of two "half" data sets, ^e R _{work} = $\sum F_{\text{obs}} - F_{\text{calc}} / \sum F_{\text{obs}}$, ^f Five percent of the reflection data were selected at random as a test set, and only these data were used to calculate R _{free} , ^g Root-mean square deviation.				

The reaction of 10b with *h*OAT was observed in the transient state using a Hitech Scientific (TgK) stopped-flow spectrophotometer with charged coupled device (CCD) detection from 260-800 nm. *h*OAT (16.1 μ M) was allowed to react at 10 °C with varied 10b concentrations (230, 460, 910, 1820, 3640, 7280 μ M) in 50 mM HEPES, 200 mM NaCl, pH 7.5. For each concentration of the inhibitor, CCD spectral datasets were collected in duplicate for two timeframes, 0.0025 – 12.4 sec and 0.0025 – 1280 sec, and the duplicates were averaged. Datasets were spliced together at 12 sec to form one dataset with time resolution to sufficiently represent rapid and slow processes. Extracted for the individual the wavelengths 320 and 410 nm were fit to equation (1) that describes two successive first-order processes. In this equation *Abs* is absorbance, A_x are the amplitudes associated with each observed phase, k_x are the corresponding rate constants, and *C* is the absorbance endpoint. Dependences were fit to equation (2) that describes a rectangular hyperbola based on pre-equilibrium binding of the inhibitor.

Equation 10:
$$Abs = A_1(e^{-k_1t}) + A_2(e^{-k_2t}) + C$$

Equation 11:
$$k_{1obs} = k_1[10b]/(K_{10b} + [10b])$$

The spliced datasets from *h*OAT (16.1 μ M) reacting with 10b (500 μ M) at 10 °C were fit and deconvoluted based on a linear four-species model using the Spectra fit singular value decomposition module of KinTek Explorer software. The rate constant estimates used were the values determined from analytical fits to equation 11.

The enzyme form that accumulated from the reaction of *h*OAT_{PLP} with 10b was allowed to react with α -ketoglutarate. Using double mixing stopped-flow methods, *h*OAT (19.25 μ M) was allowed to react with 10b (18.75 μ M) and aged for 300 sec prior to the reaction with α -KG (250 μ M). The reaction was monitored for 500 sec using CCD. These data were fit and

deconvoluted based on a linear irreversible three-species model using the Spectra fit singular value decomposition module of KinTek Explorer software.

CONCLUSION

Human Ornithine Aminotransferase is an important drug target in a combat against hepatocellular carcinoma. In the last years it has been extensively studied by our group using multidisciplinary approach, which proved to be an efficient way to investigate enzyme's properties and reaction mechanisms. Transient-state measurements along with soaking experiments and ^{19}F -NMR studies have been added to the previously used mass spectromic analysis, steady-state assays, and X-ray cocrystal structures. This integrative approach allowed to investigate mechanisms of *h*OAT reactions with its substrates and inactivators to the great details which were not possible before. Implementation of the new techniques led to the quantitative and accurate determination of the reaction intermediates, their observed formation and decay rates as well as the binding affinity of potential ligands. Due to the new approach, the rate-limiting step of ligand's reaction with *h*OAT could now be elucidated and even cross validated by the protein crystal soaking experiments and ^{19}F -NMR. Comprehension of the rate-determining step is crucial to the understanding of efficient and specific *h*OAT inactivation and rational design of its novel potential inactivators.

For the first time, new interdisciplinary method was applied to the investigation of inactivation mechanism of BCF_3 . It resulted in the discovery of four distinguished intermediate species (internal aldimine, external aldimine I, quinonoid, and external aldimine II). The decay

of external aldimine II was identified as a rate-limiting step of the reaction and the structure of the intermediate was achieved separately in the crystal soaking experiment.

The structure of external aldimine II provided a rationale for the relatively high partition ratio of turnover pathway to inactivation pathway. In addition, it was the first intermediate structure ever captured in the active site of *hOAT*, thus it was intriguing to detect the position of active site residues during enzyme's inactivation. The ^{19}F -NMR experiments not only supported the transient-state and crystal soaking experiments, but also supplied a proof on E or Z elimination of the single fluorine that yields to one of the two possible configurations of the external aldimine II. Combined with the soaking results, it was concluded that only the E-isomer of external aldimine II can advance to form the covalently inhibited complex. Overall, the insights gained during this investigation led to the understanding of the interaction between *hOAT* and BCF_3 as well as mechanistic properties of the enzyme. The data collected in this investigation later served as a basis for the development of novel *hOAT* inactivators with improved potency and partition ratio.

Inspired by the results achieved during the mechanism study on BCF_3 , the same approach was applied on novel *hOAT* inactivators. Among them, the most thorough analysis was performed on compounds 148 and 136. Combination of transient-state kinetics experiments along with the protein cocrystallization and soaking experiments helped to obtain essential information about their complicated reaction mechanisms. As in case of BCF_3 , the stopped-flow identified several reaction intermediates for 148 and 136, estimated their observed rate constants, and determined a rate-limiting step for their inactivation reactions. The cocrystal structures, in turn, revealed the final adducts of the inactivation pathways which were separately confirmed by

the mass spectrometry. In the crystal soaking experiment with compound 148, quasi-stable gem-diamine intermediate was observed for the first time in *hOAT* active site. To sum up, compounds 148 and 136 showed themselves as promising *hOAT* inactivators with improved potency ($k_{\text{inact}}/K_{\text{I}} = 4.72 \text{ min}^{-1}\text{mM}^{-1}$ for 136 and $k_{\text{inact}}/K_{\text{I}} = 1.30 \text{ min}^{-1}\text{mM}^{-1}$) when compared to BCF_3 ($k_{\text{inact}}/K_{\text{I}} = 1.00 \text{ min}^{-1}\text{mM}^{-1}$). Moreover, compound 136 expressed the best partition ratio among all current *hOAT* inactivators (~30% inactivation for 136, ~8% for BCF_3 , < 3% for 148).

Finally, the same techniques were employed to investigate fundamental properties of *hOAT*: its pH profile, substrate specificity, and binding affinity towards alternative substrates. It was determined that for the first half-reaction the kinetic pKa is equal to 7.91 ± 0.14 , and 7.74 ± 0.07 for the second half-reaction. Observed subtle difference in pKa values hints at the possibility that the same group was acting in the rate-limiting step of both the first and the second half-reaction. The transient-state studies with alternative substrates (AVA, DABA, and GABA) showed that *hOAT* is a relatively promiscuous enzyme, which is a common case for aminotransferases. Interestingly, the kinetics studies showed that the substrates without α -amino group expressed a significant reversibility of their reaction. In case of GABA, the reaction was displaying ~92% external aldimine at equilibrium in the presence of 1 mM GABA. Based on these results, a hypothesis was proposed that α -amino group facilitates the product release ensuring irreversibility of the first half-reaction. More specifically, it was speculated that cyclization step initiated by the α -amino group could in theory bypass a hydrolysis step, the formation of GSA, and eventually result in a faster product release route. Based on the observed reaction reversibility for GABA, it could be possible that “uncyclizable” analogs of GABA could

be developed as inhibitory therapeutics against the cancer target *hOAT* if binding selectivity was achieved.

The work summarized in this dissertation demonstrated four possible modes of *hOAT* inhibition (Figure 40). They consist of competitive inhibition with “uncyclizable” analogs of GABA, irreversible inhibition by covalent modification of PLP only (compound 148, 1, and 7), irreversible inhibition by covalent modification of PLP and catalytic Lys292 (BCF₃, compound 13), and irreversible inhibition by covalent modification of PLP, catalytic Lys292, and *Thr322 (compound 8, 12).

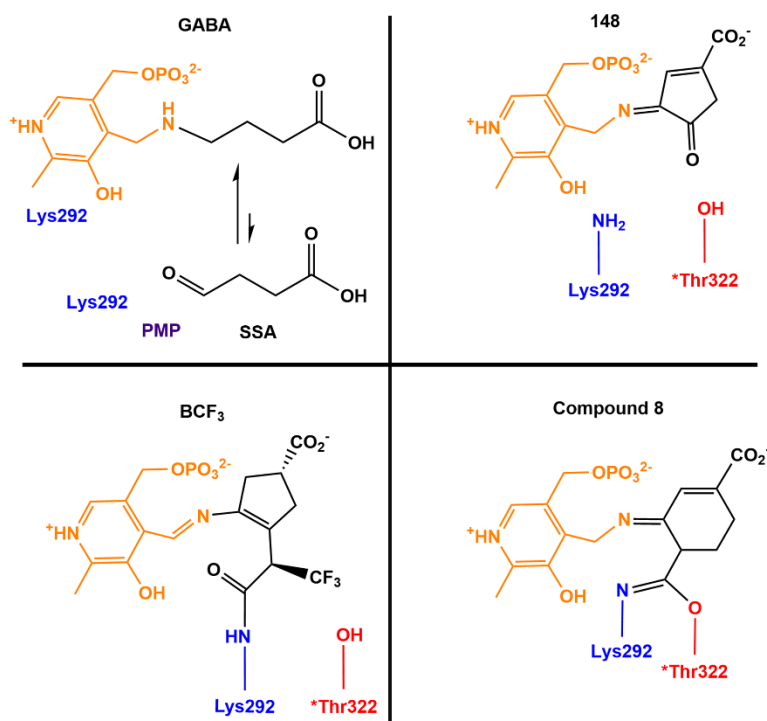


Figure 40. Four different inhibition modes discovered for *hOAT*.

Currently it is still difficult to design a novel *hOAT* inhibitor with *a priori* known properties and inhibition mode. Nevertheless, the research work performed in the last years

derived several important factors that should be considered during the rational design of a novel *hOAT* inactivator. These considerations should include (but not limited to): the appropriate ring size, conjugation of the system, ligand's length, electrostatic potential of the intermediates, presence of the specific functional groups. The work on development of a potent and selective inhibitors of *hOAT* is still not completed. However, major improvements were made in the last years, and today several potential drug candidates against *hOAT* are progressing towards their clinical trials giving hope to people fighting against HCC.

REFERENCE LIST

1. Herzfeld, A.; Knox, W. E., The Properties, Developmental Formation, and Estrogen Induction of Ornithine Aminotransferase in Rat Tissues. *Journal of Biological Chemistry* **1968**, *243* (12), 3327-3332.
2. Wang, T.; Lawler, A. M.; Steel, G.; Sipila, I.; Milam, A. H.; Valle, D., Mice lacking ornithine- δ -amino-transferase have paradoxical neonatal hypornithinaemia and retinal degeneration. *Nature Genetics* **1995**, *11* (2), 185-190.
3. Wu, G.; Knabe, D. A.; Kim, S. W., Arginine Nutrition in Neonatal Pigs. *The Journal of Nutrition* **2004**, *134* (10), 2783S-2790S.
4. Tomlinson, C.; Rafii, M.; Sgro, M.; Ball, R. O.; Pencharz, P., Arginine Is Synthesized From Proline, Not Glutamate, in Enterally Fed Human Preterm Neonates. *Pediatric Research* **2011**, *69* (1), 46-50.
5. Kohler, E. S.; Sankaranarayanan, S.; van Ginneken, C. J.; van Dijk, P.; Vermeulen, J. L.; Ruijter, J. M.; Lamers, W. H.; Bruder, E., The human neonatal small intestine has the potential for arginine synthesis; developmental changes in the expression of arginine-synthesizing and -catabolizing enzymes. *BMC Dev Biol* **2008**, *8*, 107.
6. Montioli, R.; Bellezza, I.; Desbats, M. A.; Borri Voltattorni, C.; Salviati, L.; Cellini, B., Deficit of human ornithine aminotransferase in gyrate atrophy: Molecular, cellular, and clinical aspects. *Biochimica et Biophysica Acta (BBA) - Proteins and Proteomics* **2021**, *1869* (1), 140555.
7. Ramesh, V.; Gusella, J. F.; Shih, V. E., Molecular pathology of gyrate atrophy of the choroid and retina due to ornithine aminotransferase deficiency. *Mol Biol Med* **1991**, *8* (1), 81-93.
8. Colnot, S.; Decaens, T.; Niwa-Kawakita, M.; Godard, C.; Hamard, G.; Kahn, A.; Giovannini, M.; Perret, C., Liver-targeted disruption of *Apc* in mice activates β -catenin signaling and leads to hepatocellular carcinomas. *Proceedings of the National Academy of Sciences of the United States of America* **2004**, *101* (49), 17216.
9. Cadoret, A.; Ovejero, C.; Terris, B.; Souil, E.; Levy, L.; Lamers, W. H.; Kitajewski, J.; Kahn, A.; Perret, C., New targets of β -catenin signaling in the liver are involved in the glutamine metabolism. *Oncogene* **2002**, *21* (54), 8293-8301

10. Yang, J. D.; Roberts, L. R., Hepatocellular carcinoma: a global view. *Nature Reviews Gastroenterology & Hepatology* **2010**, *7* (8), 448-458.
11. Sherman, M.; Bruix, J.; Porayko, M.; Tran, T.; for the, A. P. G. C., Screening for hepatocellular carcinoma: The rationale for the American Association for the Study of Liver Diseases recommendations. *Hepatology* **2012**, *56* (3), 793-796.
12. Personeni, N.; Rimassa, L. In *Hepatocellular carcinoma: a global disease in need of individualized treatment strategies*, American Society of Clinical Oncology: **2017**.
13. Sayiner, M.; Golabi, P.; Younossi, Z. M., Disease Burden of Hepatocellular Carcinoma: A Global Perspective. *Digestive Diseases and Sciences* **2019**, *64* (4), 910-917.
14. de Lope, C. R.; Tremosini, S.; Forner, A.; Reig, M.; Bruix, J., Management of HCC. *Journal of Hepatology* **2012**, *56*, S75-S87.
15. Milgrom, D. P.; Maluccio, M. A.; Koniaris, L. G., Management of Hepatocellular Carcinoma (HCC). *Current Surgery Reports* **2016**, *4* (6), 20.
16. de Rosamel, L.; Blanc, J.-F., Emerging tyrosine kinase inhibitors for the treatment of hepatocellular carcinoma. *Expert opinion on emerging drugs* **2017**, *22* (2), 175-190.
17. Leathers, J. S.; Balderramo, D.; Prieto, J.; Diehl, F.; Gonzalez-Ballerga, E.; Ferreira, M. R.; Carrera, E.; Barreyro, F.; Diaz-Ferrer, J.; Singh, D.; Mattos, A. Z.; Carrilho, F.; Debes, J. D., Sorafenib for Treatment of Hepatocellular Carcinoma: A Survival Analysis From the South American Liver Research Network. *Journal of Clinical Gastroenterology* **2019**, *53* (6).
18. Zigmond, E.; Ben Ya'acov, A.; Lee, H.; Lichtenstein, Y.; Shalev, Z.; Smith, Y.; Zolotarov, L.; Ziv, E.; Kalman, R.; Le, H. V.; Lu, H.; Silverman, R. B.; Ilan, Y., Suppression of Hepatocellular Carcinoma by Inhibition of Overexpressed Ornithine Aminotransferase. *ACS Med Chem Lett* **2015**, *6* (8), 840-4.
19. Ginguay, A.; Cynober, L.; Curis, E.; Nicolis, I., Ornithine Aminotransferase, an Important Glutamate-Metabolizing Enzyme at the Crossroads of Multiple Metabolic Pathways. *Biology*. *7*, *6* (1). pii: E18. 2017.
20. Peraino, C., Functional properties of ornithine-ketoacid aminotransferase from rat liver. *Biochimica et Biophysica Acta (BBA) - Enzymology* **1972**, *289* (1), 117-127.
21. Butrin, A.; Beaupre, B. A.; Kadamandla, N.; Zhao, P.; Shen, S.; Silverman, R. B.; Moran, G. R.; Liu, D., Structural and Kinetic Analyses Reveal the Dual Inhibition Modes of Ornithine

- Aminotransferase by (1S,3S)-3-Amino-4-(hexafluoropropan-2-ylidenyl)-cyclopentane-1-carboxylic Acid (BCF3). *ACS Chemical Biology* **2021**, *16* (1), 67-75.
22. Shen, S.; Butrin, A.; Doubleday, P. F.; Melani, R. D.; Beaupre, B. A.; Tavares, M. T.; Ferreira, G. M.; Kelleher, N. L.; Moran, G. R.; Liu, D.; Silverman, R. B., Turnover and Inactivation Mechanisms for (S)-3-Amino-4,4-difluorocyclopent-1-enecarboxylic Acid, a Selective Mechanism-Based Inactivator of Human Ornithine Aminotransferase. *Journal of the American Chemical Society* **2021**, *143* (23), 8689-8703.
23. Lide, D. R., Handbook of Chemistry and Physics, ed. CRC Press, Boca Raton, Florida, United States of America: **1999**.
24. Hayashi, H.; Kagamiyama, H., Transient-State Kinetics of the Reaction of Aspartate Aminotransferase with Aspartate at Low pH Reveals Dual Routes in the Enzyme–Substrate Association Process. *Biochemistry* **1997**, *36* (44), 13558-13569.
25. Shen, B. W.; Hennig, M.; Hohenester, E.; Jansonius, J. N.; Schirmer, T., Crystal structure of human recombinant ornithine aminotransferase. *Journal of molecular biology* **1998**, *277* (1), 81-102.
26. Jansonius, J.; Génovésio-Taverne, J.-C.; Hennig, M.; Hohenester, E.; Jenny, M.; Malashkevich, V.; Moser, M.; Müller, R.; Shen, B.; Stark, W., Crystallographic studies on the vitamin B 6-assisted enzymic transamination reaction. In *Biochemistry of Vitamin B6 and PQQ*, Springer: **1994**; pp 29-35.
27. Schirotli, D.; Peracchi, A., A subfamily of PLP-dependent enzymes specialized in handling terminal amines. *Biochimica et Biophysica Acta* **2015**, pp 1200-1211.
28. Zhu, W.; Doubleday, P. F.; Butrin, A.; Weerawarna, P. M.; Melani, R. D.; Catlin, D. S.; Dwight, T. A.; Liu, D.; Kelleher, N. L.; Silverman, R. B., Remarkable and Unexpected Mechanism for (S)-3-Amino-4-(difluoromethylenyl)cyclohex-1-ene-1-carboxylic Acid as a Selective Inactivator of Human Ornithine Aminotransferase. *Journal of the American Chemical Society* **2021**, *143* (21), 8193-8207.
29. Zhu, W.; Doubleday, P. F.; Catlin, D. S.; Weerawarna, P. M.; Butrin, A.; Shen, S.; Wawrzak, Z.; Kelleher, N. L.; Liu, D.; Silverman, R. B., A Remarkable Difference That One Fluorine Atom Confers on the Mechanisms of Inactivation of Human Ornithine Aminotransferase by Two Cyclohexene Analogues of γ -Aminobutyric Acid. *Journal of the American Chemical Society* **2020**, *142* (10), 4892-4903.
30. Mascarenhas, R.; Le, H. V.; Clevenger, K. D.; Lehrer, H. J.; Ringe, D.; Kelleher, N. L.; Silverman, R. B.; Liu, D., Selective Targeting by a Mechanism-Based Inactivator against

Pyridoxal 5'-Phosphate-Dependent Enzymes: Mechanisms of Inactivation and Alternative Turnover. *Biochemistry* **2017**, *56* (37), 4951-4961.

31. Moschitto, M. J.; Doubleday, P. F.; Catlin, D. S.; Kelleher, N. L.; Liu, D.; Silverman, R. B., Mechanism of Inactivation of Ornithine Aminotransferase by (1S,3S)-3-Amino-4-(hexafluoropropan-2-ylidene)cyclopentane-1-carboxylic Acid. *Journal of the American Chemical Society* **2019**, *141* (27), 10711-10721.
32. Williams, J. A.; Bridge, G.; Fowler, L. J.; John, R. A., The reaction of ornithine aminotransferase with ornithine. *Biochemical Journal* **1982**, *201* (1), 221-225.
33. Markova, M.; Peneff, C.; Hewlins, M. J.; Schirmer, T.; John, R. A., Determinants of substrate specificity in omega-aminotransferases. *J Biol Chem* **2005**, *280* (43), 36409-16.
34. Mitchell, G. A.; Brody, L. C.; Sipila, I.; Looney, J. E.; Wong, C.; Engelhardt, J. F.; Patel, A. S.; Steel, G.; Obie, C.; Kaiser-Kupfer, M., At least two mutant alleles of ornithine delta-aminotransferase cause gyrate atrophy of the choroid and retina in Finns. *Proceedings of the National Academy of Sciences* **1989**, *86* (1), 197.
35. Khersonsky, O.; Roodveldt, C.; Tawfik, D. S., Enzyme promiscuity: evolutionary and mechanistic aspects. *Current Opinion in Chemical Biology* **2006**, *10* (5), 498-508.
36. Rothman, S. C.; Kirsch, J. F., How Does an Enzyme Evolved In vitro Compare to Naturally Occurring Homologs Possessing the Targeted Function? Tyrosine Aminotransferase from Aspartate Aminotransferase. *Journal of Molecular Biology* **2003**, *327* (3), 593-608.
37. Storici, P.; Capitani, G.; Müller, R.; Schirmer, T.; Jansonius, J. N., Crystal structure of human ornithine aminotransferase complexed with the highly specific and potent inhibitor 5-fluoromethylornithine 111 Edited by R. Huber. *Journal of Molecular Biology* **1999**, *285* (1), 297-309.
38. Dreffs, A.; Henderson, D.; Dmitriev, A. V.; Antonetti, D. A.; Linsenmeier, R. A., Retinal pH and Acid Regulation During Metabolic Acidosis. *Curr Eye Res* **2018**, *43* (7), 902-912.
39. Fallingborg, J., Intraluminal pH of the human gastrointestinal tract. *Danish medical bulletin* **1999**, *46* (3), 183-196.
40. Hamm, L. L.; Nakhoul, N.; Hering-Smith, K. S., Acid-Base Homeostasis. *Clin J Am Soc Nephrol* **2015**, *10* (12), 2232-2242.

41. Park, R.; Leach, W. J.; Arieff, A. I., Determination of liver intracellular pH in vivo and its homeostasis in acute acidosis and alkalosis. *American Journal of Physiology-Renal Physiology* **1979**, 236 (3), F240-F245.
42. Peraino, C.; Pitot, H. C., Ornithine- δ -transaminase in the rat I. Assay and some general properties. *Biochimica et Biophysica Acta (BBA) - Specialized Section on Enzymological Subjects* **1963**, 73 (2), 222-231.
43. Mueckler, M. M.; Himeno, M.; Pitot, H. C., In vitro synthesis and processing of a precursor to ornithine aminotransferase. *Journal of Biological Chemistry* **1982**, 257 (12), 7178-7180.
44. Hao, G.; Xu, Z. P.; Li, L., Manipulating extracellular tumour pH: an effective target for cancer therapy. *RSC advances* **2018**, 8 (39), 22182-22192.
45. Shirmanova, M. V.; Druzhkova, I. N.; Lukina, M. M.; Matlashov, M. E.; Belousov, V. V.; Snopova, L. B.; Prodanetz, N. N.; Dudenkova, V. V.; Lukyanov, S. A.; Zagaynova, E. V., Intracellular pH imaging in cancer cells in vitro and tumors in vivo using the new genetically encoded sensor SypHer2. *Biochimica et Biophysica Acta (BBA)-General Subjects* **2015**, 1850 (9), 1905-1911.
46. Liu, P.; Zhang, H.; Lv, M.; Hu, M.; Li, Z.; Gao, C.; Xu, P.; Ma, C., Enzymatic production of 5-aminovalerate from l-lysine using l-lysine monooxygenase and 5-aminovaleramidase amidohydrolase. *Scientific Reports* **2014**, 4 (1), 5657.
47. Adams, E.; Frank, L., Metabolism of Proline and the Hydroxyprolines. *Annual Review of Biochemistry* **1980**, 49 (1), 1005-1061.
48. Rodrigues, W. F.; Miguel, C. B.; Agostinho, F.; da Silva, G. V.; Lazo-Chica, J. E.; Naressi Scapin, S. M.; Napimoga, M. H.; Trindade-da-Silva, C. A.; Krieger, J. E.; Pereira, A. d. C.; Oliveira, C. J. F.; Soares, S. d. C.; Ueira-Vieira, C., Metabolomic Evaluation of Chronic Periodontal Disease in Older Adults. *Mediators Inflamm* **2021**, 2021, 1796204-1796204.
49. Falch, E.; Hedegaard, A.; Nielsen, L.; Jensen, B. R.; Hjeds, H.; Krosgaard-Larsen, P., Comparative Stereostructure-Activity Studies on GABAA and GABAB Receptor Sites and GABA Uptake Using Rat Brain Membrane Preparations. *Journal of Neurochemistry* **1986**, 47 (3), 898-903.
50. Ellis, K. J.; Morrison, J. F., [23] Buffers of constant ionic strength for studying pH-dependent processes. In *Methods in Enzymology*, Purich, D. L., Ed. Academic Press: **1982**; Vol. 87, pp 405-426.

51. Vonrhein, C.; Flensburg, C.; Keller, P.; Sharff, A.; Smart, O.; Paciorek, W.; Womack, T.; Bricogne, G., Data processing and analysis with the autoPROC toolbox. *Acta Crystallographica Section D* **2011**, *67* (4), 293-302.
52. Battye, T. G. G.; Kontogiannis, L.; Johnson, O.; Powell, H. R.; Leslie, A. G. W., iMOSFLM: a new graphical interface for diffraction-image processing with MOSFLM. *Acta Crystallogr D Biol Crystallogr* **2011**, *67* (Pt 4), 271-281.
53. McCoy, A. J.; Grosse-Kunstleve, R. W.; Adams, P. D.; Winn, M. D.; Storoni, L. C.; Read, R. J., Phaser crystallographic software. *Journal of Applied Crystallography* **2007**, *40* (4), 658-674.
54. Liebschner, D.; Afonine, P. V.; Baker, M. L.; Bunkoczi, G.; Chen, V. B.; Croll, T. I.; Hintze, B.; Hung, L. W.; Jain, S.; McCoy, A. J.; Moriarty, N. W.; Oeffner, R. D.; Poon, B. K.; Prisant, M. G.; Read, R. J.; Richardson, J. S.; Richardson, D. C.; Sammito, M. D.; Sobolev, O. V.; Stockwell, D. H.; Terwilliger, T. C.; Urzhumtsev, A. G.; Videau, L. L.; Williams, C. J.; Adams, P. D., Macromolecular structure determination using X-rays, neutrons and electrons: recent developments in Phenix. *Acta Crystallogr D Struct Biol* **2019**, *75* (Pt 10), 861-877.
55. Emsley, P.; Lohkamp, B.; Scott, W. G.; Cowtan, K., Features and development of Coot. *Acta Crystallogr D Biol Crystallogr* **2010**, *66* (Pt 4), 486-501.
56. Paettersen, E.; Goddard, T.; Huang, C.; Couch, G.; Greenblatt, D.; Meng, E.; Ferrin, T., UCSF Chimera--a visualization system for exploratory research and analysis. *J Comput Chem* **2004**, *25* (13), 1605-12.
57. Eliot, A. C.; Kirsch, J. F., Pyridoxal phosphate enzymes: mechanistic, structural, and evolutionary considerations. *Annu Rev Biochem* **2004**, *73*, 383-415.
58. Mehta, P. K.; Hale, T. I.; Christen, P., Aminotransferases: demonstration of homology and division into evolutionary subgroups. *Eur J Biochem* **1993**, *214* (2), 549-61.
59. Hayashi, H., Pyridoxal enzymes: mechanistic diversity and uniformity. *J. Biochem.* **1995**, *118* (3), 463-473.
60. Ginguay, A.; Cynober, L.; Curis, E.; Nicolis, I., Ornithine Aminotransferase, an Important Glutamate-Metabolizing Enzyme at the Crossroads of Multiple Metabolic Pathways. *Biology (Basel)* **2017**, *6* (1).
61. Wang, G.; Shang, L.; Burgett, A. W.; Harran, P. G.; Wang, X., Diazonamide toxins reveal an unexpected function for ornithine delta-amino transferase in mitotic cell division. *Proc Natl Acad Sci U S A* **2007**, *104* (7), 2068-73.

62. Lee, H.; Juncosa, J. I.; Silverman, R. B., Ornithine aminotransferase versus GABA aminotransferase: implications for the design of new anticancer drugs. *Med Res Rev* **2015**, *35* (2), 286-305.
63. Moschitto, M. J.; Doubleday, P. F.; Catlin, D. S.; Kelleher, N. L.; Liu, D.; Silverman, R. B., Mechanism of Inactivation of Ornithine Aminotransferase by (1S,3S)-3-Amino-4-(hexafluoropropan-2-ylidene)cyclopentane-1-carboxylic Acid. *J Am Chem Soc* **2019**, *141* (27), 10711-10721.
64. Abeles, R. H.; Maycock, A. L., Suicide Enzyme Inactivators. *Acc. Chem. Res.* **1976**, *9* (9), 313-319.
65. Juncosa, J. I.; Takaya, K.; Le, H. V.; Moschitto, M. J.; Weerawarna, P. M.; Mascarenhas, R.; Liu, D.; Dewey, S. L.; Silverman, R. B., Design and Mechanism of (S)-3-Amino-4-(difluoromethylenyl)cyclopent-1-ene-1-carboxylic Acid, a Highly Potent gamma-Aminobutyric Acid Aminotransferase Inactivator for the Treatment of Addiction. *J Am Chem Soc* **2018**.
66. Le, H. V.; Hawker, D. D.; Wu, R.; Doud, E.; Widom, J.; Sanishvili, R.; Liu, D.; Kelleher, N. L.; Silverman, R. B., Design and Mechanism of Tetrahydrothiophene-Based gamma-Aminobutyric Acid Aminotransferase Inactivators. *J Am Chem Soc* **2015**, *137* (13), 4525-33.
67. Mascarenhas, R.; Le, H. V.; Clevenger, K. D.; Lehrer, H. J.; Ringe, D.; Kelleher, N. L.; Silverman, R. B.; Liu, D., Selective Targeting by a Mechanism-Based Inactivator against Pyridoxal 5'-Phosphate-Dependent Enzymes: Mechanisms of Inactivation and Alternative Turnover. *Biochemistry* **2017**, *56* (37), 4951-4961.
68. Moschitto, M. J.; Doubleday, P. F.; Catlin, D. S.; Kelleher, N. L.; Liu, D.; Silverman, R. B., Mechanism of Inactivation of Ornithine Aminotransferase by (1 S,3 S)-3-Amino-4-(hexafluoropropan-2-ylidene)cyclopentane-1-carboxylic Acid. *J Am Chem Soc* **2019**.
69. Zhu, W.; Doubleday, P. F.; Catlin, D. S.; Weerawarna, P. M.; Butrin, A.; Shen, S.; Wawrzak, Z.; Kelleher, N. L.; Liu, D.; Silverman, R. B., A Remarkable Difference That One Fluorine Atom Confers on the Mechanisms of Inactivation of Human Ornithine Aminotransferase by Two Cyclohexene Analogues of gamma-Aminobutyric Acid. *J Am Chem Soc* **2020**, *142* (10), 4892-4903.
70. Toney, M. D., Reaction specificity in pyridoxal phosphate enzymes. *Arch. Biochem. Biophys.* **2005**, *433*, 279-287.

71. Hayashi, H.; Kagamiyama, H., Transient-state kinetics of the reaction of aspartate aminotransferase with aspartate at low pH reveals dual routes in the enzyme-substrate association process. *Biochemistry* **1997**, *36* (13558-13569).
72. Williams, J. A.; Bridge, G.; Fowler, L. J.; John, R. A., The reaction of ornithine aminotransferase with ornithine. *Biochem J* **1982**, *201* (1), 221-5.
73. Storici, P.; Capitani, G.; Muller, R.; Schirmer, T.; Jansonius, J. N., Crystal structure of human ornithine aminotransferase complexed with the highly specific and potent inhibitor 5-fluoromethylornithine. *J Mol Biol* **1999**, *285* (1), 297-309.
74. Shah, S. A.; Shen, B. W.; Brunger, A. T., Human ornithine aminotransferase complexed with L-canaline and gabaculine: structural basis for substrate recognition. *Structure* **1997**, *5* (8), 1067-75.
75. Storici, P.; Qiu, J.; Schirmer, T.; Silverman, R. B., Mechanistic crystallography. Mechanism of inactivation of gamma-aminobutyric acid aminotransferase by (1R,3S,4S)-3-amino-4-fluorocyclopentane-1-carboxylic acid as elucidated by crystallography. *Biochemistry* **2004**, *43* (44), 14057-14063.
76. Reddy, V. P., *Organofluorine Compounds in Biology and Medicine*. Elsevier: 2015; p 330.
77. Vulpetti, A.; Dalvit, C., Fluorine local environment: from screening to drug design. *Drug Discov Today* **2012**, *17* (15-16), 890-7.
78. Dalvit, C.; Ko, S. Y.; Vulpetti, A., Application of the rule of shielding in the design of novel fluorinated structural motifs and peptidomimetics. *Journal of Fluorine Chemistry* **2013**, *152*, 129-135.
79. Burgi, H. B.; Dunitz, J. D.; Lehn, J. M.; Wipff, G., Stereochemistry of Reaction Paths at Carbonyl Centers. *Tetrahedron* **1974**, *30* (12), 1563-1572.
80. Koch, C. J.; Parliament, M. B.; Brown, M.; Urtasun, R. C., Chemical Modifiers of Radiation Response. In *Leibel and Phillips Textbook of Radiation Oncology*, 3rd ed.; ElsevierHealth: **2010**; pp 55-68.
81. Shen, B. W.; Hennig, M.; Hohenester, E.; Jansonius, J. N.; Schirmer, T., Crystal structure of human recombinant ornithine aminotransferase. *J Mol Biol* **1998**, *277* (1), 81-102.

82. Bolkenius, F. N.; Knödgen, B.; Seiler, N., dl-canaline and 5-fluoromethylornithine. Comparison of two inactivators of ornithine aminotransferase. *Biochemical Journal* **1990**, *268* (2), 409-414.
83. Butrin, A.; Beaupre, B. A.; Kadamandla, N.; Zhao, P.; Shen, S.; Silverman, R. B.; Moran, G. R.; Liu, D., Structural and Kinetic Analyses Reveal the Dual Inhibition Modes of Ornithine Aminotransferase by (1S,3S)-3-Amino-4-(hexafluoropropan-2-ylidene)-cyclopentane-1-carboxylic Acid (BCF3). *ACS Chemical Biology* **2020**.
84. Clift, M. D.; Ji, H.; Deniau, G. P.; O'Hagan, D.; Silverman, R. B., Enantiomers of 4-amino-3-fluorobutanoic acid as substrates for gamma-aminobutyric acid aminotransferase. Conformational probes for GABA binding. *Biochemistry* **2007**, *46* (48), 13819-28.
85. Gokcan, H.; Konuklar, F. A., Theoretical study on HF elimination and aromatization mechanisms: a case of pyridoxal 5' phosphate-dependent enzyme. *J Org Chem* **2012**, *77* (13), 5533-43.
86. Alunni, S.; De Angelis, F.; Ottavi, L.; Papavasileiou, M.; Tarantelli, F., Evidence of a borderline region between E1cb and E2 elimination reaction mechanisms: a combined experimental and theoretical study of systems activated by the pyridine ring. *J Am Chem Soc* **2005**, *127* (43), 15151-60.
87. Silverman, R. B., Design and Mechanism of GABA Aminotransferase Inactivators. Treatments for Epilepsies and Addictions. *Chem Rev* **2018**, *118* (7), 4037-4070.
88. Winter, G., xia2: an expert system for macromolecular crystallography data reduction. *Journal of Applied Crystallography* **2010**, *43* (1), 186-190.
89. Phang, J. M.; Donald, S. P.; Pandhare, J.; Liu, Y., The metabolism of proline, a stress substrate, modulates carcinogenic pathways. *Amino Acids* **2008**, *35* (4), 681-690.
90. Phang, J. M.; Liu, W.; Hancock, C. N.; Fischer, J. W., Proline metabolism and cancer: emerging links to glutamine and collagen. *Curr Opin Clin Nutr Metab Care* **2015**, *18* (1), 71-77.
91. Phang, J., The Proline Regulatory Axis and Cancer. *Frontiers in Oncology* **2012**, *2*.
92. Phang, J. M.; Liu, W.; Zabornyk, O., Proline Metabolism and Microenvironmental Stress. *Annual Review of Nutrition* **2010**, *30* (1), 441-463.
93. Vander Heiden Matthew, G.; Cantley Lewis, C.; Thompson Craig, B., Understanding the Warburg Effect: The Metabolic Requirements of Cell Proliferation. *Science* **2009**, *324* (5930), 1029-1033.

94. Tang, L.; Zeng, J.; Geng, P.; Fang, C.; Wang, Y.; Sun, M.; Wang, C.; Wang, J.; Yin, P.; Hu, C.; Guo, L.; Yu, J.; Gao, P.; Li, E.; Zhuang, Z.; Xu, G.; Liu, Y., Global Metabolic Profiling Identifies a Pivotal Role of Proline and Hydroxyproline Metabolism in Supporting Hypoxic Response in Hepatocellular Carcinoma. *Clinical Cancer Research* **2018**, *24* (2), 474.
95. Liu, Y.; Wu, L.; Li, K.; Liu, F.; Wang, L.; Zhang, D.; Zhou, J.; Ma, X.; Wang, S.; Yang, S., Ornithine aminotransferase promoted the proliferation and metastasis of non-small cell lung cancer via upregulation of miR-21. *Journal of Cellular Physiology* **2019**, *234* (8), 12828-12838.
96. Silverman, R. B., [10] Mechanism-based enzyme inactivators. In *Methods in Enzymology*, Academic Press: **1995**; Vol. 249, pp 240-283.
97. Pan, Y.; Gerasimov, M. R.; Kvist, T.; Wellendorph, P.; Madsen, L. L.; Pera, E.; Lee, H.; Schousboe, A.; Chebib, M.; Bräuner-Osborne, H.; Craft, C. M.; Brodie, J. D.; Schiffer, W. K.; Dewey, S. L.; Miller, S. R.; Silverman, R. B., CPP-115, a Potent γ -Aminobutyric Acid Aminotransferase Inactivator for the Treatment of Cocaine Addiction. *Journal of Medicinal Chemistry* **2012**, *55* (1), 357-366.
98. Pan, Y.; Qiu, J.; Silverman, R. B., Design, Synthesis, and Biological Activity of a Difluoro-Substituted, Conformationally Rigid Vigabatrin Analogue as a Potent γ -Aminobutyric Acid Aminotransferase Inhibitor. *Journal of Medicinal Chemistry* **2003**, *46* (25), 5292-5293.
99. Lee, H.; Doud, E. H.; Wu, R.; Sanishvili, R.; Juncosa, J. I.; Liu, D.; Kelleher, N. L.; Silverman, R. B., Mechanism of Inactivation of γ -Aminobutyric Acid Aminotransferase by (1S,3S)-3-Amino-4-difluoromethylene-1-cyclopentanoic Acid (CPP-115). *Journal of the American Chemical Society* **2015**, *137* (7), 2628-2640.

VITA

Dr. Butrin was born and raised in Almaty, Kazakhstan. He graduated from New School High School in 2014. In 2015, he moved to Mississippi, USA with his family. He received his Bachelor of Science in Chemistry from Mississippi State University, Mississippi, USA in 2017. In 2018, he began the PhD program in Chemistry and Biochemistry at Loyola University Chicago.